

# Influence of Electromagnetic Intermolecular Forces on Thermodynamic Properties

J. Avsec<sup>1</sup>, I. Medved<sup>2</sup>

University of Maribor, Faculty of Energy Technology<sup>1</sup>  
Hocevarjev trg 1, 8270 Krsko,

Constantine the Philosopher University in Nitra, Faculty of Natural Sciences<sup>2</sup>  
Trieda Andreja Hlinku 1, 94974 Nitra,  
e-mail: jurij.avsec@uni-mb.si, imedved@ukf.sk

**Abstract.** This article presents the mathematical model for determination of thermophysical properties in dependence of temperature and volume. On this basis, to develop the model, we have used statistical thermomechanics to describe the influence of electromagnetic nature of electromagnetic forces. The analysis in presented article focused on virial coefficients as one of very important parameters.

**Keywords:** *statistical thermodynamics, electromagnetic interaction, constant heat flux, constant wall temperature.*

## 1. Introduction

Billions of years ago, when enormous quantities of energy were released after the Big Bang, the fundamental particles followed by molecules were formed into complex structures according to certain coincidental events. In the period of several billion years of development, the Earth was also shaped as one of the planets in space, after which life was created on it.

Table 1: The forces of nature [1]

Force	Force particle	Mass
Strong	Gluon	0
Electromagnetic	Photon	0
Weak	Weak gauge bosons	86.97
Gravity	Graviton	0

Today all physical phenomena could we explain with the knowledge of 4 fundamental forces: gravitation, electromagnetic, weak and strong (Table 1). Gravitation is important if we take into account big distances or big masses, electromagnetic force is force which covers chemical and biological reactions, weak and strong force are important when we study changes in atomic nucleus [1]. Through the history of creation of universe the theories show that when young universe was created some speculations say that at first was created one or maybe two force (Figure 1).

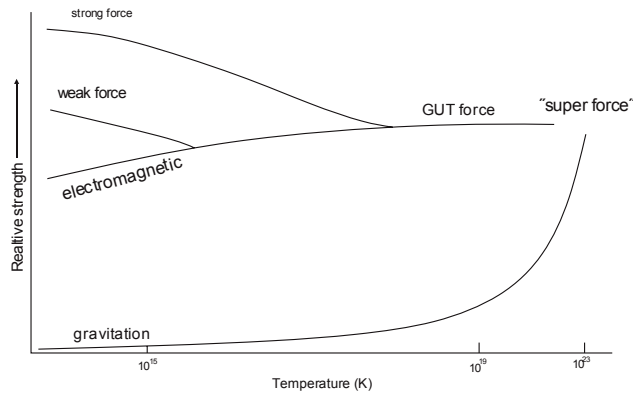


Figure 1: The history of natural forces creation

Unfortunately we could not at the same time with one model explain all fundamental forces from the physical point of view. For majority of important phenomena in electromagnetics is satisfactory to take into account only electromagnetic force. With electromagnetic force we could explain many important phenomena like phase transitions, chemical reactions, heat transfer, changes of thermophysical properties in dependence of temperature, volume, magnetic field and other phenomena.

## 2. Statistical mechanics taking into account electromagnetic forces

To calculate thermodynamic functions of state, we applied the canonical partition function [2-4] Utilising the semi-classical formulation for the purpose of the canonical ensemble for the  $N$  indistinguishable molecules, the partition function  $Z$  can be expressed as follows:

$$Z = \frac{1}{N!h^N} \int \dots \int \exp\left(-\frac{H}{kT}\right) \cdot d\vec{r}_1 d\vec{r}_2 \dots d\vec{r}_N d\vec{p}_1 d\vec{p}_2 \dots d\vec{p}_N \quad (1)$$

where  $f$  stands for the number of degrees of freedom of an individual molecule,  $H$  designates the Hamiltonian molecule system, vectors  $\vec{r}_1, \vec{r}_2, \dots, \vec{r}_N$  describe the positions of  $N$  molecules and  $\vec{p}_1, \vec{p}_2, \dots, \vec{p}_N$  momenta,  $k$  is the Boltzmann's constant and  $h$  is Planck's constant. The canonical ensemble of partition function for the system of  $N$  molecules can be expressed by:

$$Z = Z_0 Z_{trans} Z_{vib} Z_{rot} Z_{ir} Z_{el} Z_{nuc} Z_{conf} \quad (2)$$

Thus, the partition function  $Z$  is a product of terms of the ground state (0), the translation (*trans*), the vibration (*vib*), the rotation (*rot*), the internal rotation (*ir*), the influence of electrons excitation (*el*), the influence of nuclei excitation (*nuc*) and the influence of the intermolecular potential energy (*conf*).

Utilising the canonical theory for computation, the thermodynamic functions of the state can be defined as follows:[3-5]

$$\begin{aligned}
 \text{Pressure } p &= kT \left( \frac{\partial \ln Z}{\partial T} \right)_V, \\
 \text{Internal energy } U &= kT^2 \left( \frac{\partial \ln Z}{\partial T} \right)_V \\
 \text{Entropy } S &= k \left[ \ln Z + T \left( \frac{\partial \ln Z}{\partial T} \right)_V \right] \\
 \text{Enthalpy } H_h &= kT \left[ T \left( \frac{\partial \ln Z}{\partial T} \right)_V + V \left( \frac{\partial \ln Z}{\partial V} \right)_T \right]
 \end{aligned} \tag{3}$$

where  $T$  is temperature and  $V$  is volume of molecular system.

### 3. Second virial coefficients and higher orders of virial coefficients

Calculation of second virial coefficient for real substances is possible by the classical and statistical thermodynamics. Classical thermodynamics has no insight into the microstructure of the substance. But it allows the calculation of thermodynamics function of state with assistance of measurement or empirical equations. Statistical thermodynamics, on the other hand, calculates the properties of state on the basis of molecular motions in a space, and on the basis of the intermolecular interactions.

The virial equation of state is the expansion of the compressibility factor  $Z_r$  along individual isotherms in terms of density around according to the next equation:

$$Z_r = \frac{pV}{NkT} = 1 + \frac{B_2}{V} + \frac{B_3}{V^2} \dots \tag{4}$$

where  $B_2$  and  $B_3$  are second and third virial coefficient and the are defined as:

$$B_2 = \left( \frac{\partial Z_r}{\partial n} \right)_{n=0} = \left( \frac{\partial Z_r}{\partial \rho} \right)_{\rho=0}, \quad B_3 = \frac{1}{2!} \left( \frac{\partial^2 Z_r}{\partial n^2} \right)_{n=0} = \frac{1}{2!} \left( \frac{\partial^2 Z_r}{\partial \rho^2} \right)_{\rho=0} \tag{5}$$

The virial coefficients are properties of the gas at  $n = 0$ . The second virial coefficient is the first term of the expansion of the compressibility factor of a fluid in powers of the density. From statistical mechanics the second virial coefficient summarizes the influence of two body interactions, the third virial coefficient summarizes influences of three-body interactions... The are properties of gas at  $n = 0$  and the do not depend on density, but only on temperature and, in mixtures, on composition. A general expression for virial coefficients related with the equation of state can be written with the next equation:

$$B_k = \frac{1}{(k-1)!} \left( \frac{\partial^{k-1} Z_r}{\partial \rho^{k-1}} \right)_{\rho=0} \tag{6}$$

In the presented paper we have used the combination of equations (10) and the method of statistical mechanics. On this basis we can express the free energy of a fluid as the sum of all parts:

$$A = A^{LJ} + A^{ex} \quad (7)$$

On the basis of Eq. (12) we can express

$$B = B_{LJ} + B_{ex} \quad (8)$$

If the virial coefficients are known as a function of temperature, all thermodynamic functions depending on the equation of state may be calculated:

$$U_{conf} = -NkT^2 \left[ n \frac{dB_2}{dT} + \frac{n^2}{2} \frac{dB_3}{dT} + \dots \right] \quad (9)$$

$$S_{conf} = -Nk \left[ \left( B_2 + T \frac{dB_2}{dT} \right) n + \left( B_3 + T \frac{dB_3}{dT} \right) \frac{n^2}{2} + \dots \right] \quad (10)$$

Second virial coefficients and higher orders of virial coefficients

Revised Cotterman EOS is based on the hard sphere perturbation theory. The average relative deviation for pressure and internal energy in comparison with Monte-Carlo simulations are 2.17% and 2.62% respectively for 368 data points 9. The configurational free energy is given by:

$$A_{LJ} = A_{hs} + A_{pert} \quad (11)$$

$$\frac{A_{hs}}{R_m T} = \frac{4\eta - 3\eta^2}{(1-\eta)^2}, \quad (12)$$

$$A_{pert} = \frac{A^{(1)}}{T^*} + \frac{A^{(2)}}{T^{*2}} \quad (13)$$

$$\frac{A^{(1)}}{R_m T} = \sum_{m=1}^4 A_{1m} \left( \frac{\eta}{\tau} \right)^m, \quad \frac{A^{(2)}}{R_m T} = \sum_{m=1}^4 A_{2m} \left( \frac{\eta}{\tau} \right)^m \quad (14)$$

$$\tau = 0.7405, \quad \eta = \frac{\pi \rho d^3}{6} \quad (15)$$

where  $\eta$  is packing factor,  $D$  is hard-sphere diameter. The effective hard sphere diameter  $d$  is determined on the basis of Barker perturbation theory. We use a function developed in the work of Chapman et al.27

$$d = \sigma \frac{1 + 0.2977T^*}{1 + 0.33163T^* + 0.0010477T^{*2}} \quad (16)$$



With help of configurational free energy we can calculate all configurational thermodynamic properties. Expressions for calculation of configurational entropy and internal energy are shown in literature 9. We carried out all other expressions for calculation of thermophysical properties.

In the broadest sense we can express the  $n$ -th virial coefficient as the sum of two parts:

$$B_{nLJ} = B_{nhs} + B_{npert} \quad (17)$$

The first part in the Eq. (22) represents hard sphere part and the second part represents the perturbation term where are also hidden the effects of polarity. On the basis of Eqs. (10) we expressed the next analytical expressions:

$$B_{2hs} = \frac{2\pi d^3}{3}, B_{3hs} = 10 \left( \frac{\pi d^3}{6} \right)^2, B_{4hs} = 18.3648 \left( \frac{\pi d^3}{6} \right)^3, \\ B_{5hs} = 28.2245 \left( \frac{\pi d^3}{6} \right)^4, B_{6hs} = 39.83 \left( \frac{\pi d^3}{6} \right)^5 \quad (18)$$

$$B_{2pert} = \frac{d^3}{\sqrt{2}} \left( \frac{A_{11}}{T^*} + \frac{A_{21}}{T^{*2}} \right), B_{3pert} = d^6 \left( \frac{A_{12}}{T^*} + \frac{A_{22}}{T^{*2}} \right), \\ B_{4pert} = \frac{3d^9}{2^{1.5}} \left( \frac{A_{13}}{T^*} + \frac{A_{23}}{T^{*2}} \right), B_{5pert} = d^{12} \left( \frac{A_{14}}{T^*} + \frac{A_{24}}{T^{*2}} \right), B_{6pert} = 0 \quad (19)$$

Using the perturbation expansion around the reference potential one can then write the configuration effect to the free energy as:

$$\frac{A_{conf}}{Nk_B T} = \frac{A^{LJ}}{Nk_B T} + \frac{A^\lambda}{Nk_B T} + \frac{A^{\lambda\lambda}}{Nk_B T} + \frac{A^{\lambda\lambda\lambda}}{Nk_B T} \quad (20)$$

There are several methods to compute the influence of anisotropic potentials [3-8]. In the present paper those models were used which yielded favourable results in practical computations for a large number of components and within a relatively wide range of densities and temperatures.

The perturbation theory is applied successfully to real fluids of moderate polarity and to molecules of simple structure. The problem in perturbation theory is that in series of the perturbation expansion converges slowly as the dipole moment increases. The application of Pade equation can help that the equation converge more rapidly. However, for highly polar molecules, if a simple reference model is used the perturbation terms become greater than the reference term, which in principle is not a small perturbation on which the theory of small perturbation is based. From scientific point of view is impossible to calculate the thermodynamic properties for highly polar molecules on the basis of perturbation theory. In the presented paper we have used the mean potential model, instead of the statistical-mechanical perturbation theory, to avoid mentioned problems. The orientation-averaged pair potential for polar molecules is given by the next equations:

where:

$$\epsilon' = \epsilon \left( 1 + \frac{\mu^4}{6kT\epsilon\sigma^6} + \dots \right), \quad (\sigma')^6 = \frac{\sigma^6}{\left( 1 + \frac{\mu^4}{12kT\epsilon\sigma^6} + \dots \right)} \quad (21)$$

In the presented equation is taken into account the most important term in the multipole expansion, the dipole-dipole interaction.

#### 4. Results and discussion

The results for hydrocarbons are presented in the Figs. (2) and (3). In Figs. (2) and (3) are presented results for second, third, fourth and fifth virial coefficient for ethane. Figure 4 shows second virial coefficient analytical computation for equimolar mixture between ethane (C<sub>2</sub>H<sub>6</sub>) and propane (C<sub>3</sub>H<sub>8</sub>). Figure 4 shows the analytical results for second virial coefficient for equimolar mixture of ethane and propane.

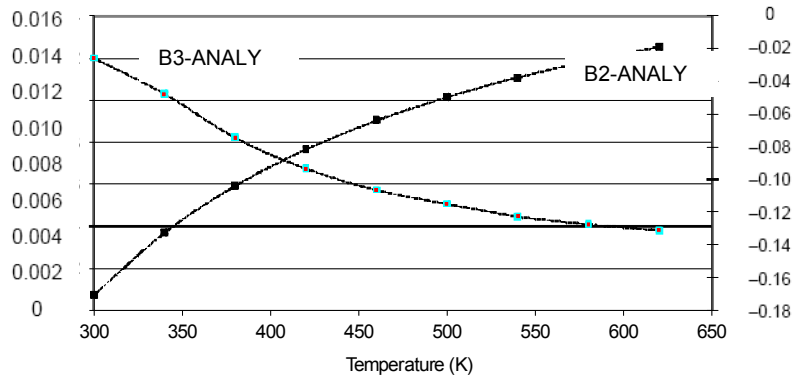


Figure 2: Second and third virial coefficient for ethane (C<sub>2</sub>H<sub>6</sub>)

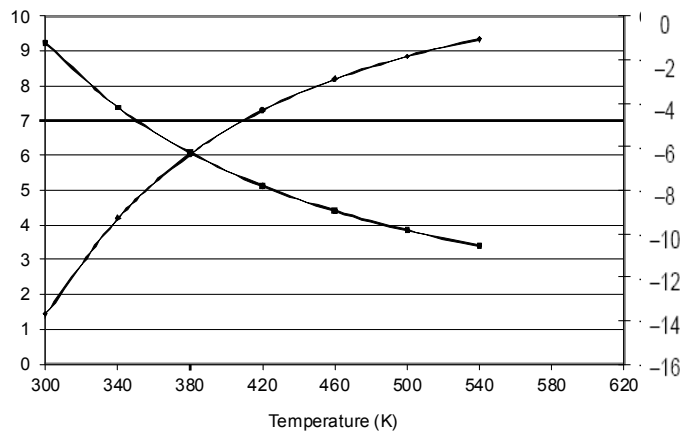


Figure 3: Fourth and fifth virial coefficient for ethane (C<sub>2</sub>H<sub>6</sub>)

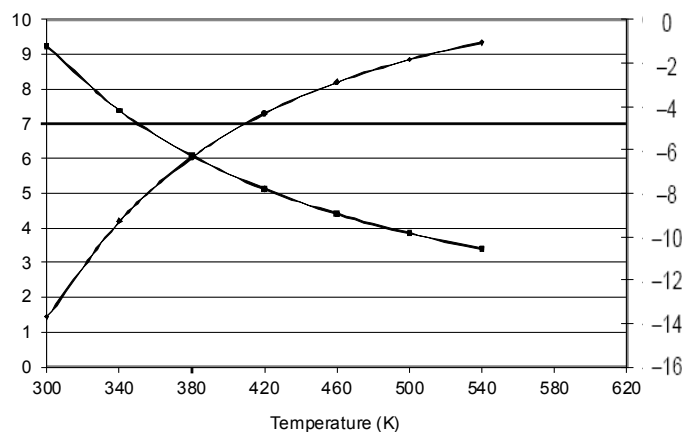


Figure 4: Second virial coefficient for equimolar mixture of ethane and propane

## 5. Conclusion

This paper has developed an analytical formulation of for calculation of virial coefficients on the basis of statistical thermodynamics. The formulation includes all kinds of molecular motion such as translation, rotation, vibration of molecules and intermolecular potential caused due to electromagnetic forces. In the presented article we have concentrated on hydrocarbons and formulation of virial coefficients.

## References

- [1] Greene, B.: *The elegant Universe*, Vintage Books, (2000).
- [2] Kumar, S., Khanna, K. N.: *Viorial Coefficients from Equation of State*, Journal of Molecular Liquids, Vol. 107, No. 1-3, (2003), pp. 41–57.
- [3] Boublik, T., Nezbeda, I.: *P-V-T Behavior of Hard Body Fluids, Theory and Experiment*, Collection Czechoslovak Chem. Commun., Vol. 51, (1986), pp. 2301–2433.
- [4] Jenaček, J., Boublik, T.: *The second virial coefficient of polar-rod-like Molecules*, Fluid Phase Equilibria, Vol. 212, (2003), pp. 349–361.
- [5] Lucas, K.: *Applied Statistical Thermodynamics*, Springer Verlag, New York, (1992).
- [6] Gray, C. G., Gubbins, K. E.: *Theory of Molecular Fluids*, Clarendon Press, Oxford, (1984).
- [7] Avsec J., Marcic, M., Watanabe, K.: *Study for Lennard-Jones Chains for Hydrocarbons*, J. thermophys. heat transf., Vol. 18., No. 2., (2004), pp. 243–252.
- [8] Chung, T. H., Khan, M. M., Lee, L. L., Starling, K. E.: *A New Equation of State for Polar and Nonpolar Pure Fluids*, Fluid Phase Equilibria, Vol. 17., (1984), pp.: 351–372.
- [9] Chunxi, L., Yigui, L., Jiufang, L.: *Investigation and Improvement of Equations of State for Lennard-Jones Fluid*, Fluid Phase Equilibria, Vol. 127., (1997), pp. 71–81.

# Electromagnetics of an Electroactive Polymer Actuator

Á. Aczél

Széchenyi István University, Egyetem tér 1., H-9026 Győr  
e-mail: aczela@sze.hu

**Abstract.** The aim of this paper is to describe the electromagnetic phenomena in an electroactive polymer actuator when external electric field is applied and to form a bridge between the two mainstream methods of handling the coupled problem of the electroactive polymers. Therefore, the electromagnetic field variables are estimated in a usual actuator for determining the order of magnitude of the contributions to the effective fields and to the total current density.

**Keywords:** *Electroactive polymer, coupled problem, Lorentz transformation, effective field.*

## 1. Introduction

Materials whose rheological properties can be varied by application of electric fields are called electroactive materials [1, 2]. The behaviour of these rubberlike media is used to be investigated in two different ways. Brigadnov, Dorfmann, Bustamante, Ogden and others [3, 4, 5] try to describe the coupled problem of finite deformation of the continua under electromagnetic field by taking into account all the phenomena emerging as a result of the electromagnetic excitation. Pelrine, Kornbluh, Sommer-Larsen and others [6] try to present a phenomenological description.

Our aim is to form a bridge between these two points of view by neglecting those terms of the governing and transformation equations that are smaller by several orders of magnitude than other contributions.

First, those equations are presented, that govern the finite deformation of a rubberlike continuum. After that, the electromagnetic field variables will be defined, with the Maxwell equations. Finally, those estimations will be taken that shows the order of magnitude of the different contributions to the so-called effective fields.

*Table 1. Notation*

Electrodynamics:	
<b>E</b>	Electric field intensity
<b>D</b>	Electric displacement
<b>H</b>	Magnetic field intensity
<b>B</b>	Magnetic induction
<b>P</b>	Polarization density

<b>M</b>	Magnetization density
$\varepsilon_r, \varepsilon_0$	Relative dielectric constant, dielectric constant in the vacuum
$\mu_r, \mu_0$	Relative magnetic permeability, magnetic permeability in the vacuum
$\nu$	Conductivity
$q$	Charge per unit volume
<b>J</b>	Current per unit area
$c$	Speed of light in the vacuum
Continuum mechanics	
<b>v</b>	Velocity of the material body
$\rho$	Mass density
$\mathbf{t}^{(n)}$	Stress vector (traction) at the surface with unit normal <b>n</b>
<b>F</b>	Force per unit volume, acting on the material body
<b>r</b>	Position vector
<b>L</b>	Body couple per unit volume
$\Phi$	Energy supply density
$U$	Potential energy per unit volume
<b>Q</b>	Heat flux vector
$Y$	Young's modulus
Application as actuator	
$V$	Voltage applied to the actuator
$C$	Capacitance of the EAP actuator
$I$	Current
$A$	Area of the EAP layer
$F$	Force acting on the EAP layer due to the applied voltage
$d$	Thickness of the EAP layer

## 2. The governing equations

The deformation of the electroactive polymer (EAP) actuator under voltage is governed by the balance equations of the continuum mechanics and the Maxwell's equations, simultaneously. The basic balance laws, that govern the mechanics of the continuum are the balance of mass, the balance of linear momentum, the balance of angular momentum, and the balance of energy [7], respectively:

$$\frac{d}{dt} \int_V \rho \, dV = 0, \quad \frac{d}{dt} \int_V \rho \mathbf{v} \, dV = \oint_S \mathbf{t}^{(n)} dS + \int_V \mathbf{F} \, dV \quad (1)$$

$$\frac{d}{dt} \int_V \mathbf{r} \times \rho \mathbf{v} \, dV = \oint_S \mathbf{r} \times \mathbf{t}^{(n)} dS + \int_V \mathbf{r} \times \mathbf{F} + \mathbf{L} \, dV \quad (2)$$

$$\frac{d}{dt} \int_V \rho \left( \frac{1}{2} \mathbf{v} \cdot \mathbf{v} + U \right) dV = \oint_S (\mathbf{t}^{(n)} \cdot \mathbf{v} - \mathbf{Q} \cdot \mathbf{n}) dS + \int_V (\mathbf{F} \cdot \mathbf{v} + \Phi_\rho + \Phi) dV \quad (3)$$

The local forms of the Maxwell's equations are [8]:

$$\text{curl } \mathbf{H} = \mathbf{J} + \frac{\partial \mathbf{D}}{\partial t}, \quad \text{curl } \mathbf{E} = -\frac{\partial \mathbf{B}}{\partial t} \quad (4)$$

$$\text{div } \mathbf{B} = 0, \quad \text{div } \mathbf{D} = q \quad (5)$$

The coupling between the continuum mechanics and the electromagnetic phenomena is hidden in three variables in the balance equations: *body force per unit volume*  $\mathbf{F}$ , *body couple per unit volume*  $\mathbf{L}$ , and *energy supply density*  $\Phi$  of electromagnetic origin. The constitutive equations can be considered as coupling between the various electromagnetic field variables, also. In a general case, they are:

$$\mathbf{D} = \mathcal{D}(\mathbf{E}); \quad \mathbf{B} = \mathcal{B}(\mathbf{H}); \quad \mathbf{J} = \mathcal{J}(\mathbf{E}), \quad (6)$$

where  $\mathcal{D}, \mathcal{B}, \mathcal{J}$ , are general vector functions. In the most general case, even the coupling between electric and magnetic variables can be possible, e.g.  $\mathbf{J} = \mathcal{J}(\mathbf{E}, \mathbf{H})$ . There is a tendency to regard  $\mathbf{E}$  and  $\mathbf{B}$  fields as the basic variables for electric and magnetic fields in the vacuum so the constitutive laws can be rewritten by introducing two more variables for material media:

$$\mathbf{D} = \varepsilon_0 \mathbf{E} + \mathbf{P}; \quad \mathbf{B} = \mu_0 (\mathbf{H} + \mathbf{M}), \quad (7)$$

where  $\mathbf{P}$  is the polarization density and  $\mathbf{M}$  stands for the magnetization density.

### 3. The equations for moving media

In the case of moving media, the first difficulty is that several co-ordinate systems can be chosen as a reference co-ordinate system. The laboratory frame is regarded as inertial system and the intensity of the external electromagnetic field is usually given in this representation, so it seems obvious to describe all the electromagnetic phenomena in the laboratory frame.

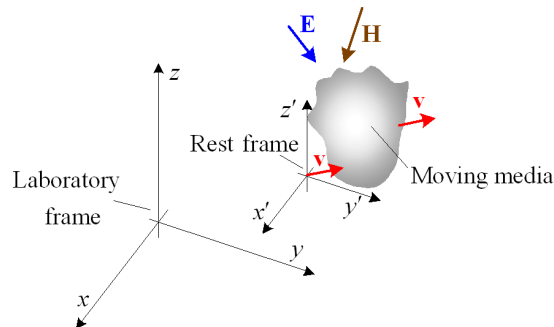


Figure 1. Laboratory frame and rest frame for describing the moving media

Unfortunately, the constitutive equations are known only for the material lying at rest. In addition, all the points of the deforming media may move by the velocity of their own, so there is no co-ordinate system in which the material body under investigation seems to be at rest. Naturally, one can choose a co-ordinate system in which one single point and its small surroundings are at rest and this system may be called rest frame (Fig. 1.). However, other areas of the body under investigation may be moving according to this so-called rest frame. Therefore, we must use at least two co-ordinate systems and some transformation equations for transforming the field variables from one co-ordinate system to the other. As the velocity is much smaller than the speed of light, the slow speed approximation of the Lorentz transformation can be used:

$$\mathbf{E}' = \mathbf{E} + \mathbf{v} \times \mathbf{B}; \quad \mathbf{D}' = \mathbf{D} + \mathbf{v} \times \mathbf{H}/c^2 \quad (8)$$

$$\mathbf{H}' = \mathbf{H} - \mathbf{v} \times \mathbf{D}; \quad \mathbf{B}' = \mathbf{B} - \mathbf{v} \times \mathbf{E}/c^2 \quad (9)$$

$$\mathbf{J}' = \mathbf{J} - q\mathbf{v}; \quad q' = q - \mathbf{v} \cdot \mathbf{J}/c^2 \quad (10)$$

Unfortunately, there are several problems with this approach:

The use of these transformation equations is self-evident in vacuum, but there are different commonly used formulations for transformation in the presence of matter. The Lorentz-, Maxwell- and Chu-formulations differ from each other not only in some notation but also in regarding the polarization and the magnetization relevant or irrelevant when defining the effective fields [9, 10].

The points of the deforming material body are moving with not a constant velocity, and no co-ordinate system fixed to an accelerating point can be rigorously considered as inertial system. On the other hand, the acceleration can be managed by postulating inertial forces and the relativistic effects can surely be neglected since the velocities are very small, compared to the speed of light.

#### 4. Electroactive polymer actuators under voltage

The model of an average EAP actuator can be imagined as a flat capacitor: a thin electroactive polymer layer coated on both side with compliant conductive film (Fig. 2.).

Therefore, charge and current can occur only on the surface, or more precisely in the plates of the capacitor.

In the EAPs, there are no free charges, no free currents and no magnetisable parts inside the material, except for the case of damage. This fact simplifies the Maxwell equations:

$$\text{curl } \mathbf{H} = \varepsilon_0 \frac{\partial \mathbf{E}}{\partial t} + \frac{\partial \mathbf{P}}{\partial t}, \quad \text{curl } \mathbf{E} = -\frac{\partial \mathbf{H}}{\partial t} \quad (11)$$

$$\text{div } \mathbf{H} = 0, \quad \text{div } \mathbf{P} = -\varepsilon_0 \text{div } \mathbf{E} \quad (12)$$

In addition, we can assume the lack of external magnetic field as the EAP actuators are usually used without external magnetic excitation. Unfortunately, it does not mean

that no magnetic phenomena would take place at all. When an EAP actuator is moving or changing its shape or changing its voltage, current is flowing and this current results in magnetic field according to the Ampère–Maxwell law.

In the next section, approximate evaluation will be given for the electromagnetic and mechanical variables of a common EAP actuator working under usual circumstances.

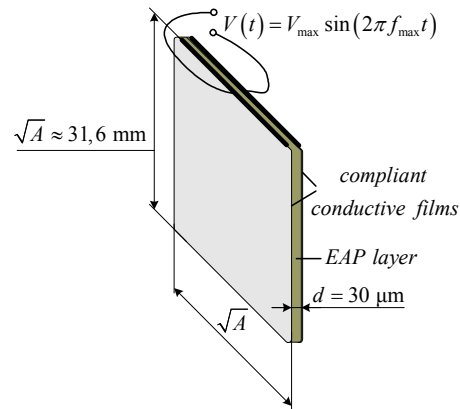


Figure 2. Model of the EAP actuator

## 5. Electromagnetic and mechanical conditions in an EAP actuator

In dielectric electroactive polymers (DEAP), actuation is caused by electrostatic force between the two electrodes. This force squeezes the polymer and because of its quasi-incompressibility, it expands in area due to the electric field.

Consider an actuator of this type with an area of  $10 \text{ cm}^2$ . The EAP film thickness can vary from several  $\mu\text{m}$  up to a few ten  $\mu\text{m}$  depending on the original thickness of the film and the prestretch. For a PolyPower Film under minimal prestretch,  $30 \mu\text{m}$  is adequate [11]. According to the engineering sheet of the PolyPower film [11], the maximum electric field strength is  $35 \text{ V}/\mu\text{m}$ . It results in a breakdown voltage of  $1050 \text{ V}$ . The capacitance and the capacitive energy can be calculated by the well-known formulae:

$$C = \varepsilon_0 \varepsilon_r \frac{A}{d} = 915 \text{ pF}; \quad E_C = \frac{1}{2} V^2 \varepsilon_0 \varepsilon_r \frac{A}{d} \quad (13)$$

The force, what an actuator of this type can exert is:

$$F = \frac{dE_C}{dd} = -\frac{V^2 \varepsilon_0 \varepsilon_r A}{d^2} = -33,6 \text{ N} \quad (14)$$

The incompressibility of the material has been taken into account due to the  $Ad = \text{const.}$  condition. This force is perpendicular to the capacitor's plate and results in compressing the polymer in thickness.



The external electric field is sinusoidal. The higher the frequency is, the more significant magnetic phenomena are expected. According to the experiments [6] (page 118), a few kHz is available as a maximum operating frequency. Assuming that the voltage applied on the device is sinusoidal and the capacitance does not change in time, the current is sinusoidal also:

$$I(t) = 2\pi f CV \cos(2\pi f t) \quad (15)$$

The maximum current happens to be  $I_{max} = 60.3$  mA at  $f_{max} = 10$  kHz. It causes a magnetic field inside the polymer. The field intensity is parallel with the conductive layers and perpendicular to the direction of the current (Fig. 3.).

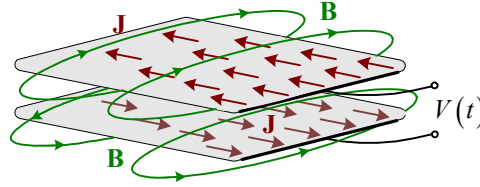


Figure 3. Magnetic induction due to the current flowing into the plate of the capacitor

$$H_{max} = \frac{I_{max}}{\sqrt{A}} = 1.91 \frac{\text{A}}{\text{m}}; \quad B_{max} = \mu_0 H_{max} = 2.1 \mu\text{T} \quad (16)$$

In addition, a magnetic field is induced due to the altering electric displacement. Its maximum equals:

$$H'_{max} = \frac{\dot{D}_{max}}{4\sqrt{A}} = \frac{2\pi f_{max} \epsilon_0 \epsilon_r V_{max}}{4\sqrt{A} \cdot d} = 477 \frac{\text{A}}{\text{m}}; \quad B'_{max} = \mu_0 H'_{max} = 0.6 \text{mT} \quad (17)$$

This contribution to the magnetic field is also parallel with the layers and reaches its highest amount near the edges of the EAP layer (Figure 4.).

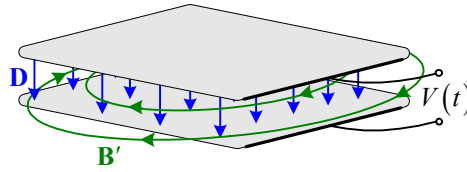


Figure 4. Magnetic induction due to the change of the electric displacement

The above calculations were all made under the assumption that there are no movements in the system. The EAP is considered incompressible, therefore the change of area due to the applied voltage is:

$$\Delta A = -\frac{F_{max}}{Y} = 0.31 \text{cm}^2 \quad (18)$$

Changing in area goes hand in hand with the acceleration and velocity of every single point in the material body. The maximum speed occurs at the edges of the actuator:

$$v_{\max} = \frac{|\Delta A|}{4\sqrt{A}} 4\pi f = \frac{V^2 \varepsilon_0 \varepsilon_r \sqrt{A}}{d^2 Y} \pi f = 30.3 \frac{\text{m}}{\text{s}} \quad (19)$$

After these calculations, we can estimate the terms of the Maxwell equations and the terms of the Lorentz transformation equations. The aim is to decide which terms can be neglected in the special case of dielectric electroactive polymers. In the formulae of the Lorentz transformation (8-10) the ratios of the terms are, as follows:

$$\frac{|\mathbf{v} \times \mathbf{B}|}{|\mathbf{E}|} = \frac{\mu_0}{2Y} \left( \frac{V \varepsilon_0 \varepsilon_r \pi f}{d} \right)^2 = 5.14 \cdot 10^{-10} \quad (20)$$

$$\frac{|\mathbf{v} \times \mathbf{H}|}{c^2 |\mathbf{D}|} = \frac{\varepsilon_0 \varepsilon_r}{2Y} \left( \frac{V \pi f}{dc} \right)^2 = 1.68 \cdot 10^{-10} \quad (21)$$

$$\frac{|\mathbf{v} \times \mathbf{D}|}{|\mathbf{H}|} = \frac{2V^2 \varepsilon_0 \varepsilon_r A}{d^2 Y} = 6.11 \cdot 10^{-5} \quad (22)$$

$$\frac{|\mathbf{v} \times \mathbf{E}|}{c^2 |\mathbf{B}|} = \frac{2V^2 A}{d^2 Y c^2 \mu_0} = 1.97 \cdot 10^{-5} \quad (23)$$

According to (20-23), the  $\mathbf{v} \times \mathbf{B}$  and the  $\mathbf{v} \times \mathbf{H}/c^2$  terms can surely be disregarded. Although  $\mathbf{v} \times \mathbf{D}$  and  $\mathbf{v} \times \mathbf{E}/c^2$  play a role higher by five orders of magnitude, they can be neglected too. Especially, when taking into account that our measurements of the constitutive equations can hardly be of the same accuracy.

For handling the coupled problem, it is essential to calculate the above-mentioned body force per unit volume  $\mathbf{F}$ , body couple per unit volume  $\mathbf{L}$ , and energy supply density  $\Phi$  of electromagnetic origin. The body couple equals zero, because of the lack of magnetisable particles. The body force and the energy supply happen to be the Lorentz force and the Joule heat, respectively:

$$\mathbf{F} = q_t \mathbf{E} + \mathbf{J}_t \times \mathbf{B}, \quad \Phi = \mathbf{J}_t \cdot \mathbf{E} \quad (24)$$

where  $\mathbf{J}_t$  stands for the total current density and  $q_t$  is the total charge density.

$$q_t = q - \nabla \cdot \mathbf{P}, \quad \mathbf{J}_t = \mathbf{J} + \frac{\partial \mathbf{P}}{\partial t} + \nabla \times \mathbf{M} + \nabla \times (\mathbf{P} \times \mathbf{v}) \quad (25)$$

(The last contribution occurs only according to the Lorentz formulation.) The free current, the free charge and the magnetization equal zero, the polarization is assumed homogeneous. Therefore, the total charge equals zero and the second and fourth terms of the total current density can be estimated as:

$$\left| \frac{\partial \mathbf{P}}{\partial t} \right| = (\varepsilon_r - 1) \varepsilon_0 \frac{V}{d} 2\pi f = 47.68 \frac{\text{A}}{\text{m}^2} \quad (26)$$

It can be multiplied by the area of the actuator and one gets a few ten milliamps, what is comparable with the free current flowing into the electrodes. Polarisation is assumed

to be homogenous inside the material, but velocity is linearly changing from one edge of the actuator to the other. Taking notice of only linear dislocation,

$$|\text{curl}(\mathbf{P} \times \mathbf{v})| = (\varepsilon_r - 1) \varepsilon_0^2 \varepsilon_r \frac{V^3}{d^3 Y} \pi f = 0.496 \frac{\text{A}}{\text{m}^2} \quad (27)$$

Finally, the current due to the movement of the charged electrodes must be estimated:

$$I'_{\text{max}} = \varepsilon_0^2 \varepsilon_r^2 \frac{V_{\text{max}}^3 A}{2d^3 Y} \pi f_{\text{max}} = 0.92 \text{ mA} \quad (28)$$

## 6. Conclusions

The calculations of the last section showed us which terms could be neglected in the (8-10) formulae of the Lorentz transformation and in the (25) formulae of the total current density and total charge density. According to (20-23), the  $\mathbf{v} \times \mathbf{B}$  and the  $\mathbf{v} \times \mathbf{H}/c^2$  terms can surely be disregarded. Although  $\mathbf{v} \times \mathbf{D}$  and  $\mathbf{v} \times \mathbf{E}/c^2$  play a role higher by five orders of magnitude, they can be neglected too.

On the other hand, the basis of these calculations was a special case of an electroactive polymer actuator. One can find different ratios when examining other types of EAP devices or similar devices under different conditions. All results depend on the working frequency, the relative dielectric constant, the maximum voltage and the thickness of the EAP layer. These can vary due to technological development; therefore, the estimations must be repeated for every single case.

The polarisation current and the current of the capacitor are of the same order of magnitude, so none of them can be neglected. The  $\text{curl}(\mathbf{P} \times \mathbf{v})$  term can be estimated as some percent of the polarisation current, so it cannot be disregarded either. Naturally, this term emerges only in the Lorentz formulation and this fact can be a basis for deciding by measures which formulation describes the real electromagnetic phenomena in the moving media.

## Acknowledgements

The research was supported by the Project BAROSS-ND07-ND-INRG5-07-2008-0062.

## References

- [1] Carlson, J. D., Jolly, M. R.: *MR Fluid, Foam and Elastomer Devices*, Mechatronics, 10 (2000), pp. 555–569.
- [2] Kordonsky, W.: *Magnetorheological Effects as a Base of New Devices and Technologies*, Journal of Magnetism and Magnetic Materials, 122 (1993), pp. 395–398.
- [3] Dorfmann, A., Ogden, R. W.: *Nonlinear Magnetoelastic Deformations of Elastomers*, Acta Mechanica, 167 (2004), pp. 13–28.

- [4] Brigadnov, I. A., Dorfmann, A.: *Mathematical Modelling of Magneto-sensitive Elastomers*, International Journal of Solids and Structures, 40 (2003), pp. 4659–4674.
- [5] Bustamante, R., Dorfmann, A., Ogden, R. W.: *On Electric Body Forces and Maxwell Stresses in Nonlinearly Electroelastic Solids*, International Journal of Engineering Science, 47 (2009), pp. 1131–1141.
- [6] Carpi, F. et al.: *Dielectric Elastomers as Electromechanical Transducers*, Elsevier, (2008).
- [7] Maugin, G. A.: *Continuum Mechanics of Electromagnetic Solids*, North-Holland, Amsterdam, (1988), pp. 95–117.
- [8] Kuczmann, M., Iványi, A.: *The Finite Element Method in Magnetics*, Akadémiai Kiadó, Budapest, (2008).
- [9] Aczél, Á.: *Electromagnetic Forces in Electroactive Polymers*, Acta Technica Jaurinensis 5/1 (2012), pp. 87–101.
- [10] Pao, Y. H.: *Electromagnetic Forces in Deformable Continua*, in: Mechanics Today, 4. Nemat-Nasser, S., Editor. Pergamon Press, (1978), pp. 209–306.
- [11] Danfoss: *Engineering sheet*, PCM 276 Single layer Un-metalized Polymer film (2009).

# A Comparative Analysis of Two Rotor Broken Bars/Rotor Faults Diagnosis Methods and the Influence of These Faults on Induction Motors Operating Parameters

A. Ciobanu<sup>1</sup>, E. Helerea<sup>1</sup>, S. Abagiu<sup>2</sup>

Transilvania University of Brasov , Faculty of Electrical Engineering and Computer Science<sup>1</sup>, Eroilor Street, No.29, 500036, Brasov, Romania,  
Transilvania Sud-Electrica Serv SA<sup>2</sup>,  
e-mail: anca.ciobanu@unitbv.ro, helerea@unitbv.ro, sabagiu@yahoo.com

**Abstract.** Rotor's integrity diagnosis is difficult and for induction motors producers represents a challenge, because they usually detect faults at the end of the manufacturing process which involves both material and labor loss. In this paper a comparative analysis of two rotor faults diagnosis methods and the influence of these faults on low voltage induction motors operating parameters were performed in order to establish the need of using each of these methods before the final motor testing on the production line. As samples were considered three identical rotors with a total of 22 bars, and a prototype stator designed for motors with rated power of 0.37 kW and speed of 1500 rpm.

**Keywords:** *induction motors, diagnosis methods, rotor broken bars/rotor faults, comparative analysis.*

## 1. Introduction

Induction motors made the subject of numerous studies, because they are widely used in industry such as in pumps, elevators, conveyors, winders, wind tunnels. For the last two decades, studies regarding fault diagnosis in the induction motors were accomplished and, in particular, a substantial research was dedicated to broken rotor bar faults and to their non-intrusive diagnosis techniques development [1]. According [2], broken rotor bar represents approximately 5% from induction motor faults and yet it is the most studied fault type. Since 1988 Kliman et. al [3], used the stator currents and voltages measurement method to detect the presence of broken rotor bar. As functions of induction motors became more complex, fault diagnosis methods were designed and improved [4, 5, 6]. Yet, the problem remains for the production stage, especially in mass production, when fast fault diagnosis methods are required.

Induction motor rotors are of two types: cast and fabricated. Previously, cast rotors were only used in small motors. However, with the advent of cast ducted rotors, casting technology can be used even for the rotors of motors in the range of 3000 kW [7].

Although die-cast cages are more durable and rugged than special fabricated cages they are impossible to repair after bar breakage or cracks [8].

The rotor of the squirrel cage induction machine consists of axial bars closed on both sides by end rings. Defective rotor bars such as broken bars and high resistance of rotors may have bad effects on the performance of the machine [9].

Rotor cage manufacturing influence the induction motors operating parameters and for this reason an early diagnosis of faults in the design and execution phase and then in the operation phase is necessary. Efficiency, slip, rated current, winding temperature rise, starting torque are the most important operating parameters affected. Usually, the poor quality of the rotor cage is observed at the final induction motor testing.

Besides casting machines development, a strict observation of the specified materials usage and casting technology, introducing a control filter for detecting the rotor cage faults are required.

To keep induction motor performance within acceptable limits and to reduce the failure rate, further investigations are needed to establish new manufacturing technologies, new power supply systems and adequate systems of control and testing, monitoring and diagnosis of motor operation [10].

This paper aims are a comparative analysis of two rotor faults diagnosis methods and the influence of these faults on induction motors operating parameters in order to establish the need of using each of these methods before the final motor testing on the production line. The paper is organized as follows: fault detection by measuring the rotor impedance, fault detection by measuring the induced current of a constant magnetic field, standard testing and conclusions.

## 2. Fault detection by measuring the rotor impedance

As samples were considered three rotor cages/rotors, designed for motors with rated power of 0.37 kW and speed of 1500 rpm, with a total of 22 bars. The cages marked S1, S2, S3 are the rotor cages/rotors without faults, the sample S21 is the rotor cage/rotor with one broken bar and the sample S22 is the rotor cage/rotor with two broken bars.

Two rotors were deliberately damaged by drilling holes in the bars and then used with the same stator, for a better accuracy of the tests (Fig. 1a, b).

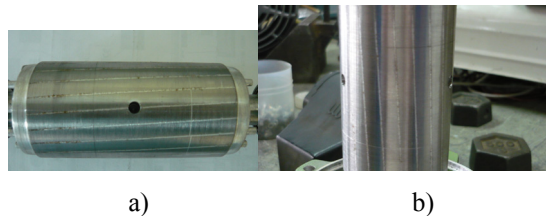


Figure 1. Induced rotor faults – a) One broken rotor bar; b) Two broken rotor bars.

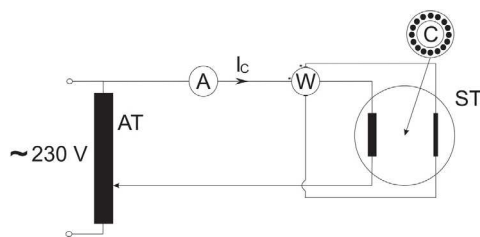


Figure 2. Schematic diagram for rotor cage/rotor impedance measuring

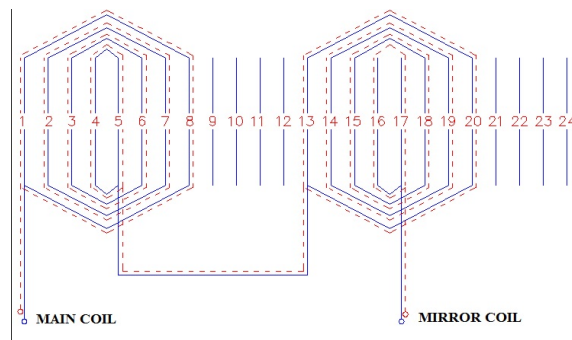


Figure 3. Stator winding scheme for cage/rotor size 63, speed 1500 rpm

The first rotor fault detecting method that was used is based on rotor cage/rotor impedance measuring. The measured impedance value is compared with a predefined value (previously established for cages/rotors considered accepted or for which induction motors parameters were good). Failure limit is given by the predefined value, so that all cages with a lower impedance value than the predefined one are accepted.

In Fig. 2 is shown a schematic diagram for impedance measuring, where AT is an autotransformer, A is an ammeter, W is a wattmeter, C is the testing cage/rotor and ST is a special wound stator made from two coils: the main coil and the mirror coil (Fig. 3). The ammeter is connected to the main coil and the wattmeter is connected to the mirror coil – measuring the electromotive voltage induced by the magnetic field created by the current coil.

The rotor cage is placed inside the supplied wound stator. Both stator current  $I_C$  (A) and power  $W_C$  (W) are read from the measurement devices. The equivalent resistance of the circuit  $R_2'$  ( $\Omega$ ) can be interpreted as the equivalent resistance of the cage/rotor and is calculated with [11]:

$$R_2' = \frac{W_C}{I_C^2} \tag{1}$$

This method can be successfully used in the production line where a quality control is introduced by detecting rotor cages faults before the shaft pressing.

The advantages of these methods are:

- The low cost;
- Its simplicity;
- The possibility of manufacturing of the special wound stator in the production line;
- It can be used for any low voltage induction motor size;
- It can be used for prototype rotors.
- The drawbacks of this method are:
- The need to design and manufacture of special wound stator for each motor size and speed, to be able to verify all the rotor cages in the production line;
- Impossibility of cage/rotor fault type identification;
- Rotor cages must be deburred before testing because aluminum surplus influences the equivalent resistance of the cages/rotors.

The equivalent resistances determined by this method are presented in Table 1. After comparing test results with the predefined resistance value, it was established that all rotor cages/rotors are accepted. It was observed that the resistance decreased significantly after rotor cages deburring. Even in the case of two broken bars the resistance is within the imposed limit, which means that this method it is not accurate for this type of fault.

Table 1. Rotor cage / rotor impedance values

Samples	Rotor cage			Rotor			$R_2'$
	$I_c$	$W_c$	$R_2'$	$I_c$	$W_c$	$R_2'$	
S1	1.5	51.625	22.94	1.5	45	20	25
S2		51.75	23		45.525	20.23	
S3		56.25	25		46.12	20.49	
S22	-	-	-	51	22.66		

Fault detection by measuring the induced current of a constant magnetic field

For the second used method, the working principle is based on the detection of a signal proportionate to the induced current, generated in the bars of the rotor cage, when they cross a continuous magnetic field.

Faults that can be detected with this method are:

- Broken rotor bars;
- Blowholes or porosity;
- Wrong inclination angle of bars;
- Low quality of aluminium alloy;
- Leakage between laminations;
- Gluing of bars to laminations;
- Magnetic retentivity.

The sensor, using its internal permanent magnets, generates a continuous magnetic flux between its polar expansions. The rotor cage/rotor is fixed between lock peaks and alignment of an automated rotating device. After closing the protecting element, rotor cage/rotor rotates so that its bars cross this magnetic flux generated by the sensor. The result is the generation of an induced current inversely proportional to the ohmic



resistance of the rotor cage/rotor in the bars. The induced current generates an inverse flux proportional to its intensity.

On this method is based the die-cast rotor cages testing system 06/M from Risatti Instruments.

This testing system is particularly indicated for laboratory tests or for statistical control of the production.

The electromotive voltages are captured by the special windings of the 60/M system which transforms the flux into an electrical signal. The signal is then amplified and viewed on the system's display device. The constant amplitude of all displayed signals means the absence of faults, whilst the reduction of amplitude of one or more signals or, the complete absence of some signals is the indication of faults.

For the results evaluation, the curves obtained in the test are compared with the system standard curves. It has to be kept in mind that often, various faults are combined together and generate curves that are slightly different than the system's standard curves.

The drawback of this method is: in order to test rotor cages/rotors for sizes up to 80 it is necessary to purchase another system.

In Fig. 4 is shown the sample S1 without broken rotor bar fault, in Fig. 5 the sample S3 without broken rotor bar fault, in Fig.6 the sample S2 without broken rotor bar fault, in Fig. 7 the sample S21 with one broken bar fault and in Fig. 8 the sample S22 with two broken bars fault.

It can be observed that for the samples without major faults the amplitude is kept in limits and for the samples with one/two broken bars the amplitude increases in the area where the fault occurs.

The system 06/M also detects broken rotor bars fault by indicating the unaffected number of bars. The small amplitude difference for the samples S1, S2, and S3 is due to magnetic remanence.

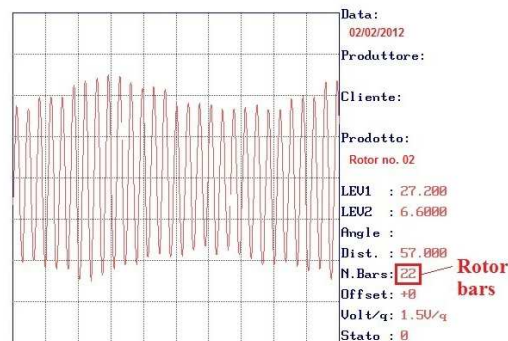


Figure 4. Sample S1 without broken rotor bar fault

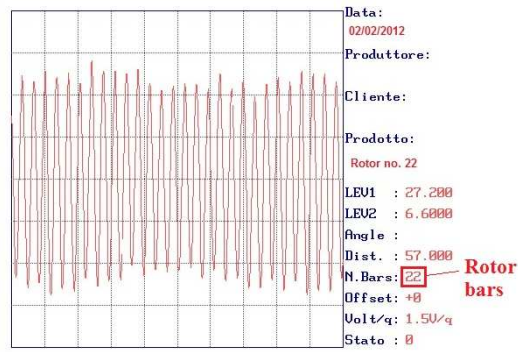


Figure 5. Sample S3 without broken rotor bar fault

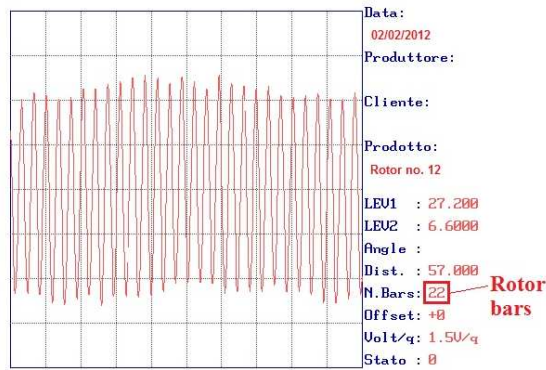


Figure 6. Sample S2 without broken rotor bar fault

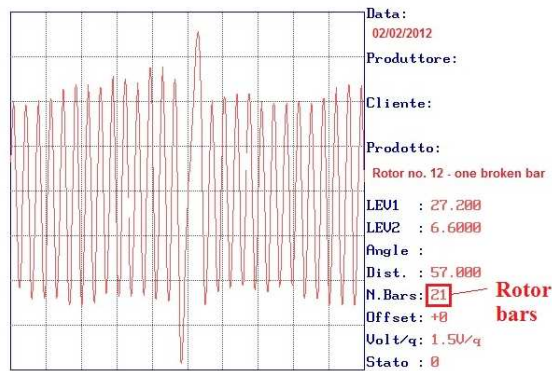


Figure 7. Sample S21 with one broken bar fault

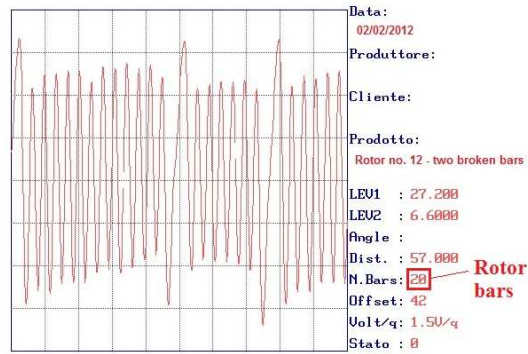


Figure 8. Sample S22 with two broken bars fault

### 3. Standard testing

The same prototype stator, designed for motors with rated power of 0.37 kW and speed of 1500 rpm, was used for each tested rotor.

No-load, short-circuit and load tests were performed.

The following parameters were determined:

- Induction motors resistance at the laboratory,  $R_{20}$  ( $\Omega$ );
- No-load current,  $I_0$  (A);
- No-load power,  $P_0$  (W);
- Short-circuit current,  $I_k$  (A);
- Short-circuit power,  $P_k$  (W);
- Torque ratio,  $M_p/M_n$ ;
- Current ratio,  $I_p/I_n$ ;
- Rated current,  $I_n$  (A);
- Efficiency,  $\eta$  (%);
- Power factor,  $\cos\phi$ ;
- Slip,  $s$  (%);
- Winding temperature rise,  $\Delta\theta$  ( $^{\circ}\text{C}$ ).

Table 2. Induction motors operating parameters

Motors parameters	Motor samples				
	M1	M3	M2	M21	M22
$R_{20}$	26.25				
$I_0$	0.84	0.865	0.9	0.9	0.91
$P_0$	96	102	105	104	110
$I_k$	3.57	3.53	3.67	3.55	3.28
$P_k$	2040	2070	2090	2030	1860
$M_p/M_n$	2.53	2.45	2.2	2.55	2.58
$I_p/I_n$	3.25	3.1	3.25	3.09	2.78
$I_n$	1.1	1.4	1.13	1.15	1.18
$\eta$	64.22	61.97	63.57	62.59	61.56
$\cos\phi$	0.745	0.758	0.74	0.71	0.735
$s$	14.8	15.53	15.33	16.2	17
$\Delta\theta$	77	85	84	87	89.5

In Table 2 the induction motors operating parameters are presented – without broken rotor bar fault for samples M1, M2, M3 one broken rotor bar for sample M21 and two broken rotor bars for sample M22.

The obtained data indicate that the rotor cage/rotor with the lowest resistance value determine maximum performances for the induction motor.

Following the made analysis for the motors noted M2, M21 and M22 the observations are:

- The short-circuit current, short-circuit power and efficiency decrease with the increasing of the broken rotor bars number, because the rotor resistance also increases;
- The torque ratio, rated current, slip and winding temperature rise increases with the increasing of the broken rotor bars number, because the rotor resistance and cage rotor losses increase.

#### 4. Conclusions

The induction motors were made with the same tested rotors for a better accuracy of the tests. For each diagnosis method the advantages and the drawbacks were pointed. The main conclusion is that the methods should be used together on the production line for a better rotor faults filtering: the first method can be used for any low voltage motor size and prototype rotors at a cheap cost and the second one to test rotors in serial production.

The standard testing of the motor can be seen from two points of view:

- To establish the resistance limit for prototype rotors;
- To establish the significance of the broken rotor bars/rotor faults on low induction motors.
- The influence of the broken rotor bar on the low voltage induction motor behaviour in terms of stator and rotor currents, torques, losses and motor heating will be analyzed and studied as next work in this field.

#### Acknowledgment

This paper is supported by the Sectoral Operational Programme Human Resources Development (SOP HRD), ID76945 financed from the European Social Fund and by the Romanian Government.

#### References

- [1] Mehrjou, M. R., Mariun, N., Marhaban, M. H., Misron, N.: *Rotor fault condition monitoring techniques for squirrel-cage induction machine – A review*, Mechanical Systems and Signal Processing, No. 25 (2011), pp. 2827–2848.
- [2] IEEE Committee Report, *Report of large motor reliability survey of industrial and commercial installations*, Part I and Part II, IEEE Trans. Ind. Applicat., vol. IA-21, (1985), pp. 853–872.

- [3] Kliman, G. B., Koegl, R. A., Stein, J., Endicott, R. D.: Madden M. W.: *Noninvasive Detection of Broken Rotor Bars in Operating Induction Motors*, IEEE Trans on Energy Conversion, Vol. 3. No. 4., (1988), pp. 873–879.
- [4] Fiser, R., Ferkolj, S.: *Application of a Finite Element Method to Predict Damaged Induction Motor Performance*, IEEE Transactions on Magnetics, Vol. 37., No. 5., (2001), pp. 3635–3639.
- [5] Ying, X.: *Characteristic Performance Analysis of Squirrel Cage Induction Motor With Broken Bars*, IEEE Transactions on Magnetics, Vol. 45., No. 2., (2009), pp. 759–766.
- [6] Cabanas, M. F., Pedrayes, F., Melero, M. G., Rojas García, C. H., Cano, J. M., Orcajo, G. A., González Normiella, J.: *Unambiguous Detection of Broken Bars in Asynchronous Motors by Means of a Flux Measurement-Based Procedure*, IEEE Transactions on Instrumentation and Measurement, Vol. 60., No. 3., (2011), pp. 891–899.
- [7] Wen, X.: *A hybrid intelligent technique for induction motor condition monitoring*, PhD Thesis, Institute of Industrial Research University of Portsmouth, (2011).
- [8] Bellini, A.: *Advances in Diagnostic Techniques for Induction Motors*, IEEE Transactions on Industrial Electronics, Vol. 55. No. 12., (2008), pp. 4109–4126.
- [9] Jung, Y.-B., Yoon, S.-B., Im, D.-H.: *The fault diagnosis of rotor bars in squirrel cage induction motors by time-stepping finite element method*, IEEE Transactions on Magnetics, Vol. 33., (1997), pp. 2131–2134.
- [10] Ciobanu, A., Helerea, E., Ioannides, M. G.: *Effects of voltage variation on the induction motor performances*, Proceedings of the 6th International Conference on Interdisciplinarity in Education ICIE'11, (2011), pp. 272–278.
- [11] Nicolaide, A.: *Electrical Machines – Theory – Design*, (In Romanian: Masini electrice – Teorie – Proiectare). Ed. Scrisul Romanesc, Craiova, Romania, (1975).

# Coupling Factor Calculation of Low Frequency RFID Systems by the Mutual Inductance Effective Permeability Method

P. Csurgai, M. Kuczmann

Széchenyi István University, Lab. Of Electromagnetic Fields, Dept. of Automation, Hungary

**Abstract.** A typical wireless energy or data transfer system consists of two inductors that are coupled through the mutual magnetic field. The performance of the system is determined by the  $k$  coupling factor which represents the linkage between the two coils. The paper introduces a new method for the calculation of the coupling factor in a time efficient way using the sensitivity parameter.

**Keywords:** *Coupling factor, Transponder coil, Sensitivity, Effective permeability, LF RFID*

## 1. Introduction

The RFID (Radio Frequency Identification) system or a typical wireless energy or data transfer system consists of two inductors that are coupled through the mutual magnetic field. The performance of the system is determined by the  $k$  coupling factor which represents the linkage between the two coils [1]. The operating distance is defined by the coupling factor therefore it is essential for the design of the RFID system to know the behaviour of the  $k$  as a function of distance. The sensitivity parameter of the transponder coil allows the calculation of the distance dependent coupling factor in a time efficient way. The sensitivity of the transponder coil can be calculated by the mutual inductance effective permeability method [2].

In the first part of the paper an introduction will be given about the LF RFID transponder coils and their properties specifically about the sensitivity parameter. In the second part the calculation of the sensitivity will be described using the mutual inductance effective permeability method. In the third part the coupling factor calculation will be introduced using the sensitivity parameter, and in the fourth part verification of the calculation method is presented using market available transponder coils.

## 2. Transponder coil properties

The transponder coil structure and properties are very similar to a general purpose inductor. Its main part is the magnetic, mostly ferrite core which the active component of the inductor is. The winding is placed around the core, which works as a bobbin and

holds the wire turns in the desired place. The termination of the inductor provides on one hand the wire joint and on the other hand soldering leads which will fix the component to the circuit board. Just like any general purpose inductor the main parameters of the transponder coil are the inductance ( $L$ ), quality factor ( $Q$ ), resistance ( $R$ ) and self resonance frequency (SRF). However the main function of the transponder coil is to provide an inductive coupling to another inductor, therefore a new parameter was introduced which describes the ability to create link through the magnetic field. This parameter is the sensitivity which is defined as follows:

$$S = \frac{U_i}{B} \quad (1)$$

where  $U_i$  is the induced voltage and  $B$  is the magnitude of the changing magnetic field. The inductor shall be placed in a changing (periodically in magnitude) uniform magnetic field. The magnetic flux that flows through the component will induce certain voltage. The ratio of the induced voltage across the coil and the magnitude of the changing magnetic field that induces the voltage is the sensitivity. The parameter describes how sensitive the inductor to the external magnetic field is [3].

The real performance of the transponder in the application is described by the coupling factor. It is used to evaluate the performance of the RFID system, but that parameter is influenced not only by the transponder coil, but by the reader coil as well. Different coupling values of different transponder constructions might reveal the difference in performance, but it will not give precise information. The sensitivity parameter allows the reliable evaluation and comparison of different coil constructions, because it describes only the transponder component.

### 3. Calculation of sensitivity

Calculation of the sensitivity is not possible by analytic mathematical formulas due to the used shape and materials of the components of the inductor. The components on one hand have different permeability (magnetic core has relative high permeability compared to the used other materials or the surrounding parts and air), and on the other hand the shapes can be very complex. A Finite Element Method based calculation technique was developed to get the sensitivity value of a transponder coil. The sensitivity calculation consists of 4 main steps as follows:

1. The first step of the above mentioned method is solving the Maxwell's equations numerically on the problem region where the transponder coil is located. For the calculation the Maxwell's equations can be simplified. The time varying parts of the equations can be neglected as well as the electric field calculation. This simplifies the problem to static magnetic problem as shown in the Fig 1., with the following governing equations:

$$\nabla \times H = J \quad (2)$$

$$\nabla \cdot B = 0 \quad (3)$$

in region  $\Omega_0$  and  $\Omega_m$ , where  $H$  is the magnetic field intensity,  $B$  is the magnetic flux density,  $J$  is the source current density of the exciting coil, which is equal to zero during





not important from the sensitivity or coupling factor calculation point of view. The average magnetic flux density calculation uses the  $B$  field computed in the first step, as can be seen in Fig. 2.

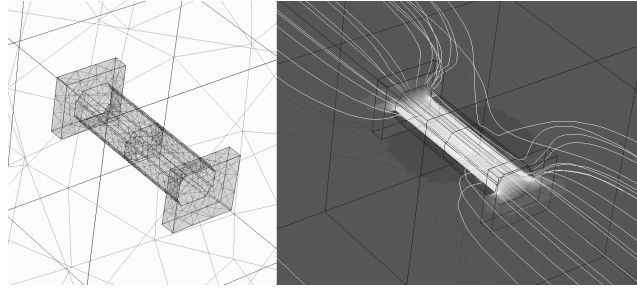


Figure 2. Example of sensitivity calculation of a transponder coil.

3. Third step is the calculation of mutual inductance effective permeability. The ratio of the average magnetic flux density in the core  $B_m$ , and the reference magnetic field strength on the boundary  $H_E$ , results the mutual inductance effective permeability parameter, denoted by  $\mu_{M\_eff}$ :

$$\mu_{M\_eff} = \frac{B_m}{\mu_0 H_E} \quad (9)$$

The  $\mu_{M\_eff}$  represents how the magnetic core in the inductor construction influences the mutual inductance. The higher the  $\mu_{M\_eff}$  value the higher the impact of the magnetic core and so the higher the mutual inductance is.

4. Final step is the calculation of the sensitivity using the previously calculated  $\mu_{M\_eff}$ . The sensitivity  $S$  of the transponder coil is proportional to the number of turns  $N$  of the coil, the angular frequency  $\omega$  of the external magnetic field, the cross sectional area of the winding (in most cases the cross sectional area of the magnetic core)  $A$  and the mutual inductance effective permeability  $\mu_{M\_eff}$ :

$$S = N\omega A\mu_{M\_eff} \quad (10)$$

#### 4. Coupling factor of transponder – reader inductor pairs

The coupling factor is used to determine the performance of the wireless energy and data transfer systems in order to define the maximum operating distance, or to evaluate the function of the system in certain distances. The coupling factor is defined as follows:

$$k(s) = \frac{U_{Transponder}(s)}{U_{Reader}} \sqrt{\frac{L_{Reader}}{L_{Transponder}}} \quad (11)$$

where  $k(s)$  is the distance dependent coupling factor,  $U_{Transponder}$  is the voltage across the transponder coil,  $U_{Reader}$  is the voltage across the reader coil,  $L_{Transponder}$  is the inductance

of the transponder coil and  $L_{Reader}$  is the inductance of the reader coil during the coupling factor measurement.

The value of the coupling factor is not constant, it changes with the orientation and the distance of the transponder and reader coils. The position and the orientation of the transponder coil from the reader point of view can be random during the standard operation of the system. However in the design phase of the RFID system only the in-line orientation of the transponder coil is evaluated, that is positioned on the symmetry axis of the reader coil, as shown in Fig. 3. This kind of set-up represents a best case situation, which is used during the component selection of the RFID system or the development of the system components.

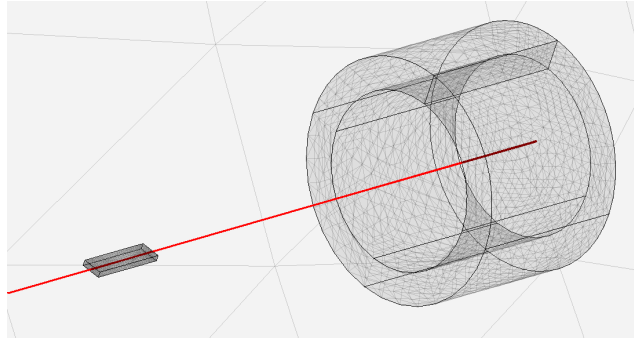


Figure 3. Best case configuration of Reader-Transponder coil pair.

In the ordinary calculation method of the  $k(s)$  the observed distance range between the transponder and reader coil shall be quantized and every distance step is calculated. This kind of calculation is very time consuming because each step requires the same amount of computation time. Considering a larger problem region and complex geometry structures with different permeability materials the computation time can be very high. If the resolution of the distance increases the time requirement of the computation also increases proportionally. In the proposed novel calculation technique the  $k(s)$  function is determined by a more time efficient method. In the far field region of the reader coil the magnetic field can be simplified to uniform in direction, and for practical purposes the magnitude of the field can be assumed as constant. By these simplifications the magnetic field of the reader coil in far field region in a close distance of the transponder coil's location is identical to the magnetic field defined for the sensitivity parameter. Therefore the magnetic flux density and so the total magnetic flux can be approximated using the sensitivity parameter of the transponder coil.

The ordinary calculation of the coupling factor requires as many FEM problem computations, as many distance steps there are. By the new method only two FEM problem computations are required regardless how many distance steps shall be calculated. In the first FEM computation the sensitivity of the transponder coil is calculated, in the second FEM computation the magnetic field strength of the reader coil is calculated. In the second computation the problem does not include the transponder coil, the resulting magnetic field strength (function of distance) describes purely the reader coils field.

**5. Verification of the calculation method**

Market available transponder and reader coils were chosen for the verification, in two different case sizes [6]. The coupling factor is independent of the inductance value of the transponder coil, therefore only one inductance value was tested per case sizes. The calculated magnetic field strength of the reader coil can be seen in Fig. 4. The figure represents the value of the H field on the symmetry axis of the reader coil as a function of distance from the coil.

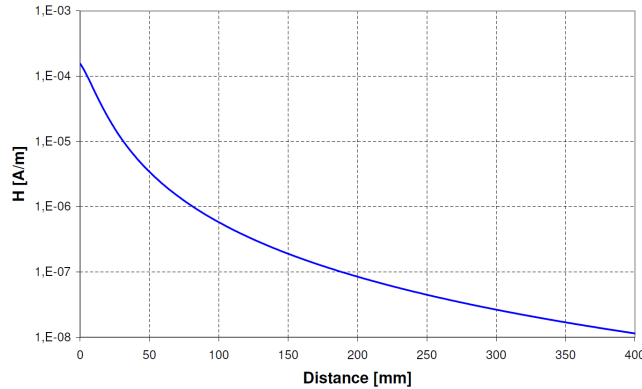


Figure 4. Calculated magnetic field strength of a reader coil.

Verification measurement of the coupling factor was performed using the above introduced reader coil and two different transponder coil constructions. The results of the measurement and comparison of the measured and calculated values can be seen in Fig. 5.

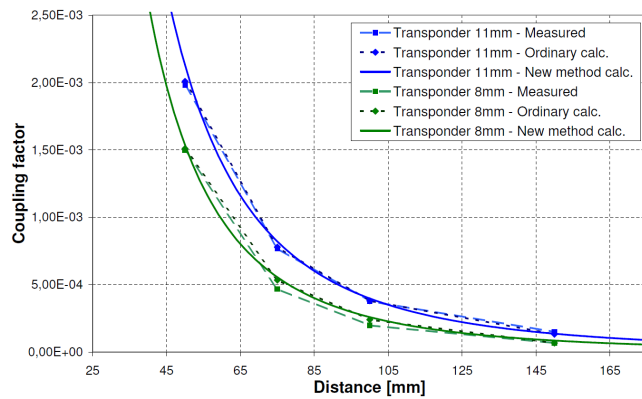


Figure 5. Comparison of coupling factor calculation with measurements.

**6. Conclusion**

The design process of the antenna components of the low frequency RFID system requires a fast approach where the efficiency of the components can be approximated. An optimization process where the geometries or the used materials are modified is not

able to use a slow and time consuming coupling factor calculation method. The above presented method consists of only two static FEM problem solving which requires much less time compared to the ordinary method where all the distance steps of the reader-transponder coil configuration are calculated. The strength of the method is the simplicity and speed. If the sensitivity parameter of the transponder coil or the magnetic field strength distribution of the reader coil is known by measurement or by other calculation method, they can be applied also in this calculation method improving the speed of the calculation. The accuracy of the method showed very good results during the validation of the method. The difference between the calculated and measured values is inside the measurement tolerance range of the used instruments.

## References

- [1] Finkenzerler, K.: *RFID Handbook*, Carl Hanser Verlag, Munich/FRG, (1999).
- [2] Csurgai, P., Kuczmann, M.: *Sensitivity calculation of LF RFID Transponder coil by the mutual effective permeability method*, Pollack Periodica Vol. 6., No. 2., (2011), pp. 3–12.
- [3] Csurgai, P., Kuczmann, M.: *Advanced Sensitivity measurement of Low Frequency RFID Transponder coils*, Acta Technica Jaurinensis, Vol. 3, No. 1., (2010), pp. 87–98.
- [4] Kuczmann, M., Iványi, A.: *Finite Element Method in Magnetics*, Academic Press, Budapest, (2008).
- [5] Matthew, N., Sadiku, O.: *Numerical Techniques in Electromagnetics*, CRC Press Inc. (1992).
- [6] EPCOS AG, Transponder coils selection guide, <http://www.epcos.com/web/generator/Web/Sections/ProductCatalog/Inductors/Inductors/TransponderCoils/Page,locale=en.html>

# Induction Machine: Comparison of Motor and Generator Characteristics

M. Hadžiselimović<sup>1,2</sup>, I. Zagradišnik<sup>2</sup>, B. Štumberger<sup>1,2</sup>

University of Maribor, Faculty of Energy Technology<sup>1</sup>  
Hočevarjev trg 1, SI-8270 Krško, Slovenia

University of Maribor, Faculty of Electrical Engineering and Computer Science<sup>2</sup>  
Smetanova 17, SI-2000 Maribor, Slovenia, e-mail: miralem.h@uni-mb.si.

**Abstract.** The aim of this paper is to present the difference of induction machine electromechanical characteristics in motor and generator operating modes. Firstly, the paper presents analytically derived equations, which are based on equivalent circuit and are used for calculation of induction machine breakdown torque. Secondly, a comparison of calculated and measured characteristics in motor and generator operating regimes is presented. Results of torque characteristics measurements, temperature rise tests and load tests are also provided. Finally the difference between the calculated and the measured results is commented on and explained in detail.

*Keywords:* induction machine, motor, generator, analytical calculation, measurements

## 1. Introduction

In some electrical drives the induction machine can operate as a motor and as a generator (for example: elevators, electric vehicles, pumped storage power plants etc.). In such drives the key question is which nominal power of the induction machine is the right one. Namely, the nominal mechanical power written on the nominal plate of an induction motor is not the same as in a generator mode of operation. The reason lies in the shape of torque characteristics of the induction machine. Breakdown torque is not the same in motor and generator modes. Normally the generator breakdown torque is two to four times greater than the motor breakdown torque. The slope of torque characteristics is therefore also not the same in both modes. For the same torque value the generated rotor losses in the generator mode of operation are significantly lower than in the motor mode of operation. Consequently, the nominal power of the same induction machine in the generator mode of operation can be significantly higher than in the motor mode of operation.

Engineers and researches use different models and techniques for designing electrical machines which include magnetically nonlinearities of iron core [1, 2]. Ordinarily they use numerical or analytical approach, sometimes both of them [3-5]. This work provides an explanation of the analytical approach for the calculation of induction machine's characteristics in motor and generator modes of operation. This paper focuses on key equations for the calculation of breakdown torque based on induction motor's

equivalent circuit [4, 6] and the calculation of all electrical and mechanical values at nominal power.

**2. Induction machine torque characteristics – theoretical background**

Induction machines can operate in different modes according to the torque characteristic. There are three known operating modes: breaking mode for slip values between  $\infty$  and 1, motor mode for slip values between 1 and 0, and generator mode for slip values between 0 and  $-\infty$ . All three operating modes are as part of torque characteristic shown in Figure 1.

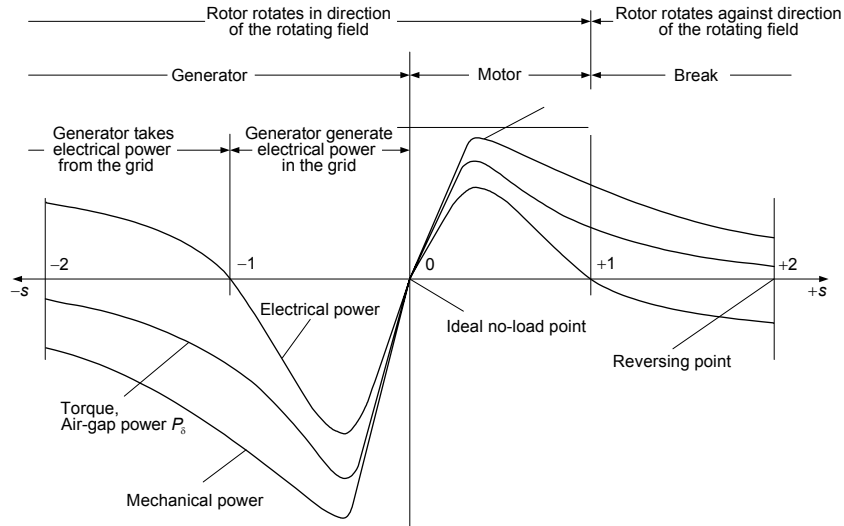


Figure 1. Induction motor torque and power characteristics

During the operation of the induction machine power losses generation is reflected in temperature rise, which can be different for motor and generator modes of operation. Direction of energy flow and the corresponding Sankey diagram, including power losses presentation, are shown in Figure 2.

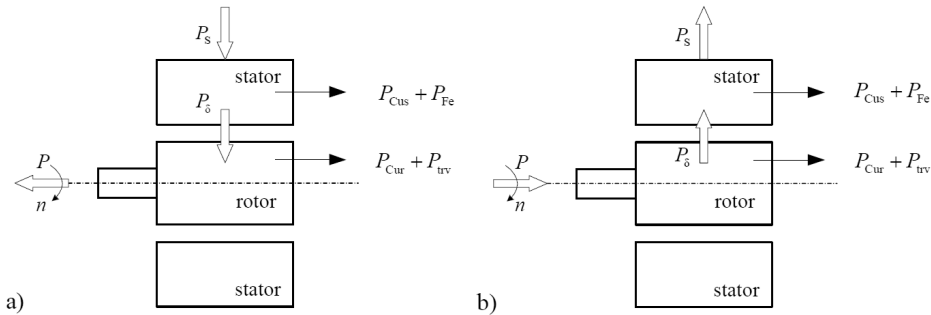


Figure 2. Energy flow Sankey diagram: a) motor mode, b) generator mode

In the process of designing an induction machine it is very important to calculate precisely the electrical and mechanical values in the breakdown torque point. The latter can be calculated with equation (1), which is deduced based on the equivalent circuit [6] of the induction motor (Figure 3):

$$T_b = \pm \frac{m_s p U_s^2}{\omega 2D} \quad (1)$$

where the operator  $\pm$  enables the calculation of the breakdown torque in the motor mode (the + sign) and in the generator mode (the – sign),  $m_s$  is the number of stator winding phases,  $p$  is the number of pole pairs,  $U_s$  is the stator winding voltage,  $\omega$  is the angular frequency and the denominator  $D$  represents:

$$D = \pm ((R_s - \chi_2 X'_{\sigma r}) \chi_1 + (X_{\sigma s} + \chi_1 X'_{\sigma r}) \chi_2) + \chi \sqrt{(R_s - \chi_2 X'_{\sigma r})^2 + (X_{\sigma s} + \chi_1 X'_{\sigma r})^2} \quad (2)$$

In equation (2) the sign  $\pm$  dictates the solution of the quadratic equation and the local extremes of the torque characteristic, where elements  $\chi_1$ ,  $\chi_2$  and  $\chi$  represent the correction factors for the calculation of the breakdown point:

$$\chi_1 = 1 + \sigma_s + d_1 \quad (3)$$

$$\chi_2 = a_1 - b_1 \quad (4)$$

$$\chi = \sqrt{\chi_1^2 + \chi_2^2} \quad (5)$$

In equation (3)  $\sigma_s$  is the factor of stator leakage, described by (6):

$$\sigma_s = \frac{X_{\sigma s}}{X_m} \quad (6)$$

and  $a_1$ ,  $b_1$  and  $d_1$  are the corresponding proportions obtained from the equivalent circuit:

$$a_1 = \frac{X_{\sigma s}}{R_{Fe}} \quad (7)$$

$$b_1 = \frac{R_s}{X_m} \quad (8)$$

$$d_1 = \frac{R_s}{R_{Fe}} \quad (9)$$

Equation (1) and the corresponding formulas of elements from equations (2) to (9) enable an analytical calculation of breakdown torque values.

### 3. Tested induction machine

In this paper the small squirrel cage induction machine with nominal power 5.5 kW and shaft height of 132 mm according to IEC was used. The induction machine was designed for a small bio-gas power plant where a gas motor is used as a turbine. The tested machine works in power plant as induction generator and is water-cooled with the temperature of water between 50 and 60 degrees Celsius and a corresponding flow of approximately 8 l/min. The water cooling system is spiral shaped and built into the stator housing. The induction machine is designed and built for an F insulation class. Thus a standard stator and rotor lamination with a combination of 36/48 slots made by lamination manufacturer Kienle + Spiess GmbH (IEC 132-4 1248) is used as the basis for the construction. Figures 4a and 4b present the shapes of the stator slot and the rotor slot respectively. The stator and rotor lamination are made from steel material M700-50A, which has 5.7 W/kg of specific core losses at 1.5 T.

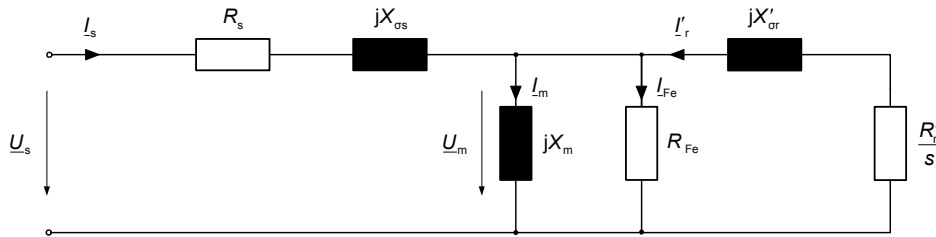


Figure 3. Induction motor equivalent circuit

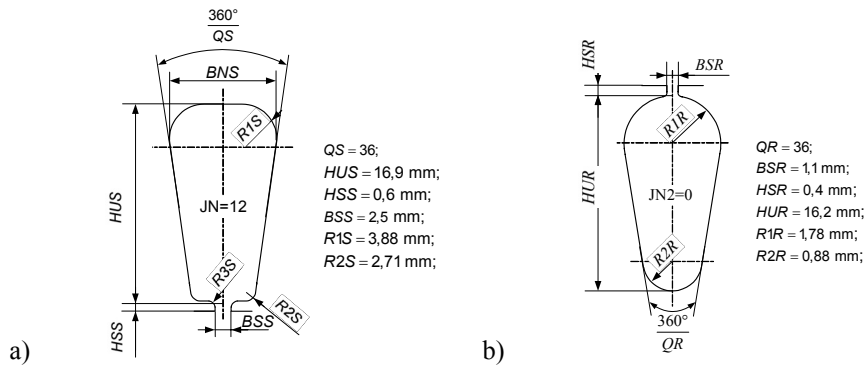


Figure 4. a) Cross-section of stator slot, b) cross-section of rotor slot

Table I. Values in the motor mode, power 5.5 kW, voltage Y 400 V and winding temperature 95 °C

$I$ (A)	$\cos \varphi$	$\eta$	$n$ ( $\text{min}^{-1}$ )	$T_N$ (Nm)	$T_b$ (Nm)	$P_{loss}$ (W)
11.18*	0.905	0.785	1420	37	88	1500
10.63	0.909	0.821	1419	37	89	1200

Remark: \* measured results



Table II. Values in the generator mode, power 5.5 kW, voltage Y 400 V and winding temperature 95 °C

$I$ (A)	$\cos \varphi$	$\eta$	$n$ ( $\text{min}^{-1}$ )	$T_N$ (Nm)	$T_b$ (Nm)	$P_{\text{loss}}$ (W)
9.95*	0.801	0.825	1556	41.3	365	1140
9.49	0.845	0.864	1560	39.3	233	875

Remark: \* measured results

#### 4. Comparison of measured and calculated results

All presented measurements in this paper were performed by classical induction machine measurement system shown in Figure 5. It consists of tested induction machine mechanically connected by clutch with active load machine, which one is speed controlled by converter via position sensor. Tested induction machine torque is measured via force sensor by reaction method. All electrical and mechanical values of tested induction motor are measured by power analyzer which ones via GPIB interface send measured results to personal computer where analysis of measured data is performed.

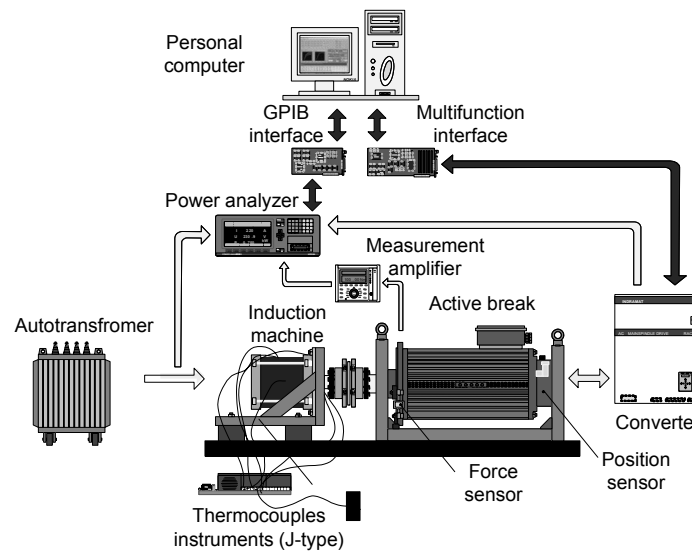


Figure 5. Measurement system

For temperature measurement the J-type thermocouples with corresponding instruments were used. Distribution of the thermocouples inside and on the surface of the induction machine housing is shown in Figure 6.

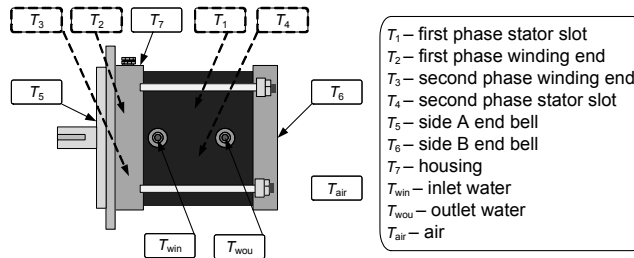


Figure 6. Measurement of temperatures on motor's housing

Figure 7 shows the measured and the calculated torque and current characteristics of the tested induction machine with nominal power 5.5 kW. From the presented characteristics it is evident that the breakdown torque in the generator mode is greater than the breakdown torque in the motor mode. From the measurements we obtain 88 Nm (at  $\approx 1050$  rpm) breakdown torque of the machine in the motor mode and in the 365 Nm (at  $\approx 2170$  rpm) breakdown torque in the generator mode, i.e. with slip  $s = 0.3$  or  $s = -0.47$ . It turned out that the measured breakdown torque in the generator mode is about 4 times larger than in the motor mode.

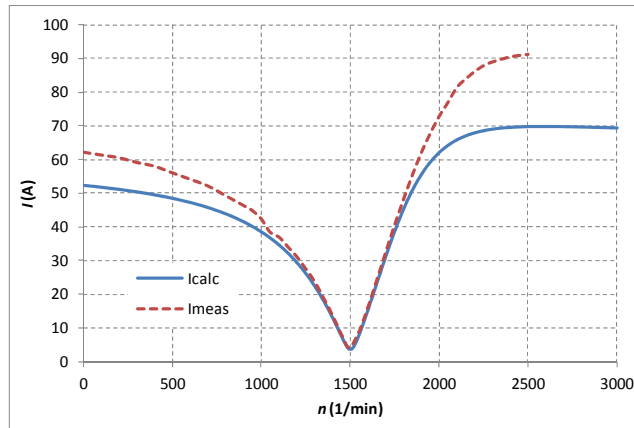


Figure 7. Measured and calculated current characteristics

To calculate the characteristics of the three-phase induction machine, we used the emLook software, which enables “click calculation” of characteristics. The calculation software package uses a standard equivalent circuit (Figure 3) stated in IEC 60034-28 as a basis. The measurement and the calculation (with emLook) results for the machine are provided in Table I for the motor operation mode and in Table 2 for the generator operation mode.

A comparison of the measurement and the analytical calculation data shows a significant difference between the two in the generator breakdown torque. The measured breakdown torque in the generator operating mode is about 4 times larger than in the motor operating mode. An analytical calculation of the breakdown torque with equation (1) for equivalent circuit (Figure 3) however returns only a 2.6 times

higher value for the generator than for the motor. There are several reasons for the much higher measured value of the breakdown torque  $T_b$  than the calculated value (Table II). The main reason is that the analytical calculation (emLook) in generator mode does not correctly take into account the real reduction of reactance leakage for the basic harmonic of the magnetic field. This is due the higher current in the rotor, which has as a consequence higher local saturation in slot bridges. The motor thus has the measured current in the breakdown point  $I_b \approx 36$  A, and the generator  $I_b \approx 96$  A; the increase is about threefold. The reactance leakage is the same in the analytical calculation for motor and for generator both in the nominal and the breakdown operation points. This is the main reason for the difference between the measured and the calculated results. Another increase of the breakdown torque in generator operation mode is the consequence of the influence of higher harmonics, which are being deduced in generator operation, i.e. added to the negative torque of the basic harmonic for the generator, thus absolutely increasing it.

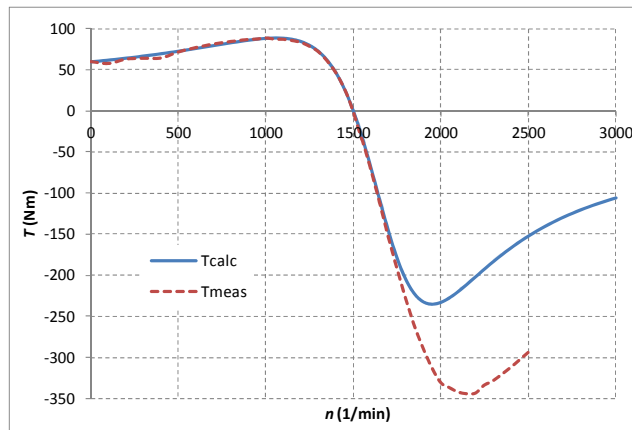


Figure 8. Measured and calculated torque characteristics

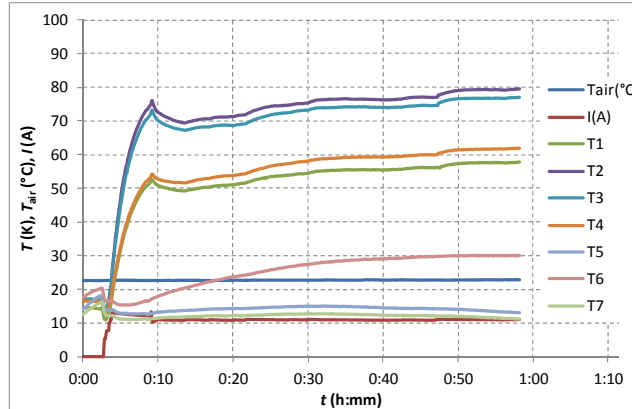


Figure 9. Results of temperature rise test in motor operation mode: nominal power 5.5 kW (mechanical output power)

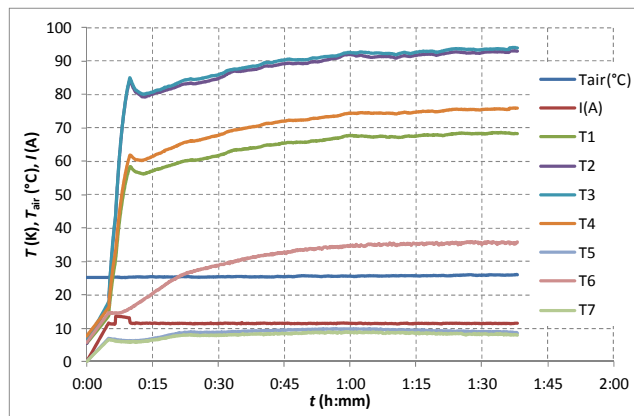


Figure 10. Results of temperature rise test in generator operation mode: thermal power 6.6 kW (electrical output power)

Because of a much higher torque characteristic in generator operation mode the losses of the machine are lower with the same output power. With the same load current and the same cooling conditions the output power in generator operation mode is for the presented machine 6.36 kW or by 15.6% higher than in the motor operation mode with 5.5 kW of power. The thermal power was approximately 6.6 kW at the incoming water temperature 50 °C and flow of 8.3 l/min for F insulation class. Results of temperature rise tests for motor and generator operating mode are presented in Figure 9 and 10.

## 5. Conclusion

The paper presents an analytical equation for calculation of induction machine breakdown torque in motor and generator operating regimes. Special emphasis is given to the comparison of machine characteristics in motor and generator modes, including a comparison of calculated and measured results for load conditions and torque characteristics. The differences between the calculated and the measured results are commented on and explained in detail. From calculated and measured results it is obviously seen that the induction machine is able to operate in generator mode with higher power than in motor operating mode. Reason lies in higher efficiency and lower power losses of generator which is reflected as lower heating in comparison with motor.

The main focus of future research will be calculation of torque characteristics and magnet circuit and equivalent circuit parameters of an induction machine with finite element method in order to improve the analytical approach.

## References

- [1] Prus, V. V., Zagirnyak, M. V., Kolotylo, I. A., Miljavec, D.: *Estimate and taking into account change of steel losses in induction motors in process of their aging*, Proceedings of International IEEE Conference EUROCON 2009, Saint Petersburg, (2009), pp. 790–795.

- [2] Prus, V., Nikitina, A., Zagirnyak, M., Miljavec, D.: *Research of energy processes in circuits containing iron in saturation condition*, Przeglad Elektrotechniczny, Vol. 87, Issue 3, (2011), pp. 149–152.
- [3] Vrtič, P.: *Variations of Permanent Magnets Dimensions in Axial Flux Permanent Magnet Synchronous Machine*, Przeglad Elektrotechniczny, Vol. 87, Issue 12b, (2011), pp. 194–197.
- [4] Vrtič, P., Avsec, J.: *Analysis of coreless stator axial flux permanent magnet synchronous generator characteristics by using equivalent circuit*, Przeglad Elektrotechniczny, Vol. 87, Issue 3, (2011), pp. 208–211.
- [5] Kent, R. D.: *Analytic Analysis of Single- and Three-Phase Induction Motors*, IEEE Transactions on Magnetics, Vol. 34, No. 5, (1998), pp. 3721–3727.
- [6] Mlakar, M., Hadžiselimović, M., Štumberger, B., Zagradišnik, I.: *Determination of equivalent circuit parameters for three-phase induction motors: procedure in accordance with the iec 60034-28 standard*, Journal of Energy Technology, Vol. 4, Issue 2, (2011), pp. 31–46.
- [7] Zagirnyak, M., Mamchur, D., Kalinov, A.: *The theory and application of the induction motor diagnostic methods based on electrical signal analysis*, Journal of Energy Technology, Vol. 5, Issue 2, (2012), pp. 37–50.
- [8] Zagradišnik, I., Hadžiselimović, M., Ritonja, J., Slemnik, B.: *The emLook software package for the analytical and numerical analyses of electrical machines*, Prz. Elektrotech., Vol. 85, Issue 12, (2010), pp. 175–178.

# The Asymmetry of the Magnetic Field Distribution in a Flat Unshielded 3-phase High Current Busduct

D. Kusiak<sup>1</sup>, Z. Piątek<sup>2</sup>, T. Szczegielniak<sup>2</sup>

Czestochowa University of Technology, Faculty of Electrical Engineering<sup>1</sup>

Aleja Armii Krajowej 17, 42-200 Częstochowa,

Czestochowa University of Technology,

Faculty of Environmental Engineering and Protection<sup>2</sup>

ul. Brzeźnicka 60a, 42-200 Częstochowa,

e-mail: [dariuszkusiak@wp.pl](mailto:dariuszkusiak@wp.pl) [zygmunt.piatek@interia.pl](mailto:zygmunt.piatek@interia.pl),  
[szczegielniakt@interia.pl](mailto:szczegielniakt@interia.pl)

**Abstract.** It has been demonstrated in the paper that the magnetic field distribution in two outer conductors of the flat, three-phase, high-current busduct is asymmetric. The components of this field reflect the magnetic field of the reverse reaction fields of the eddy currents induced in the conductors of the adjacent phases as the results of the proximity effect and the skin effect. The field distribution is shown in the outer area of the outer phases as the function of the parameters reflecting the current frequency, the conductivity, and the transverse dimensions of the tubular conductors. The results also account for the fact that analogously in the high-current busducts of this type the active power losses, temperature distributions, and electrodynamic forces, will not be the same in the outer buses.

*Key words:* magnetic field, tubular conductor, high current busduct

## 1. Introduction

The magnetic field in the external area of the flat unshielded three-phase high current busduct (fig. 1) is a vector sum of the own magnetic field, and that generated by the currents in the adjacent tubular conductors, with the consideration of the magnetic field of the reverse reaction. Instead, in the conductors we have the sum of the own magnetic field with the consideration of the skin effect as well as the field induced by the magnetic field of the adjacent phase currents. The own current, in accordance with the Ampere's law, does not generate any magnetic field inside a tubular conductor, and the magnetic field in this area generated by the currents in the adjacent conductors can be neglected [1,2].

In this study it has been shown that the magnetic field distribution in the two external conductors of a three-phase flat unshielded high-current busduct is not the same, in spite of the symmetry of the system geometry [3].

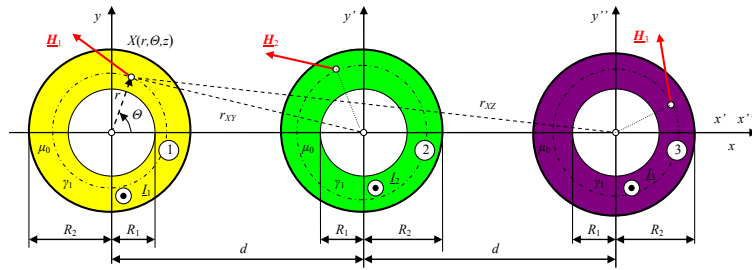


Figure 1. Three phase high current busduct with the currents  $I_1$ ,  $I_2$  and  $I_3$

## 2. Magnetic field distribution

In the unshielded flat three-phase high current busduct, as shown in figure 1 we assume a symmetrical threesome of phase currents, i.e. [4, 5]

$$I_2 = \exp[-j\frac{2}{3}\pi]I_1 \quad \text{and} \quad I_3 = \exp[j\frac{2}{3}\pi]I_1 \quad (1)$$

The magnetic fields of external origin are for the outer phases, and those generated only by the currents in the adjacent phases can be presented as

$$\underline{H}_{123}^w(r, \theta) = \underline{H}_{12}^w(r, \theta) + \underline{H}_{13}^w(r, \theta) \quad (2)$$

and accordingly

$$\underline{H}_{312}^w(r, \theta) = \underline{H}_{31}^w(r, \theta) + \underline{H}_{32}^w(r, \theta) \quad (3)$$

The modules of these fields are respectively symmetrical – fig 2.

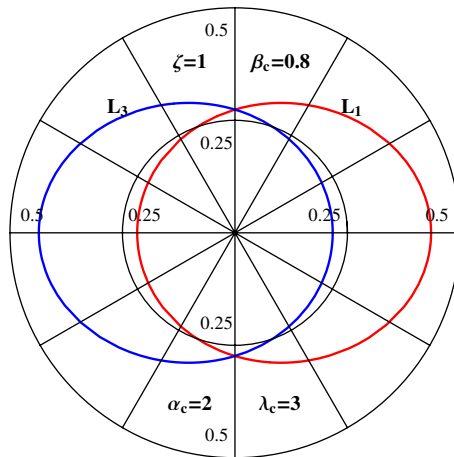


Figure 2. The distribution of the modules of the magnetic field of external origin (without the magnetic field of the own phase) in the outer phases of the three-phase, flat, high-current busduct with the symmetrical currents  $I_1$ ,  $I_2$  and  $I_3$  ( $lc=d/R_2$  ( $lc \geq 1$ ),  $x=r/R_2$ ,  $bc=R_1/R_2$  ( $0 \leq bc < 1$ ))

These fields induce the eddy currents which in turn generate reverse reaction magnetic fields  $\underline{H}_{123}^{rr}(r, \vartheta)$  and  $\underline{H}_{321}^{rr}(r, \vartheta)$ . These fields are still respectively symmetrical in the outer phases due to the identical mechanism of generating them in relation to the respective fields  $\underline{H}_{123}^w(r, \vartheta)$  and  $\underline{H}_{321}^w(r, \vartheta)$  – fig 3.

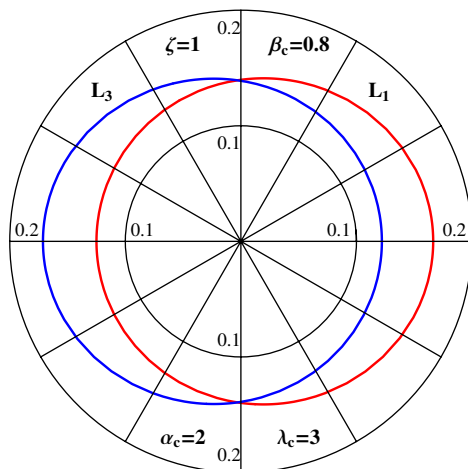


Figure 3. The distribution of the modules of the reverse reaction magnetic field in the outer phases of the three-phase, flat, high-current busduct with the symmetrical currents I1, I2 and I3

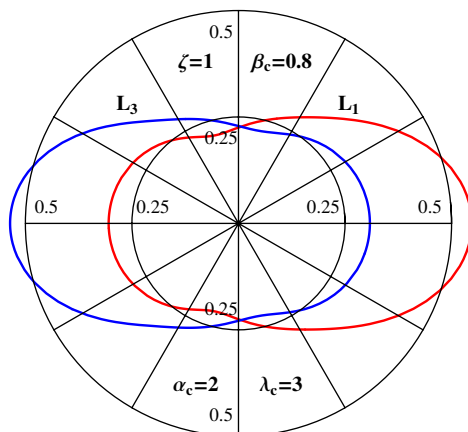


Figure 4. The distribution of the modules of the magnetic field outside of the outer phases (without the magnetic field of the own phase) of the flat, high-current busduct with the symmetrical currents I1, I2 and I3

The magnetic fields outside of the conductors, without the own fields can be presented as:



$$\underline{H}_{123}^{ext}(r, \Theta) = \underline{H}_{123}^w(r, \Theta) + \underline{H}_{123}^{rr}(r, \Theta) \quad (4)$$

and

$$\underline{H}_{321}^{ext}(r, \Theta) = \underline{H}_{321}^w(r, \Theta) + \underline{H}_{321}^{rr}(r, \Theta) \quad (5)$$

These fields remain still respectively symmetrical one to another – fig 4.

### 3. Asymmetry of the magnetic field

The total magnetic field outside of the conductors of the outer phases can be express with the following formulas [6]

$$\underline{H}_1^{ext}(r, \Theta) = \underline{H}_{11}^{ext}(r) + \underline{H}_{12}^{ext}(r, \Theta) + \underline{H}_{13}^{ext}(r, \Theta) = \underline{H}_{11}^{ext}(r) + \underline{H}_{123}^{ext}(r, \Theta) \quad (6)$$

and

$$\underline{H}_3^{ext}(r, \Theta) = \underline{H}_{33}^{ext}(r) + \underline{H}_{31}^{ext}(r, \Theta) + \underline{H}_{32}^{ext}(r, \Theta) = \underline{H}_{33}^{ext}(r) + \underline{H}_{321}^{ext}(r, \Theta) \quad (7)$$

The  $\underline{H}_{11}^{ext}(r)$  and  $\underline{H}_{33}^{ext}(r)$  fields have tangent components only. Therefore, the above vector summing up can be limited to the summing up of the relevant tangent components. That summing up is an operation in the complex number domain, hence the complex sums of tangent components [7, 8]

$$\underline{H}_{1\Theta}^{ext}(r, \Theta) = \underline{H}_{11\Theta}^{ext}(r) + \underline{H}_{12\Theta}^{ext}(r, \Theta) + \underline{H}_{13\Theta}^{ext}(r, \Theta) = \underline{H}_{11\Theta}^{ext}(r) + \underline{H}_{123\Theta}^{ext}(r, \Theta) \quad (8)$$

and

$$\underline{H}_{3\Theta}^{ext}(r, \Theta) = \underline{H}_{33\Theta}^{ext}(r) + \underline{H}_{31\Theta}^{ext}(r, \Theta) + \underline{H}_{32\Theta}^{ext}(r, \Theta) = \underline{H}_{33\Theta}^{ext}(r) + \underline{H}_{321\Theta}^{ext}(r, \Theta) \quad (9)$$

are determined not only by the modulus values of the sum components, but also their amplitudes, and more precisely the difference of the amplitudes. The distribution of these differences for the outer phases is shown in figure 5.

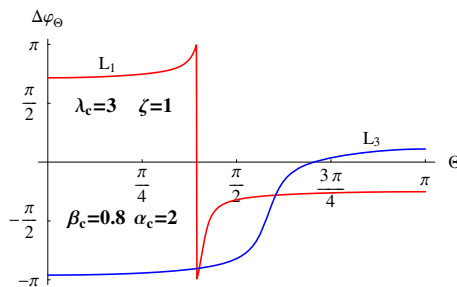


Figure 5. The distribution of the differences of the amplitudes of the field tangent component of the own phase and the tangent component of the field outside (without the magnetic field of the own phase) of the outer phases of a 3-phase flat high-current busduct with symmetrical currents I1, I2 and I3

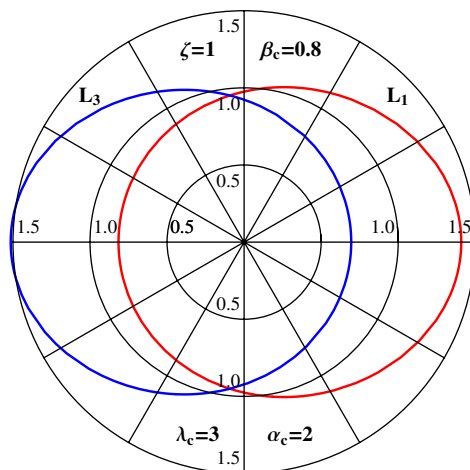


Figure 6. The distribution of the modulus values of the total magnetic field outside of the conductors of the outer phases of a 3-phase flat high-current busduct with symmetrical currents  $I_1, I_2$  and  $I_3$

As it can be seen in figure 5, despite the fact the modulus values of the own fields of individual phases and the modulus values outside of the outer phases are the same the relevant sums of the tangents components in the complex number domain will not have the same modulus values. Therefore, the total magnetic field with the consideration of the magnetic field of the own phase outside of the outer phases is not accordingly symmetrical – figure 6.

The problem of the asymmetry of the magnetic field distribution outside of the conductors of the outer phases of the three-phase, flat, high-current busduct can be also explained with indicator diagrams. Let us assume a symmetrical threesome of the magnetic field of the own phase currents – figure 7.

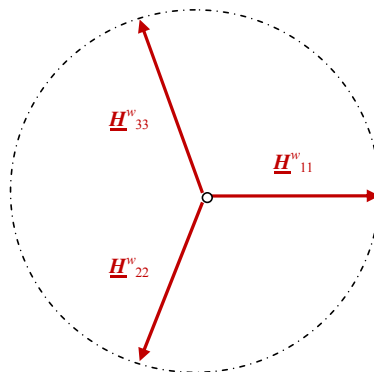


Figure 7. The own magnetic field outside of the conductors of the three-phase, flat, high-current busduct with the symmetrical currents  $I_1, I_2$  and  $I_3$

In some points on the surfaces of the conductors of the outer phases, said points being symmetrical with respect to the centre of the middle phase axis we can assume that the feedback magnetic fields of eddy currents add up vectorially and in the domain of complex numbers with the relevant fields which have induced these currents – for the L1 phase in the  $\Theta = p$  point (fig. 9) and the corresponding to it  $\Theta = 0$  point (symmetrical with respect to the middle phase axis) for the L3 phase (fig. 8).

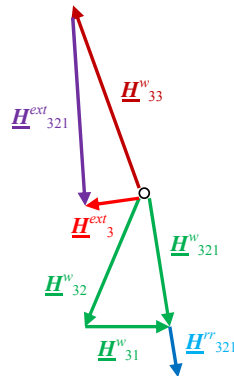


Figure 8. The indicator diagram of the magnetic fields for the outer phase L3 of the three-phase flat high-current busduct with the symmetrical currents I1, I2 and I3

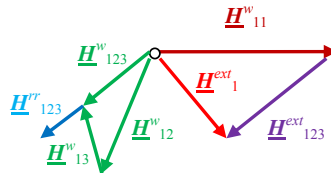


Figure 9. The indicator diagram of the magnetic fields for the outer phase L1 of the three-phase flat high-current busduct with the symmetrical currents I1, I2 and I3

#### 4. Conclusions

The total magnetic field outside of the extreme phases 3-phase flat high current busduct is not accordingly symmetrical – fig. 6. This asymmetry increases with the increase of the current frequency, the electrical conductivity, and the outer radius of the conductors

The indicator diagrams presented above show (figure 8 and 9) that in certain point ( $r = R_2, \Theta = \Theta_2$ ) on the surface of the outer L1 phase the module of the total magnetic field outside of the conductor differs from the module of the total magnetic field in the symmetrical point on the external surface of the conductor of the L3 phase. In the provided example  $|\underline{H}_1^{ext}(r = R_2, \Theta = \Theta_0)| > |\underline{H}_3^{ext}(r = R_2, \Theta = \Theta_0)|$ . In other points a reverse inequality or an equality may happen.

## Acknowledgments

This work is financed by the Polish National Science Centre as research project N N511 312540.

## References

- [1] Kusiak, D.: *Description of elliptical magnetic field in unshielded bifilar transmission line*, Electrical Engineering, No. 62, (2010), pp. 67–76.
- [2] Kusiak, D.: *Use elliptical magnetic fields in unscreened flat three phase busduct*, XXXIII IC SPETO, Gliwice-Ustroń, (2010).
- [3] Cao, M., Biringer, P. P.: *Asymmetry in bus bars due to proximity effects*, Journal of Applied Physics, Volume 67, Issue 9, (1990), pp. 4729–4731.
- [4] Piątek, Z., Kusiak, D., Szczegielniak, T.: *Elliptical magnetic field in the high current busducts* (in Polish), Przegląd Elektrotechniczny, R. 86 NR 4, (2010), pp. 101–106
- [5] Piątek, Z.: *Modeling of lines, cables and high-current busducts* (in Polish), Seria Monografie nr 130, Wyd. Pol. Częst., Częstochowa, (2007).
- [6] Piątek, Z., Kusiak, D., Szczegielniak, T.: *Magnetic field of the three phase flat high current busduct* (in Polish), Zesz. Nauk. Pol. Śl., Elektryka, z.1(209), (2009), pp. 51–65.
- [7] Kusiak, D.: *Magnetic field of two- and three-pole high current busducts* (in Polish), Dissertation doctor, Pol. Częst., Wydz. Elektryczny, Częstochowa, (2008).
- [8] Piątek, Z.: *Impedances of Tubular High Current Busducts*, Series Progress in High-Voltage technique, Vol. 28, Polish Academy of Sciences, Committee of Electrical Engineering, Wyd. Pol. Częst., Czestochowa, (2008).

# Using Electrical Impedance Tomography in Flood Embankment System

Krzysztof Król<sup>1</sup>, Jan Sikora<sup>1,2</sup>, Tomasz Rymarczyk<sup>3</sup>

Lublin University of Technology, Department of Electronics

Nadbystrzycka 38d, 20-618 Lublin<sup>1</sup>,

Electrotechnical Institute, Warsaw<sup>2</sup>,

Net-art, Lublin Lotnicza 3, 20-322 Lublin<sup>3</sup>,

e-mail: tomasz@rymarczyk.com

**Abstract:** A new nondestructive method of the flood embankment dampness was tested by the electrical impedance tomography. The basic information about the built measuring system, including prototype equipment is given. The setup was used to determine the dampness of the test flood blank on a specially built model. The boundary element method was used to solve the forward problem. The neural networks were applied in the inverse problem for the image reconstruction.

**Keywords:** *Electrical Impedance Tomography, Boundary Element Method, Neural Networks*

## 1. Introduction

This paper presents the system for identification the unknown shape of an interface. A new nondestructive method of the flood embankment dampness was tested by the electrical impedance tomography [4, 5]. It makes it possible to obtain a 3D distribution of wall dampness. Basic information about the built measuring system, including prototype equipment is given. The setup was used to determine the dampness of the test flood blank on a specially built model. The boundary element method was used to solve the forward problem [1, 2, 3]. Decreasing along wall height and depth humidity creates nonhomogenous testing environment where object properties conductivity varied smoothly with one more coordinates. The distribution of potentials on the surface of an object depends on the distribution of conductivity. Surface potential measurements are performed at different angles of projection whereby the information needed to determine an approximate distribution of conductivity inside the object is obtained. The architecture of the flood embankment system was shown in the figure 1.

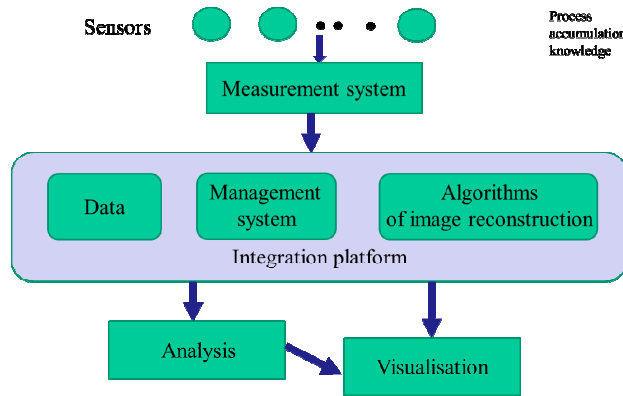


Figure 1. The architecture of the flood embankment system

**2. Electrical impedance tomography**

Electrical impedance tomography is a widely investigated problem with many applications in physical and biological sciences. The presenting method was based a numerical scheme for the identification of piecewise constant conductivity coefficient for a problem arising from electrical impedance tomography. Forward problem solution in EIT consist in determining potential distribution inside the region under given boundary conditions and full information about region under consideration; that is in solving Laplace’s equation. The inverse problem is nonlinear and highly ill-posed. Several of numerical techniques with different advantages have been proposed to solve the problem. The following functional is minimized (the difference between the potential due to the applied current and the measured potential):

$$F = 0.5 \sum_{j=1}^p (U - U_0)^T (U - U_0) \tag{1}$$

where  $p$  is the number of the projection angles.

**3. Forward problem**

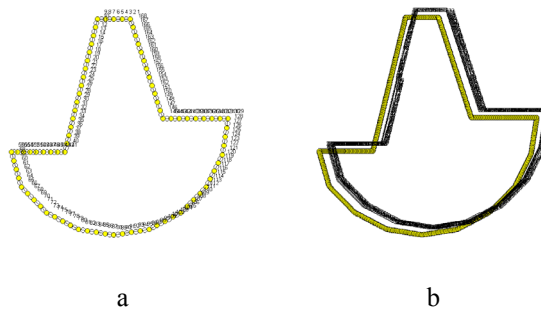


Figure 2. The cross-section of the flood embankment for: (a) 84 elements, (b) 336 elements

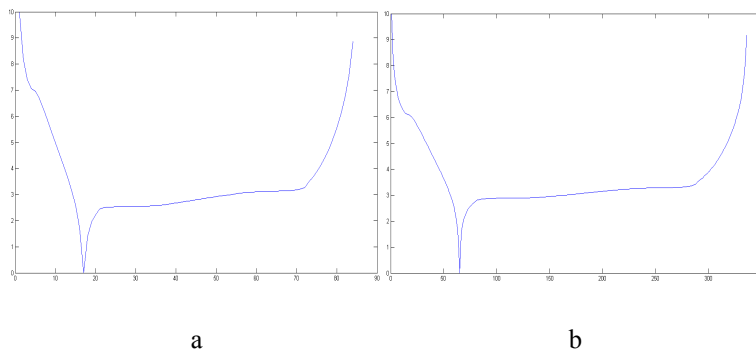


Figure 3. The value of the potentials on the edge of the flood embankment for:  
 (a) 84 elements, (b) 336 elements

The figure 2 shows the tested object of the flood embankment with the finite and infinite elements. The value of the potentials on the edge of the flood embankment for 84 and 336 elements were presented on the figure 3.

In the figure 4 the object was divided into 57 elements, 111 nodes. Each element consists of three nodes. The red element symbolizes the electrode 10 V. In black marked 0 V ground potential. For the area of  $\gamma_4$  is water. The measurement voltage is from node 1 to 57–28 items (27 electrodes from node 2 at the second node to node until the number 56, in addition to node 32 where it was applied 10 V). Green color indicated the first item.

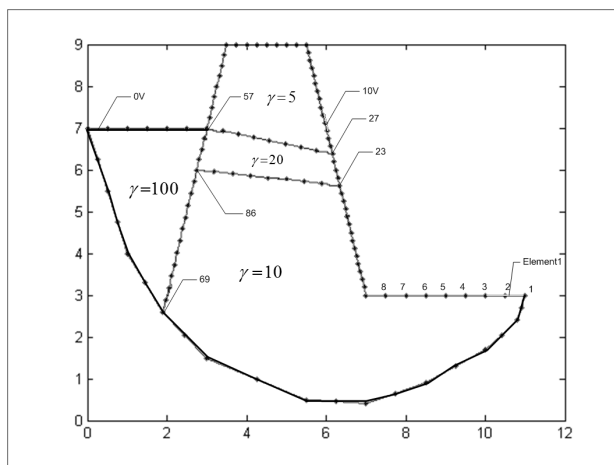


Figure 4. The distribution of elements on the edge of the flood embankment

Description of legends of all graphs such as 1020580

- Gamma1 = 10
- Gamma2 = 20 saturated sand
- Gamma3 = 5 dry sand
- Gamma4 = 80 water

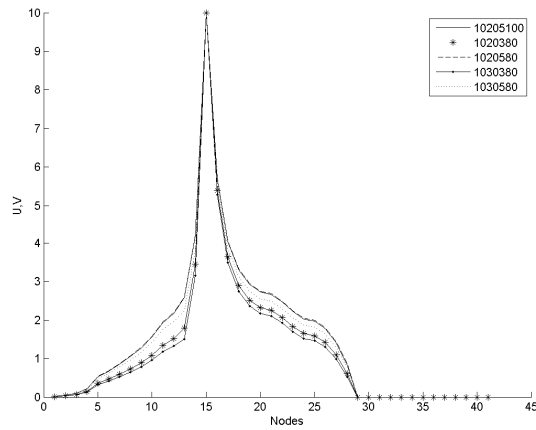


Figure 5. Potentials on the edge of the bank

The distribution of potentials on the edge of the flood embankment results can easily check the state of saturation in the layer of sand  $\gamma_2$ . The greater permeability of the sand is lower potential at the edge of the flood embankment. The lower permeability area  $\gamma_3$  is lower potentials. As you can see from the chart the impact of water conductivity in a very small influence on the distribution of potentials in most places (at the edge of the flood embankment and on the border between the saturated sand and the top layer of dry sand and the boundary between the saturated sand and a lower layer of the bank). Only the results differ on the border of the bank – the water. The distribution of potentials on the border of saturated sand and the top of the bank is linear, it may be because the electrode was placed near the 10V and the other side of the border of three centers is 0 V.

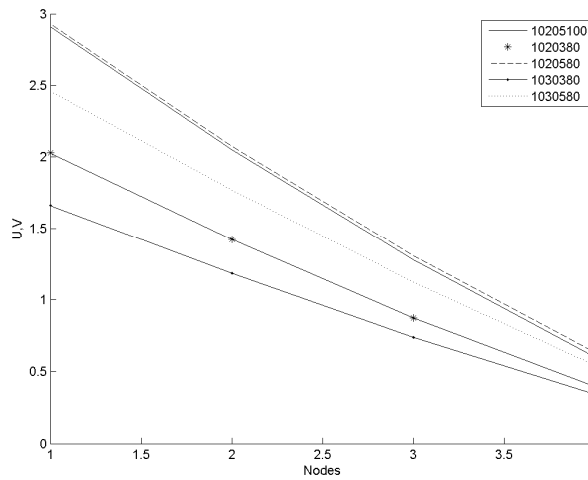


Figure 6. Potentials of the upper limit of the saturated sand



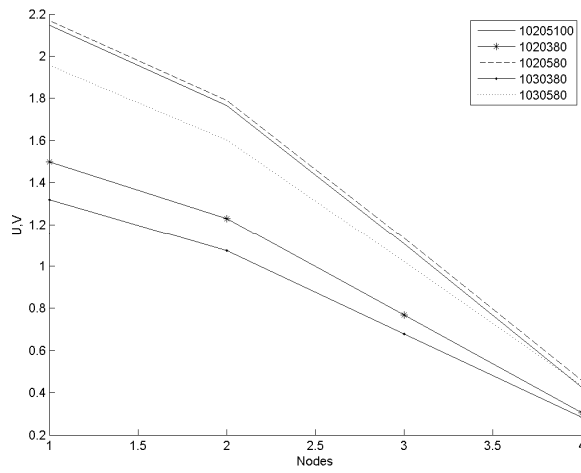


Figure 7. The potentials lower limit of the saturated sand

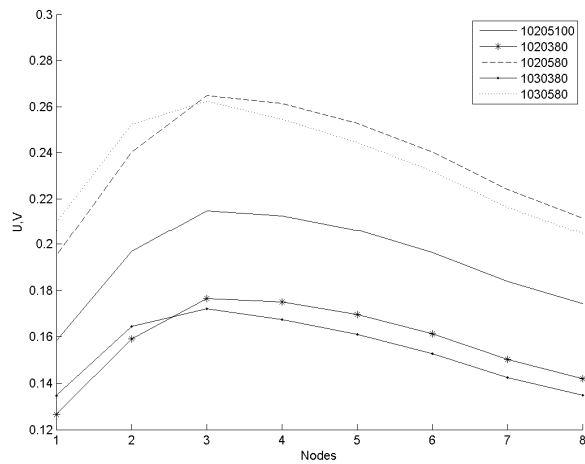


Figure 8. Potentials on the border of the bank water

As shown in Figures 5, 6, 7 and 8 that the greatest impact on the potentials are on the layer of the saturated sand ( $\gamma_3$ ) and only the second layer of the saturated sand. The lower the conductivity of the lower layer  $\gamma_3$  potential values were obtained at the border centers. By contrast, the smaller the value of the conductivity of the layer  $\gamma_2$  are larger values of potentials at the border areas. Only at the border of the bank water can be observed that there is the saturated sand ( $\gamma_2$ ) All results are discussed with the opposite of figures 5, 6, 7, 8. Only at the edge between water and  $\gamma_1$  layer dependencies are the same as discussed with the drawings 5,6,7,8.

All results were obtained using BEM with the library BEMLAB [6].

**4. Neural Networks**

For different values of gamma2 changed from 5 to 20 in steps of 1 were made measurements. On elements from 14 to 20 (from node 27 to the upper edge of the horizontal) was potential 10V and the potential 0V in the same area marked in black in figure 9. The other components were unchanged.

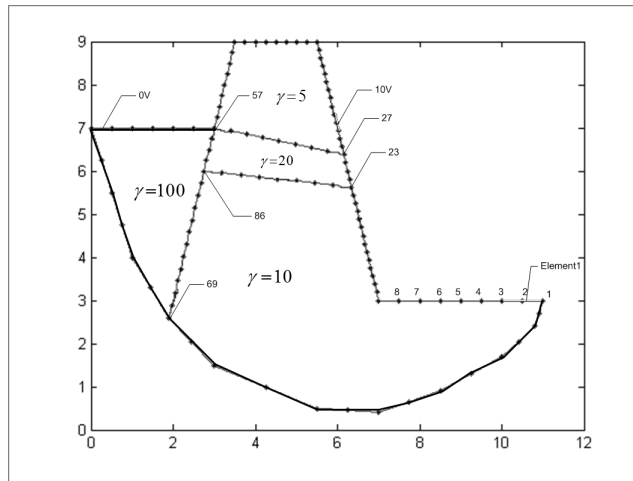


Figure 9. The flood embankment

It was built neural network, which consists of three layers: input, hidden and output. There were given to the input data generated from the design model flood embankment. The input data are introduced as vectors consisting of 73 elements. The hidden layer neurons were 9 and the output first. All the neurons are linear. Figure 10 is presented the neural network learning process. Figure 11 and 12 on the vertical axis represented the value of the permeability on the horizontal axis.

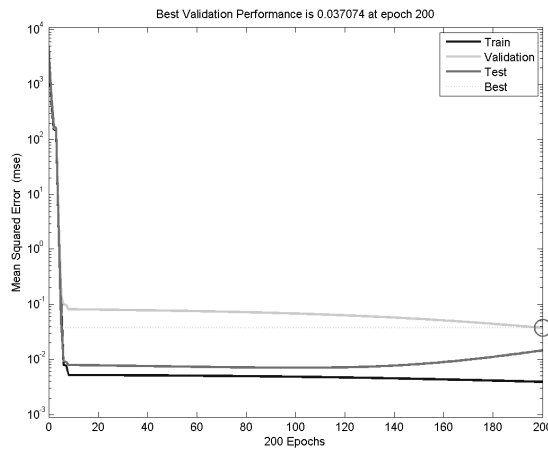


Figure 10. The learning process of the neural network

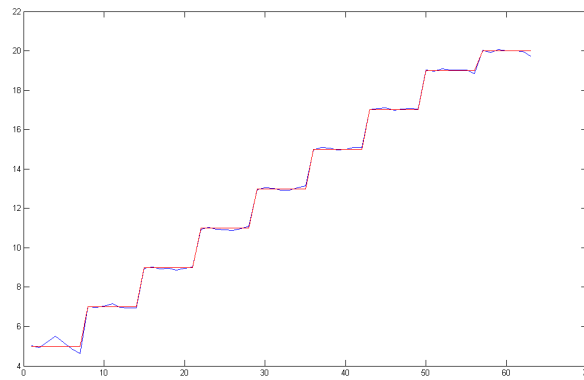


Figure 11. The neural networks response for training data (blue), the red color should look like the answer

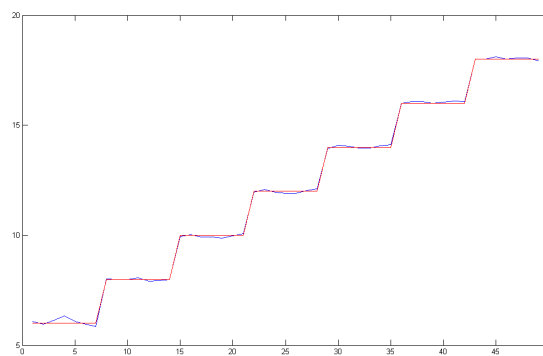


Figure 12. Response of the neural network for test data (blue), the red color should look like the answer

## 5. Summary

This paper has introduced the new method examining the flood embankment dampness by the electrical impedance tomography. The applications was depended on a specially built model. The boundary element method was used to solve forward problem. The inverse problem was solved by the neural network. For the electrical impedance tomography, it is sometimes more important to recover the shape of the domains containing different materials than to recover the values for the materials. It is sometimes more important to recover the shape of the domains containing different materials than to recover the values for the materials. The presented techniques were shown to be successful to identify the unknown properties of the object.

**References**

- [1] Beer, G.: *Programming the boundary element method*, John Wiley & Sons, Ltd (2001).
- [2] Filipowicz, S. F., Rymarczyk, T.: *Tomografia Impedancyjna, pomiary, konstrukcje i metody tworzenia obrazu*, BelStudio, Warsaw, (2003).
- [3] Sikora, J.: *Boundary Element Method for Impedance and Optical Tomography*, OWPW (2007).
- [4] Rymarczyk, T., Filipowicz, S. F., Sikora, J., Polakowski, K.: *Applying the level set methods and the immersed interface method in EIT*, Electrical Review, R. 85 NR 4, (2009), pp. 68–70.
- [5] Rymarczyk, T., Filipowicz, S. F., Sikora, J., Polakowski, K.: *A piecewise-constant minimal partition problem in the image reconstruction*, Electrical Review, R. 85 NR 12, (2009), pp. 141–143.
- [6] BEMLAB: <http://bemlab.org>.

# Transient Analysis of Induction Motor Using Different Simulation Models

V. Sarac<sup>1</sup>, G. Cvetkovski<sup>2</sup>

Goce Delcev University, Electrotechnical Faculty,  
P. O. Box 201, 2000 Stip, Macedonia<sup>(1)</sup>,  
Cyril and Methodius University, Faculty of Electrical Engineering and IT,  
P. O. Box 574, 1000 Skopje, Macedonia<sup>(2)</sup>  
e-mail: vasilija.sarac@ugd.edu.mk , gogacvet@feit.ukim.edu.mk .

**Abstract.** Squirrel cage induction motors have wide range of applications in many industrial drive systems due to their simple construction, robust design and low operational costs. Their application becomes even wider as a result of implementation of voltage inverters providing very good speed-torque control characteristics. In this paper a dynamic behaviour of a squirrel cage induction motor type 2AZ 155-4 is analysed. Two simulation models are developed, the first one in Matlab/Simulink and the second one in PSIM enabling motor transient characteristics to be analysed. Information about the distribution of the magnetic flux density inside the motor cross section is gained by application of the Finite Elements Method (FEM).

**Keywords:** *induction squirrel cage motor, MATLAB/Simulink and PSIM simulation models, FEM motor model*

## 1. Introduction

Squirrel cage induction motor has wide application in many industrial drive systems due to its simple construction, robust design and low operational costs. Its application becomes even wider as a result of voltage inverters enabling very good speed-torque regulation characteristics. In this paper the dynamic performance of squirrel cage induction motor type 2AZ 155-4 produced by Rade Koncar is analyzed. The motor has the following rated data: voltage  $U_n (\Delta/Y) = 220/380$  V, number of poles  $2p = 4$ , rated current  $8.7/5$  A, power factor  $\cos\phi = 0.81$ , rated speed  $n_n = 1410$  rpm, frequency 50 Hz. The first simulation motor model is developed in MATLAB/Simulink [1], for situation when the motor is connected to symmetrical power supply. For that purpose a motor mathematical model is developed based on the motor d, q transformation into synchronously rotating system. From the simulation motor transient characteristics of speed, electromagnetic torque and currents are obtained. The analysis is extended with simulation model when the motor is fed by a voltage inverter. In this case the motor transient speed, current and electromagnetic torque characteristics are obtained, for rated frequency as well as for frequencies lower and higher than the rated one. The results obtained from the simulation in Simulink are verified with the results obtained from the second simulation model developed in the software program PSIM. The

distribution of the magnetic field in the motor cross section is obtained by using the Finite Element Method (FEM) for all the motor operation regimes.

## 2. Simulation models

Simulation of the motor transient characteristics in SIMULINK is performed by building a simulation model based on  $d,q$  transformation. In Fig. 1 a block diagram of the simulation model consisted of following four main parts is presented:

- Power supply
- Transformation of  $a, b, c$  variables into variables in  $d,q$  system that rotates synchronously.
- Modelling of motor model and obtaining motor speed, currents and electromagnetic torque as output variables.
- Transformation from  $d,q$  system into  $a, b, c$  system in order stator and rotor voltages and currents to be obtained.

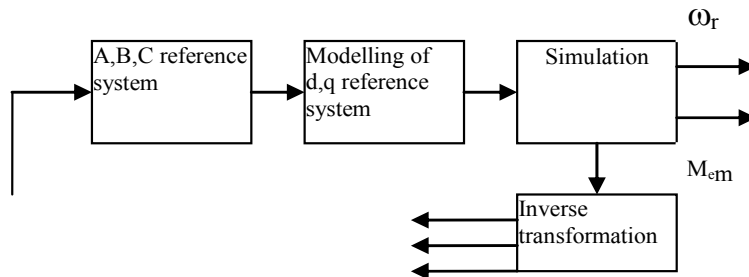


Figure 1. Block chart of Simulink motor model

Firstly the motor power supply (three phase symmetrical power supply) is transformed from three phase system into  $d,q$  system which rotates with synchronous speed as it is presented with equations (1) and (2).

$$U_{ds} = -\frac{1}{\sqrt{3}}(U_b - U_c)\cos\theta + U_a \sin\theta \tag{1}$$

$$U_{qs} = \frac{1}{\sqrt{3}}(U_b - U_c)\sin\theta + U_a \cos\theta \tag{2}$$

where:  $\omega = \frac{d\theta}{dt}$  i.e.  $\theta = \int_0^t \omega dt$

Since the power supply is a three phase symmetrical supply in that case  $\omega = \omega_e = 314 \text{ (rad/s)}$ . The simulation model is based on the following equations:

$$\begin{aligned}
i_{qr} &= \frac{L_s R_r}{L_m^2 - L_s L_r} \int_0^t i_{qr} dt + \frac{\omega L_s L_r}{L_m^2 - L_s L_r} \int_0^t i_{dr} dt + \\
&\frac{L_{sr} \omega}{L_m^2 - L_s L_r} \int_0^t \psi_{ds} dt + \frac{L_{sr}^2 - L_s L_r}{L_m^2 - L_s L_r} \int_0^t \omega_r i_{dr} dt - \\
&\frac{L_{sr}}{L_m^2 - L_s L_r} \int_0^t \omega_r \psi_{ds} dt + \frac{L_{sr}}{L_m^2 - L_s L_r} \psi_{qs}
\end{aligned} \quad (3)$$

where  $i_{qr}$  and  $i_{dr}$  are rotor currents transformed  $d,q$  systems and  $L_s$ ,  $L_r$  and  $L_{sr}$  are stator, rotor and mutual inductance respectively.

$$\begin{aligned}
i_{dr} &= \frac{L_s R_r}{L_m^2 - L_s L_r} \int_0^t i_{qr} dt - \frac{\omega(L_{sr}^2 - L_s L_r)}{L_m^2 - L_s L_r} \int_0^t i_{dr} dt - \\
&- \frac{L_{sr} \omega}{L_m^2 - L_s L_r} \int_0^t \psi_{qs} dt - \frac{(L_{sr}^2 - L_s L_r)}{L_m^2 - L_s L_r} \int_0^t \omega_r i_{qr} dt \\
&+ \frac{L_{sr}}{L_m^2 - L_s L_r} \int_0^t \omega_r \psi_{qs} dt + \frac{L_{sr}}{L_m^2 - L_s L_r} \psi_{ds}
\end{aligned} \quad (4)$$

In the equations (3) and (4) flux linkages  $\psi_{qs}$  and  $\psi_{ds}$  are unknown variables and they can be expressed from:

$$\psi_{qs} = \int_0^t U_{qs} dt - \frac{R_s}{L_s} \int_0^t \psi_{qs} dt + \frac{L_{sr} R_s}{L_s} \int_0^t i_{qr} dt - \omega \int_0^t \psi_{ds} dt \quad (5)$$

$$\psi_{ds} = \int_0^t U_{ds} dt - \frac{R_s}{L_s} \int_0^t \psi_{ds} dt + \frac{L_{sr} R_s}{L_s} \int_0^t i_{dr} dt + \omega \int_0^t \psi_{qs} dt \quad (6)$$

Motor speed is calculated from:

$$\frac{d\omega_r}{dt} = \frac{6L_{sr}}{J} (i_{qs} i_{dr} - i_{ds} i_{qr}) - \frac{2}{J} M_s - \frac{2}{J} M_0 \quad (7)$$

where  $M_s$  is load torque,  $M_0$  is a torque as a result of acceleration at no-load.

The second simulation model is built in PSIM software for symmetrical sinusoidal power supply as well as for the case when the motor is fed by a voltage inverter with variable frequency (Fig. 2).

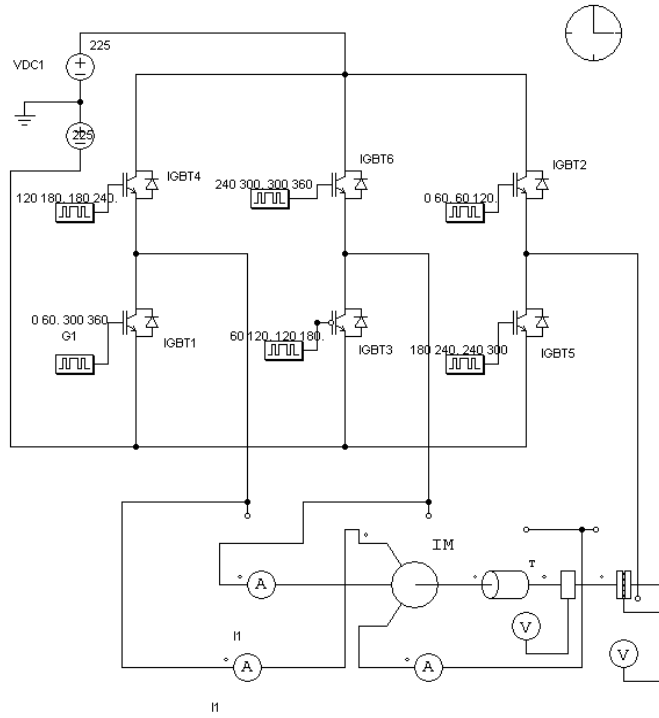
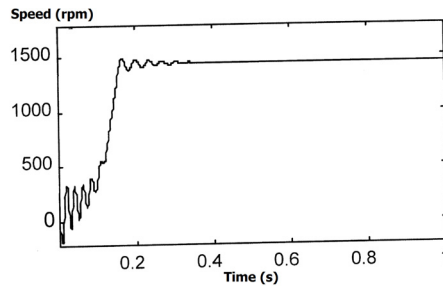


Figure 2. Simulation model in PSIM

### 3. Simulation results

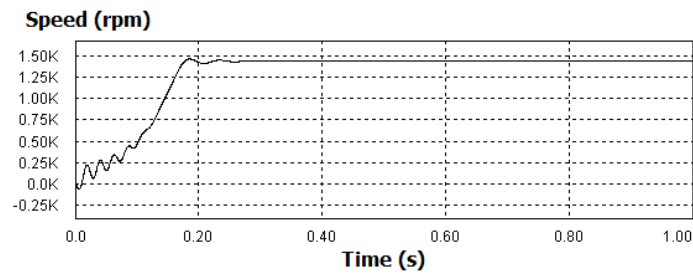
#### 3.1. A. Simulation results at symmetrical power supply 50 Hz

First, the motor simulation models are developed for power supply from network. As an output from SIMULINK and PSIM models, motor transient characteristics can be obtained for different operating regimes: no-load as well as for rated load. In Fig. 3 transient speed characteristics for rated load condition meaning constant load of  $M_s = 14$  Nm, using both simulation models, are presented.



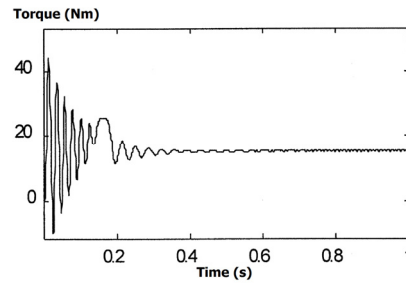
(a) Simulink model



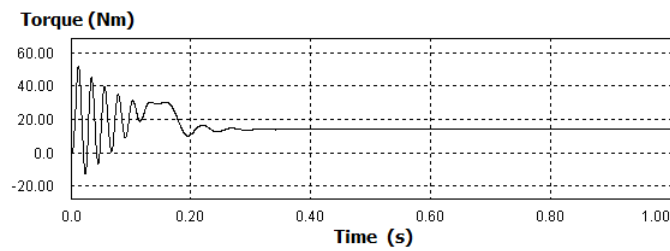


(b) PSIM model

Figure 3. Motor speed at power supply from network,  $f=50$  HZ

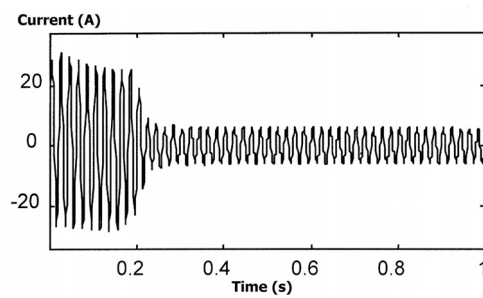


(a) Simulink model

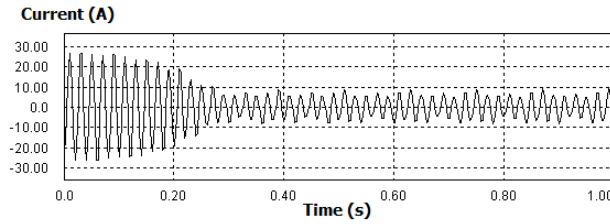


(b) PSIM model

Figure 4. Torque for power supply from network,  $f = 50$  Hz



(a) Simulink model



(b) PSIM model

Figure 5. Stator current for power supply from network,  $f=50$  HZ

From Fig. 3 it can be concluded that the motor is reaching the speed of 1440 rpm after acceleration time of 0.2 seconds. After the acceleration time has expired electromagnetic torque is achieving steady-state value of approximately 15 Nm. For the same period the value of the current is dropping from the value of starting current which is five times rated current to the maximum value of 6 A. Comparison of obtained results from Simulink model and PSIM model for the transient characteristics of speed, electromagnetic torque and stator current shows satisfactory agreement among them, which consequently proves the accuracy of both simulation models.

### 3.2. B. Simulation results using inverter as power supply

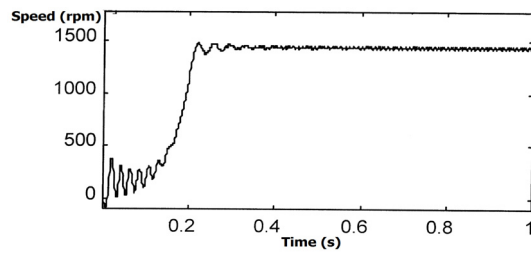
In order speed regulation to be achieved a voltage inverter is used as power supply of the motor. Motor speed is related to power supply frequency with equation (8):

$$n = \frac{60f}{p} (\text{rpm}) \quad (8)$$

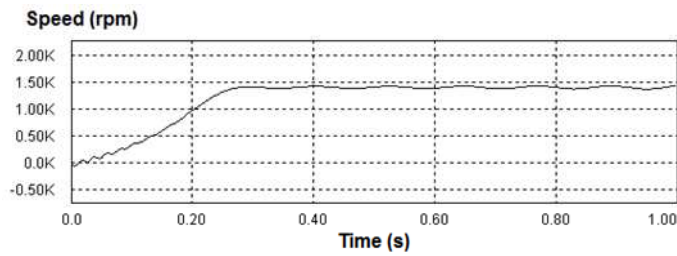
$f$  is the power supply frequency and  $p$  is the pair of poles. In this application constant torque should be maintained at constant value of  $M_s = 14$  Nm, ratio between magnitude of power supply voltage and frequency should be kept constant. In that case equation (9) is applicable:

$$\frac{n^*}{n} = \frac{f^*}{f} \quad (9)$$

Symbol \* denotes speed and frequency different from the rated one. In case when motor is supplied with variable frequency power supply, adequate values of frequencies are input in the model of voltage inverter as well as in equations for direct and inverse transformation from  $a, b, c$  system into  $d, q$  system in Simulink model while adequate firing angle of thyristors is implemented in PSIM model for different operating frequencies. In Fig. 6 and Fig. 7 transient characteristics of speed and torque when the motor is fed from inverter with frequency 50 Hz for operating regime of constant load  $M_s = 14$  Nm are presented, respectively.

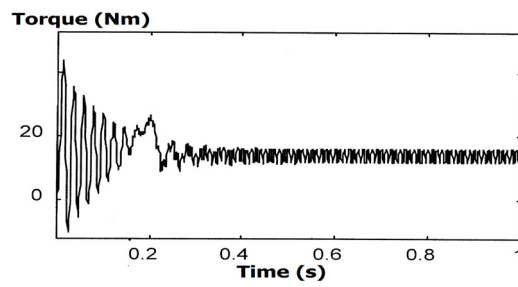


(a) Simulink model

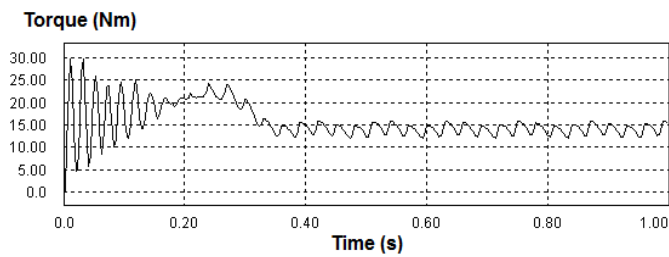


(b) PSIM model

Figure 6. Speed for power supply from inverter at 50 Hz



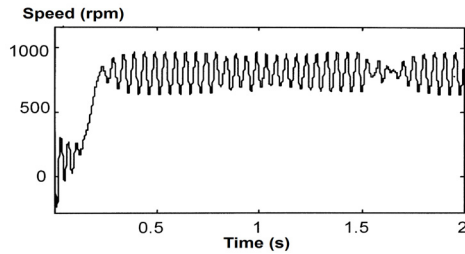
(a) Simulink model



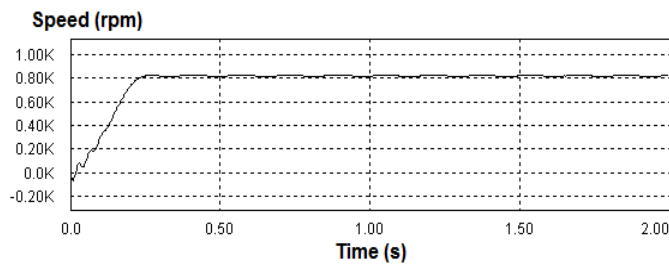
(b) PSIM model

Figure 7. Torque for power supply from inverter at 50 Hz

Comparison of Figs. 3 to 5 and Figs. 6 to 7 leads to the conclusion that the transient characteristics are quite similar with respect to the acceleration time and the final steady state values of speed, torque and current. The pulsations of torque and speed when the motor is in steady state are much higher in Figs. 6 to 7, due to the work of the inverter as a result of which higher order odd harmonics are present in their characteristics. In Figs. 8 and 9 are presented transient characteristics of speed and torque when motor is fed from voltage inverter with frequency 30 Hz for operating regime of constant load  $M_s = 14 \text{ Nm}$ .

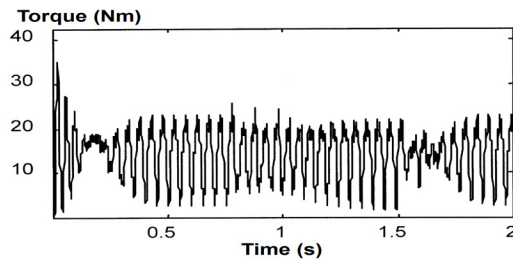


(a) Simulink model

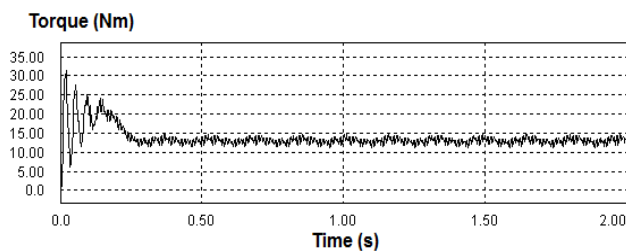


(b) PSIM model

Figure 8. Speed for power supply from inverter at 30 Hz



(a) Simulink model



(b) PSIM model

Figure 9. Torque for power supply from inverter at 30 Hz

As it is expected, according to equation (8), after the acceleration time has expired motor speed is reaching the value of 810 rpm. In Table 1 comparison of obtained results of speed, current and torque from different simulation models when the motor is supplied by voltage inverter, is presented.

Table 1. Comparison of results motor supplied from the inverter

$f = 50 \text{ Hz}$		
	Simulink model	PSIM model
Speed (rpm)	1437	1440
Electromagnetic torque (Nm)	14	13.5
Stator current (A)	5.67	6
$f = 30 \text{ Hz}$		
Speed (rpm)	850	810
Electromagnetic torque (Nm)	15	14
Stator current (A)	5.4	5.67

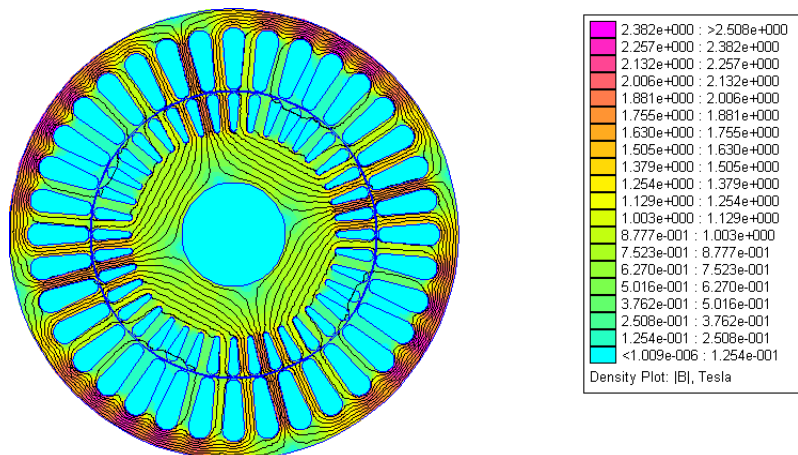


Figure 10. Flux distribution at motor cross section supply from network

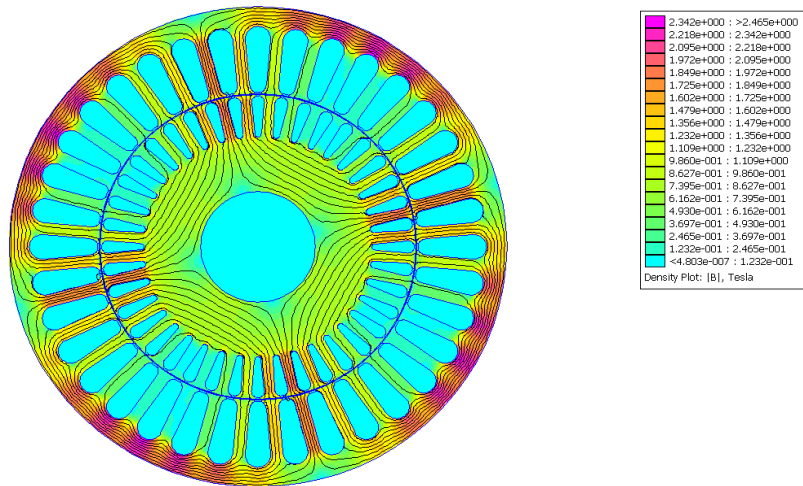


Figure 11 Flux distribution at power supply from inverter  $f = 30$  Hz

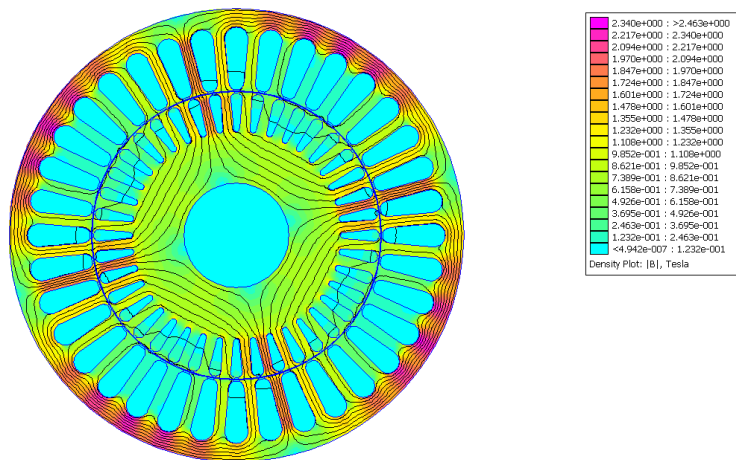


Figure 12 Flux distribution at power supply from inverter  $f = 100$  Hz

#### 4. FEM analysis

The Finite Element Method (FEM) is widely used for electromagnetic field calculations in electrical machines, in general. It is usually used as a non-linear magnetostatic problem which is solved in the terms of magnetic vector potential  $A$ . However, when analyzing induction machines, considering their AC excitation, the air-gap magnetic field is always a time-varying quantity. In materials with non-zero conductivity eddy currents are induced; consequently, the field problem turns to magneto-dynamic, i.e. non-linear time harmonic problem. When rotor is moving, the rotor quantities are oscillating at slip frequency, quite different from the stator frequency.

The problem is solved by adjusting the rotor bars conductivity  $\sigma$ , corresponding to the slip. With respect to the compound configuration of the motor, both in electrical and

magnetic sense, and taking into consideration the particular meaning of the slip  $s$ , a motor model suitable for FEM application is derived [2]. The magnetic flux distribution in the motor cross section for rated load condition at symmetrical power supply from the network with  $f = 50$  Hz as well as when motor is supplied by voltage inverter with frequency  $f = 30$  Hz and  $f = 100$  Hz are presented in Fig. 10, Fig. 11 and Fig. 12, consequently.

## 5. Conclusion

Complex analysis of induction squirrel cage motor is performed by developing mathematical, simulation and numerical motor models for calculation of motor transient performance characteristics as well as for calculation of distribution of magnetic flux density in motor's cross section.

Simulation models in SIMULINK and PSIM are developed for both cases of power supply: from the network and from voltage inverter. From obtained transient characteristics of speed torque and current in case of power supply from the network it can be concluded that simulation results of speed 1440 rpm in Simulink model and 1437 rpm in PSIM model, electromagnetic torque of 15 Nm and maximum value of current 6 A in both simulation models are showing good agreement with the data given from the producer: rated speed 1410 rpm, torque 14.9 Nm and effective value of current of 5 A. This verifies the simulation model as accurate enough to be applied in variable speed applications when motor is fed from voltage inverter. In order variable motor speed to be achieved constant Volt-Hertz characteristic is maintained which results in constant electromagnetic torque. Simulation model is built for frequency 30 Hz in Simulink as well as in PSIM. Model is showing good simulation results of speed of 810 rpm, which is adequate to the power supply frequency while electromagnetic torque is kept on value of 15 Nm. In order magnetic flux density distribution in the motor cross-section to be obtained motor model suitable for application of Finite Elements Method is developed. Obtained results proved that there is no significant increase of magnetic flux density since constant flux is maintained in all operational regimes.

## References

- [1] Krause, P. C., Wasynczuk, O., Sudhoff, S. D.: *Analysis of Electric Machinery*, IEEE Press, New York, USA, (1995).
- [2] Sarac, V., Cvetkovski, G.: *Different motor models based on parameter variation using method of genetic algorithms*, *Przegląd Elektrotechniczny*, R.87, NR3/2011, pp. 162–165.

# Investigation Some Electromagnetic Characteristic of Pm Synchronous Motor in Flux Weakening Operation

I. Szénásy

Széchenyi University, Department of Automation  
H-9026 Győr, Egyetem tér 1.  
e-mail: szenasy@sze.hu, szi001@t-online.hu

**Abstract.** The power factor, the hysteresis losses and the stator eddy current losses are electromagnetic features of permanent magnet synchronous motors. The newer method for control these motors is the flux weakening operation for extending the region over nominal speed but by nominal voltage. This paper deals with these questions and its impacts.

**Keywords:** *PM synchronous motor, flux weakening, power factor, hysteresis loss*

## 1. Introduction

Field weakening is required in order to limit the induced voltage above the nominal velocity for a PM synchronous motor also. In the case of applying permanent magnets their flux must be reduced using some applicable solution. Turning the current vector forward and further increasing in torque angle reduces the effect of the main flux. On turning the current vector ahead, this act with a constant current begins to decrease the flux. Increasing velocities and breaking it requires varying adjustment the torque angle.

We had developed a 100 kW power PMSM by Infolytica program and made simulations for investigate some characteristics on the flux-weakening region as power factor, the loss of stator teeth hysteresis and the loss of stator teeth eddy current.

## 2. Extending velocity range, field weakening

As it is known, considerably above the nominal velocity for a PM synchronous motor field weakening is required in order to limit the voltage. The flux of the magnetic field generated by the permanent magnets does not change by itself in PM synchronous motors.

Up to reaching the nominal velocity the terminal voltage must be increased in proportion to the frequency i.e., in proportion to the speed if the supply is intended to be performed by unchanged current. Without further increase in the terminal voltage, the motor cannot be used for an increase in velocity, only with a considerably decreased torque.

Fig. 1 shows the changes in the power and the voltage in function of  $\omega$ .



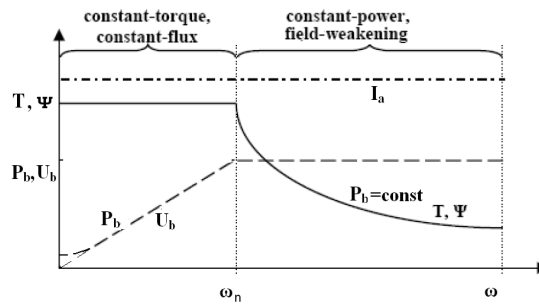


Figure 1. Torque, power and voltage vs. speed normal and flux-weakening region

In the case of speed nominal, the values of the flux and the torque are constant just as in asynchronous motors. In a range above this, only the power can remain constant applying a supply with constant voltage. On the other hand, the flux and the torque decrease in a hyperbolic way, if this intention can be realised.

For a possible use in a little city bus and supplied from battery, we had developed a surface mounted and outer rotor type PMSM motor by Infolytica program system. The type of winding is fractioned rated of slots and pole for achieving a plane torque development.

In its imagined application the maximum speed is 2500/min. The back emf is 460 V<sub>peak</sub> at 1000/min therefore above this speed the flux weakening is indispensable. The main characteristics are shown in Fig 2.

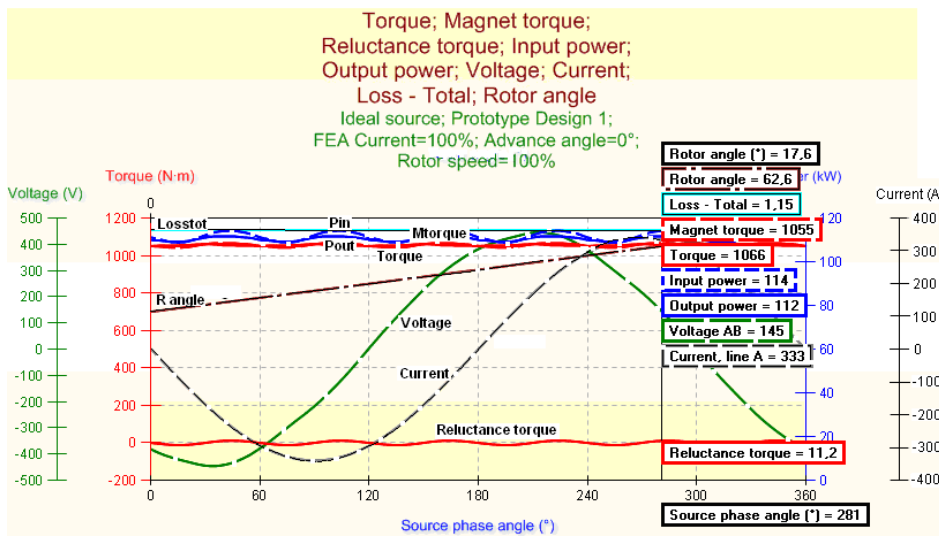


Figure 2 The main characteristics in nominal state by zero advance angle.

For realize this results we suppose a motor control with available flux-weakening operation. We have done several simulations by Infolytica for investigate some main characteristics of this PMSM in this expanded region namely the power factor, the loss of

stator teeth hysteresis and the loss of stator teeth eddy current. The functions of results are fitted by Matlab. Fig 3 shows the loss of stator teeth hysteresis vs. advance angle.

Fig. 3 shows the loss of stator teeth hysteresis vs. advance angle at speed 2000 rpm and 350 A (150%) motor current.

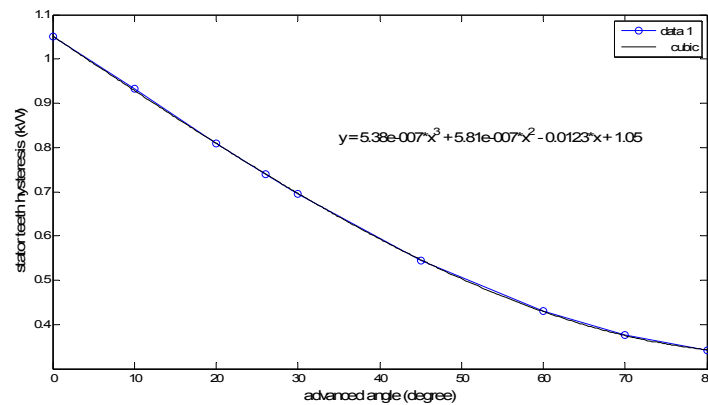


Figure 3. The loss of stator teeth hysteresis vs. advance angle. Speed 2000 rpm,  $I_{mot}$  350 A

The Fig. 4 shows the same case but by 280 A current. The losses are reduced.

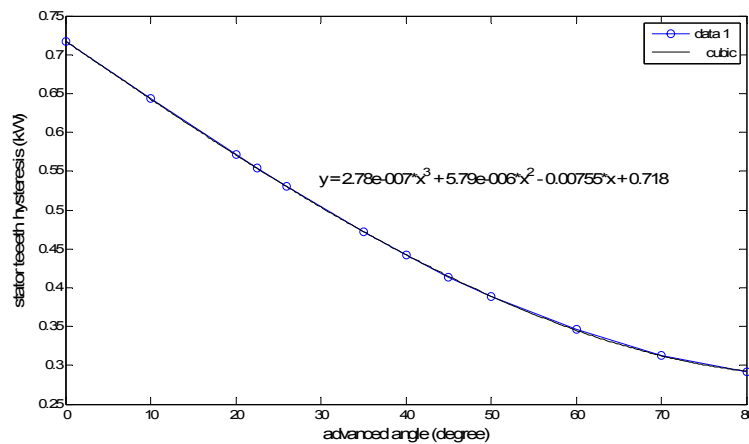


Figure 4. The loss of stator teeth hysteresis vs. advance angle. Speed 2000 rpm,  $I_{mot}$  280 A

The Fig. 5 shows the loss of stator teeth hysteresis vs. motor current at speed 2000 rpm and by advanced angle 26 degree of the current vector. This angle is very favourable for ratio of torque per current.

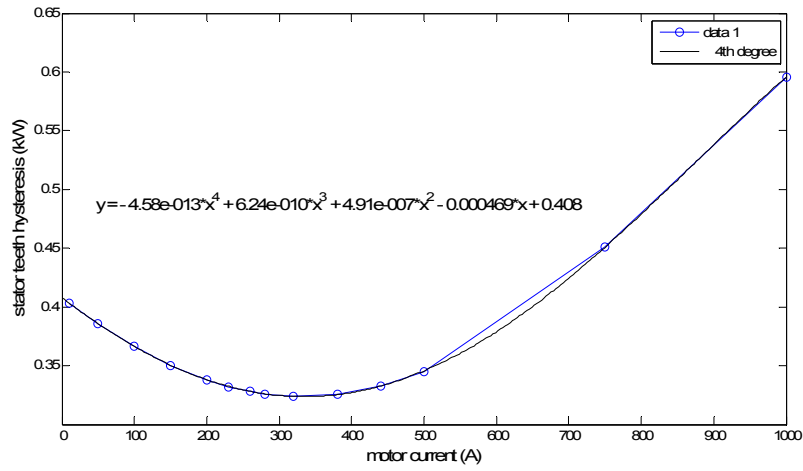


Figure 5. The loss of stator teeth hysteresis vs. motor current. Advanced angle 26 degree, speed 2000 rpm

The Fig 6. shows the stator teeth eddy current loss vs. advanced angle at speed 2000 rpm, and motor current 350 A.

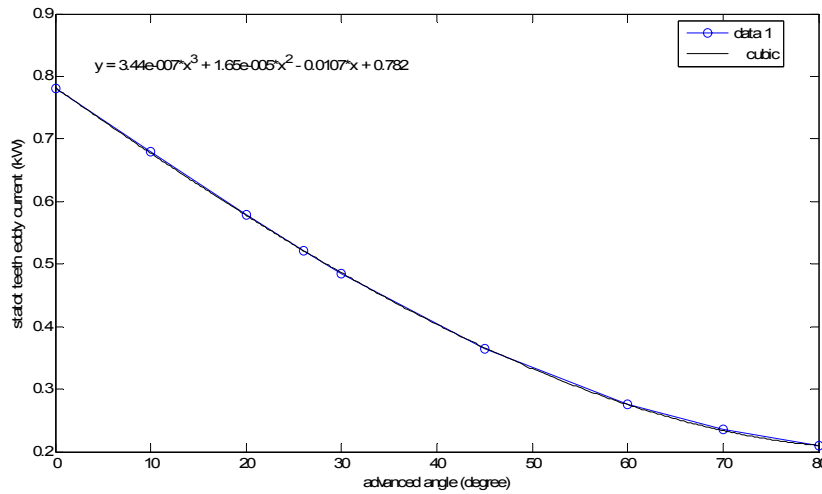


Figure 6. The stator teeth eddy current loss vs. advanced angle. Speed 2000 rpm, motor current 350 A

The Fig 7 shows the stator teeth eddy current loss vs. advanced angle at speed 2000 rpm, and motor current 280 A. The losses are reduced.

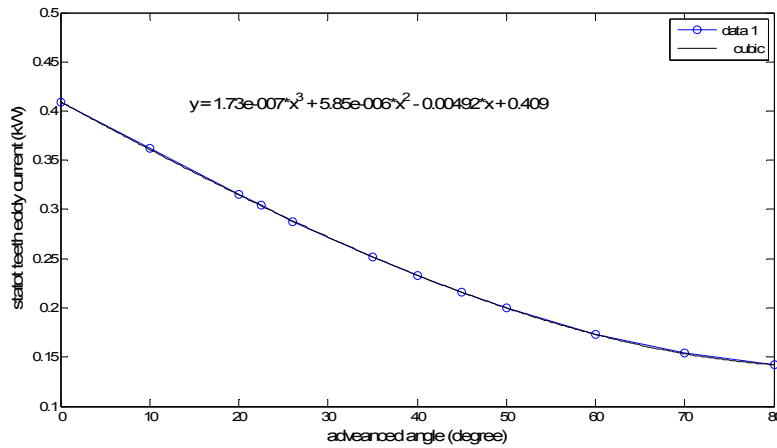


Figure 7. The stator teeth eddy current loss vs. advanced angle.  
Speed 2000 rpm, motor current 280 A

The Fig. 8 shows the stator teeth eddy current loss vs. motor current at speed 2000 rpm, and by advanced angle 26 degree.

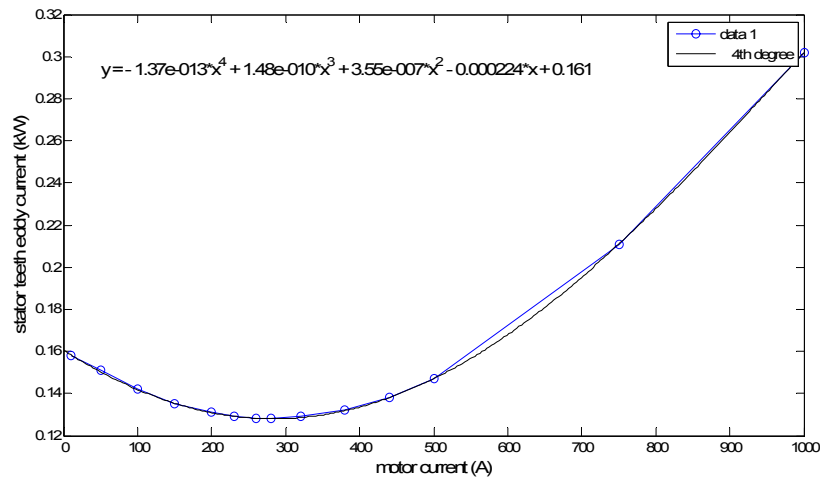


Figure 8. The stator teeth eddy current loss vs. motor current.  
Speed 2000 rpm, advanced angle 26 degree

### 3. The question of power factor

It is known that AC motors need reactive power for its operation both motoring and braking regime. Regarding that DC link can supply only real power, then the reactive power must generated by the inverter. Consequently the inverter can be considered as a reactive power generator. Inverter must control the voltage phase angle. The ability to control the phase of the voltage has been realised by solid state power switching and has significant impact on the control of AC machines.

The inverter handles both the real and reactive power. The apparent power from produced these components rates of the inverter and make the cost and pricing of it. Unity power factor operation provides the minimum needed of current of inverter but that is not possible in induction motor drives as this machine require significant magnetizing current. On contrary PMSMs are capable of unity power operation, or very close in it by varied advanced angle operation.

The Fig. 9 shows the power factor vs. motor speed at motor current 120 A and advanced angle 0 degree.

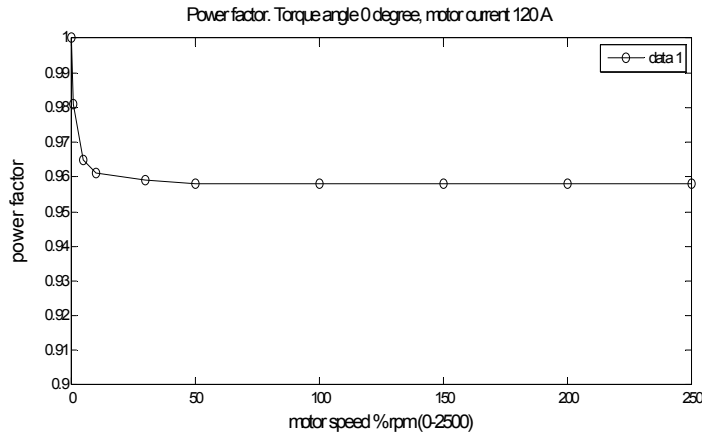


Figure 9. The power factor vs. motor speed.  
Motor current 120 A, advanced angle 0 degree

Fig. 10 shows the power factor vs. motor speed at motor current 240 A nominal value, and advanced angle is 0 degree. The power factor significantly reduced on entirely speed region.

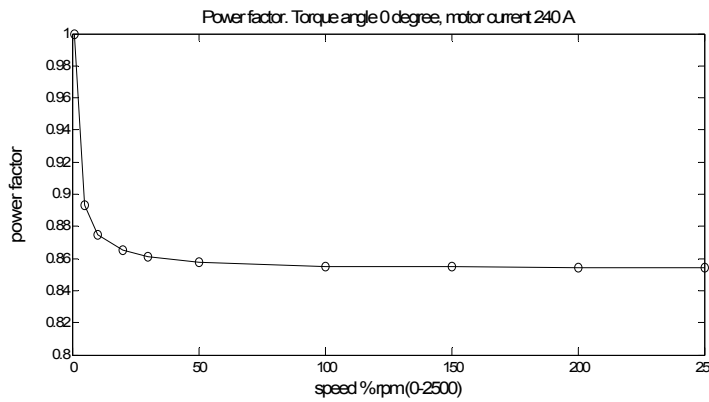


Figure 10. The power factor vs. motor speed.  
Motor current 240 A, advanced angle 0 degree

Fig. 11 shows the power factor vs. advanced angle at motor current 280 A nominal value, and the speed is 1000 rpm. The power factor is significantly high, close to unit on a medium advanced angle region.

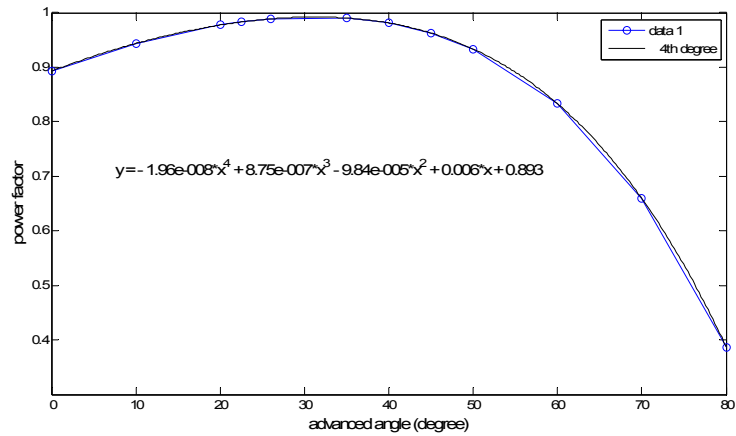


Figure 11. The power factor vs. advanced angle.  
Speed 1000 rpm. Motor current 280 A

Fig. 12 shows the power factor vs. advanced angle at motor current 350 A nominal value, and the speed is 2000 rpm. The power factor is high, close to unit in a medium advanced angle region, but without advanced angle operation the power factor is constant 0.85.

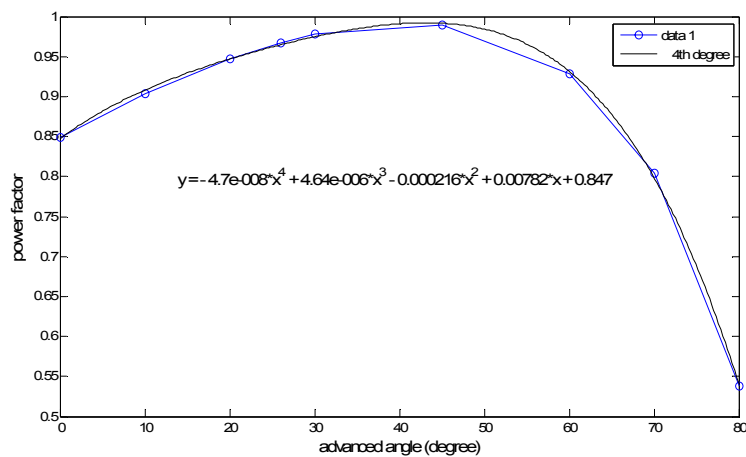


Figure 12. The power factor vs. advanced angle.  
Speed 2000 rpm. Motor current 350 A

Fig. 13 shows the power factor vs. motor current at motor speed of 1000 rpm, and the advanced angle is of 26 degree. The power factor is high, close to unit in a little medium current region between 200 and 300 A and over this value tends to 0.5.

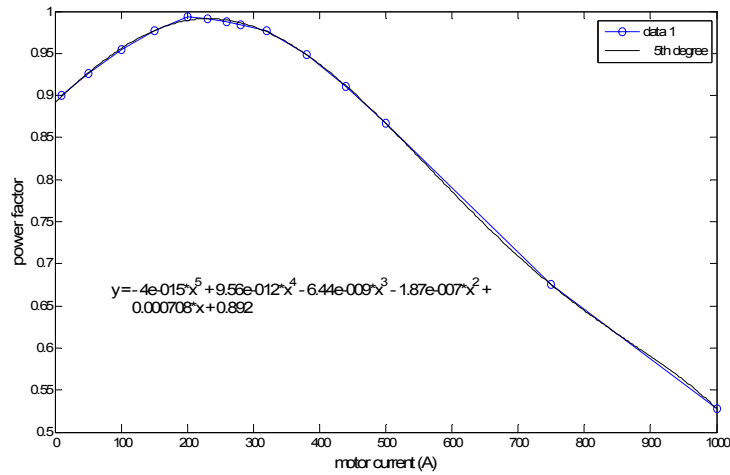


Figure 13. The power factor vs. motor current.  
Speed 1000 rpm. Advanced angle 26 degree

Fig. 14 shows the power factor vs. motor current at motor speed 1500 rpm, and the advanced angle is 70 degree for achieve an extended speed in motoring region. The power factor is high, close to unit in a little medium current region between 150 and 250 A.

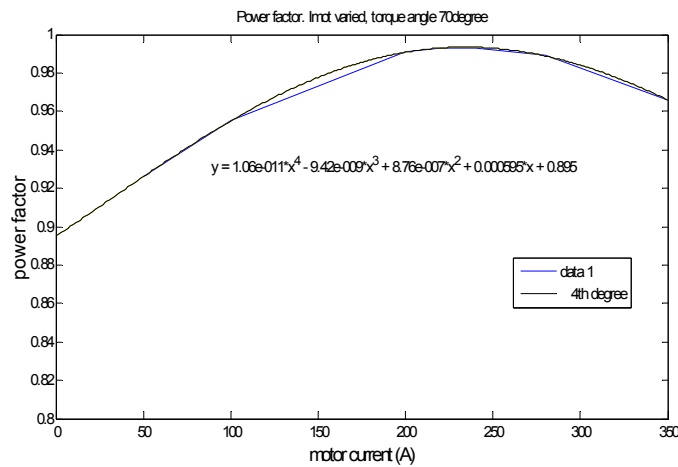


Figure 14. The power factor vs. motor current.  
Speed 1500 rpm. Advanced angle 70 degree

Fig. 15 shows the function of flux, inductances, reactances, torque and voltage factors vs. motor current at speed of 1000 rpm. and advanced angle of 45 degree.

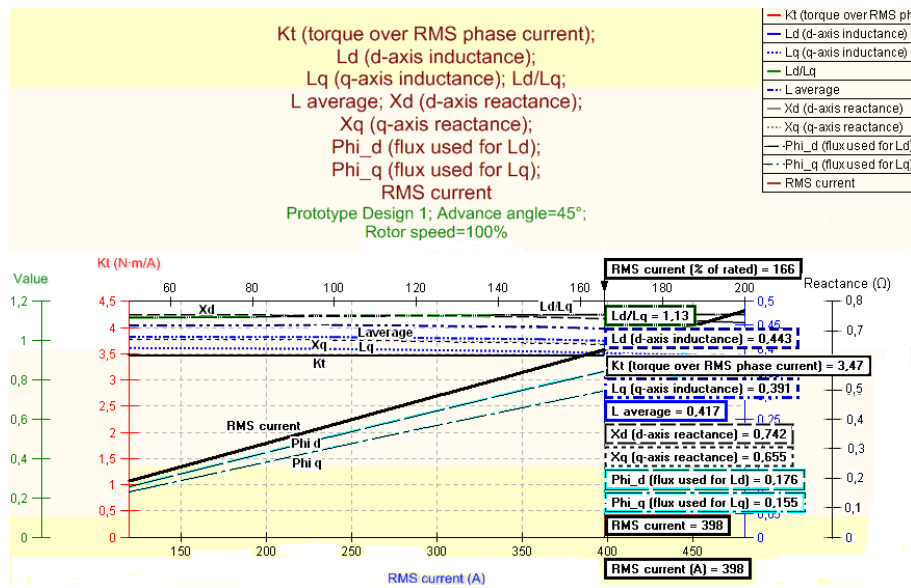


Figure 15. The flux, inductances, reactances, torque and voltage constanses vs. motor current. Speed 1000 rpm. Advanced angle 45 degree

#### 4. Conclusions

The applied flux weakening operation for extend the speed range under nominal voltage bring some appreciable features in motoring and breaking regime of permanent magnet synchronous motors. Improve the power factor an a little region and reduce the losses of magnetic circle.

#### References

- [1] Szénásy, I.: *Some developing and controlling problems of PMSM motors applied for modern drives for EV-s*, Presentation in Conference to Drive for Road Vehicle, by MTA, Budapest, (2012).
- [2] Krishnan, R.: *PMSM and Brushless DC Motor Drives*, CRC Press (2010).



# Computationally Efficient Representation and Implementation of the Preisach-model of Hysteresis

Z. Sari

University of Pécs,  
Pollack Mihály Faculty of Engineering and Information Technology,  
Pécs, Hungary Pécs, Rókus 2., e-mail: [ski@morpheus.pte.hu](mailto:ski@morpheus.pte.hu)

**Abstract.** The paper deals with the details of representation and implementation of the Preisach-model of hysteresis in order to be efficiently applicable in numerical computations, particularly in finite element modelling and analysis.

**Keywords:** *hysteresis modelling, numerical analysis, COMSOL-Matlab*

## 1. Introduction

The main goal of the paper is to describe the representation and implementation details of a hysteresis model into finite element analysis of a field calculation problem in the COMSOL-Matlab environment. It will be shown, that the quite difficult task of representation and implementation of a complicated hysteresis operator can be handled relatively easily by means of an appropriate description of the hysteresis operator and the efficient usage of the high level software environment, what the interaction of the COMSOL and Matlab packages can offer.

Since there are numerous engineering fields, where the proper application of a hysteresis operator is required, (like ferromagnetics, porous media flow, fatigue of mechanical structures, vapour-liquid phase transitions etc.) and the 'mainstream' numerical tool for the solution of these kind of problems is the Finite Element Method (FEM), it is a naturally arising need, that the hysteresis operator of choice should be ready to use, directly in the high-level FEM packages. Since the commercial FEM packages do not provide hysteresis models directly, it relies on the user building his/her implementation. In the paper a simple hysteretic diffusion problem is solved as a case study in the COMSOL Multiphysics finite element analysis software, and by the aid of this case study, the details of application of a hysteresis model in the COMSOL-Matlab environment is presented.

## 2. The Comsol FEM package and the Matlab environment

As the primary tool for the finite element analysis of the problem, the COMSOL Multiphysics engineering simulation software is applied. The COMSOL package is a high level modelling and simulation environment providing tools for all steps of modelling (geometry definition, mesh generation, physics definition, solution, post-

processing etc.), and having a set of very advantageous properties, which enables a highly customized way of building models, and running simulations. One of the most important features of the package is the equation-based modelling, facilitating the weak form representation of the partial differential equations (PDEs) of the problem, which is really advantageous, because by the application of the weak form, the user has full control over the physics defined on various domains of the modelled geometry. Another extremely useful feature is the capability of using functions written in the Matlab environment. This way, practically any kind of function or multi-valued operator can be implemented into the finite element model. As a consequence of the fundamental nature of the connection between COMSOL and Matlab, implementing a hysteresis operator requires a fair amount of initialization tasks preceding the actual usage of the operator, but after that, it can be used easily, as if it was a part of the FEM package.

### 3. The Preisach Operator

The defining equation of the operator applied here is based on the work of P. Krejci et al. [2]

$$\mathcal{P}[\lambda, u](t) = \int_0^\infty g(r, \wp[\lambda, u](t)) dr, \quad (1)$$

$$g(r, v) = \int_0^v \varphi(r, z) dz, \quad (2)$$

where  $u$  is the input of the operator,  $r$  is the abscissa of the phase space, the auxiliary function  $g$  contains the integration of the distribution function  $\varphi$  (the usual Preisach-distribution) over the phase space, where the upper bound  $\wp[\lambda, u](t)$  of integration (2) is the output of the memory operator  $\wp$ , and  $\lambda$  is a function of the  $\Lambda$  phase space. The definition of the phase space is

$$\Lambda = \{ \lambda : \mathbb{R}_+ \rightarrow \mathbb{R} : |\lambda(r) - \lambda(s)| \leq |r - s| \forall r, s \in \mathbb{R}_+ : \lim_{r \rightarrow \infty} \lambda(r) = 0 \}, \quad (3)$$

which represents a set of functions with the property of having a maximum absolute steepness of one, and having value of zero at  $r \rightarrow \infty$ . This definition basically describes an infinitely large triangle bounding the functions of the phase space. The actual state of the phase space (the concrete  $\lambda$  function) represents the memory of the hysteresis operator. Putting (1) and (2) together gives a double integral defining the Preisach-operator as

$$\mathcal{P}[\lambda, u](t) = \int_0^\infty \int_0^{\wp[\lambda, u](t)} \varphi(r, z) dz dr, \quad (4)$$

where the integration takes place over a subdomain of the phase space, defined by the actual state function  $\lambda$ , which can be obtained from the memory operator.

### 4. The implementation of the hysteresis operator

In order to implement the operator (4) into a numerical computation it is advantageous to make some practical modifications. First of all, in order to apply an operator in a

numerical environment, the phase space has to be finite. In other words, infinitely large inputs are not allowed, thus an upper bound value  $u_s$  has to be introduced. Besides the construction of the finite phase space defined as

$$\Lambda = \{\lambda : \mathbb{R}_+ \rightarrow \mathbb{R} : |\lambda(r) - \lambda(s)| \leq |r - s| \forall r, s \in \mathbb{R}_+ : \lim_{r \rightarrow u_s} \lambda(r) = 0\}, \quad (5)$$

I have introduced a memory operator  $\nu$ , which is responsible for the computation of the new state (memory function) in view of the actual state  $\lambda$ , the input  $u$ , and the time derivative  $\dot{u}$  of the input. The defining equation (4) of the Preisach-operator thus replaced by

$$\mathcal{P}[\lambda, u, \dot{u}](t) = \int_0^{u_s} \int_{r-u_s}^{\nu[\lambda, u, \dot{u}](t)} \varphi(r, z) dz dr, \quad (6)$$

which contains the memory operator  $\nu$  as the upper bound of the inner integration having the same role as the memory operator  $\wp$  in (4), but with a different realization.

### 5. The structure of the phase space and the behaviour of the memory operator

The phase space defined by (5) is basically a usual Preisach-triangle rotated by 45 degrees counter-clockwise. The role of the memory operator  $\nu[\lambda, u, \dot{u}](t)$  is to calculate the new state function  $\lambda$  based on the actual state and the input. The behaviour of the operator in the phase space (Preisach-triangle) can be tracked by the aid of Fig. 1, which shows a possible state function and the corresponding hysteresis curve.

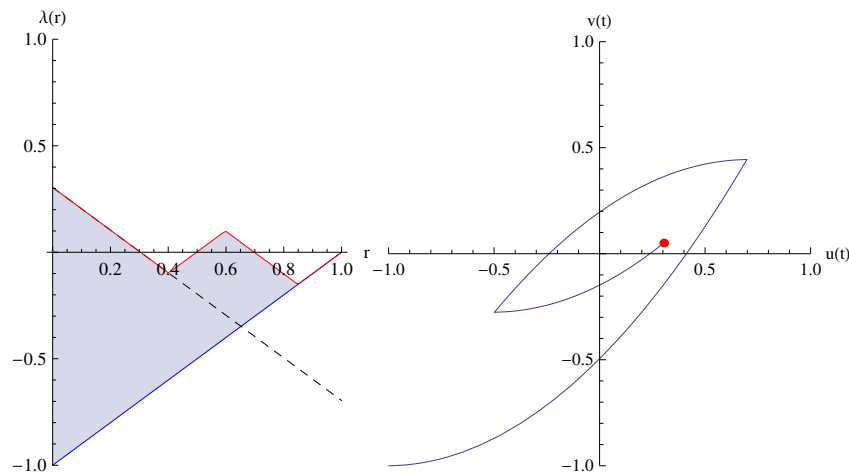


Figure 1. A state function in the phase space with the corresponding hysteresis curve

In the left subfigure the memory function  $\lambda(r)$  can be seen as the upper boundary of the filled region of the phase space, the lower boundary is  $l(r) = r - u_s$ , where the  $u_s$  is normalized to  $\{-1, 1\}$  in the figure.

Integration (6) takes place over the filled subdomain of the phase space bounded by the fixed “lower” side of the triangle and the continuously changing memory function resulting from the memory operator. The input-output relation of the operator appears as a hysteresis curve, which can be seen in the right hand side subfigure, where  $u(t)$  and  $v(t)$  denotes the input and the output of the operator (6) respectively. The memory operator utilizes an auxiliary line  $e(r) = -\text{sgn}(\dot{u})r + u$  (dashed line in figure) for the purpose of tracking the changes of the phase space. The intersecting point of the  $e(r)$  line and the  $\lambda(r)$  axis represents the actual value of the input  $u(t)$ , and starting from a given state (for example the one depicted in Fig. 1.) the change of the input of the hysteresis operator causes the moving of the  $e(r)$  line upwards or downwards depending on the sign of the time derivative of the input. The moving of  $e(r)$  results in a new intersection point of the  $e(r)$  line with the actual state function  $\lambda(r)$ , and the new memory function is constructed simply by “concatenating” the segment of  $e(r)$  preceding the intersection with the segment of  $\lambda(r)$  beyond the intersection.

Fig. 2 shows the new state and the corresponding hysteresis curve after decreasing the value of the input  $u(t)$ .

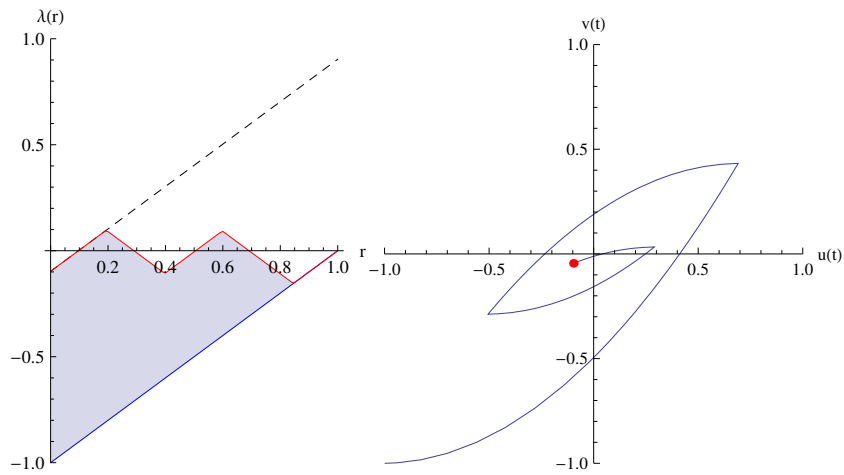


Figure 2. State function and hysteresis curve after decreasing the input from state depicted in Fig. 1

Further decreasing the input results in “wiping out” the portion of memory (state function), which represents the inside minor loop, which can be seen in Fig. 3.

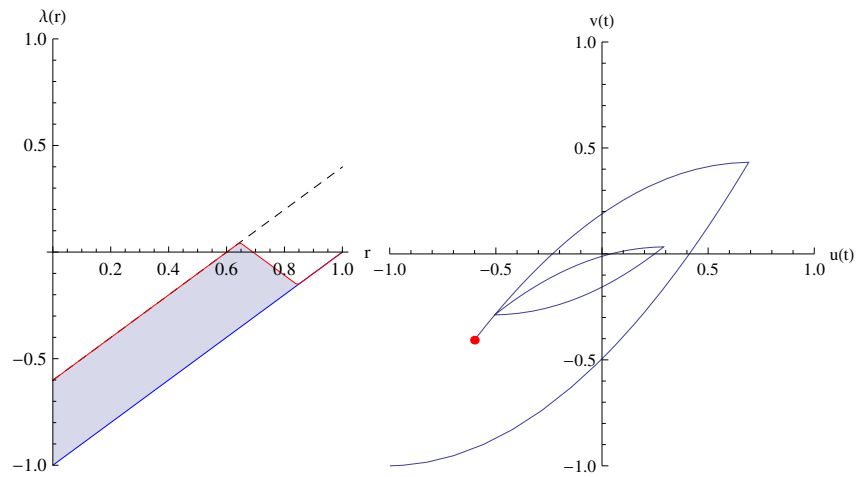


Figure 3. Phase space and hysteresis curve after a “wipe out”

The main advantage of this representation is, that the complicated changes in the phase space can be tracked very easily by the aid of the introduced memory operator, since the line  $e(r)$  can be constructed without any problems in view of the input of the hysteresis operator and the state function representing the memory is described by a single-valued function, which is very easy to handle as well.

The Matlab (or any suitable numerical tool) implementation of the operator described above consists of the discrete representation of  $\lambda(r)$  in a form of a finite dimensional vector, and the main task to perform is to find the intersection of  $e(r)$  and  $\lambda(r)$  in order to construct the new state function. The method of finding the intersection is the following

$$i_m = \left\langle \frac{1}{2} \Delta[\text{sgn}(\mathbf{e} - \boldsymbol{\lambda})], \mathbf{i} \right\rangle, \quad (7)$$

where  $\mathbf{e}$  and  $\boldsymbol{\lambda}$  are the vectors of  $\square^m$  corresponding to the discretized  $e(r)$  and  $\lambda(r)$  respectively,  $\Delta$  is the difference operator,  $\mathbf{i} = [1, 2, \dots, m]$  is an index vector,  $\langle \cdot, \cdot \rangle$  denotes the usual dot product, and  $i_m$  is the index of the intersection point. After finding the location of the intersection, the construction of the new state function is straightforward.

The representation outlined here can be immediately applicable to define a Preisach-operator in a numerical environment, and furthermore – resulting from the nature of the memory operator applied – the algorithm is easily vectorizable, so it can be implemented into finite element computation as is. One further point is, that the integration of the distribution over the phase space can be calculated off-line, thus during the actual computation it can be substituted by interpolation, which significantly speeds up the procedure of numerical computation.

## 6. Implementation of the hysteresis operator into finite element computation

The finite element implementation is demonstrated through a case study in the COMSOL environment. Since COMSOL is highly customizable, can handle complicated nonlinear problems, and it is possible to use Matlab functions directly from the user interface without explicit usage of Matlab, it is a really good tool for solving nonlinear problems involving hysteresis phenomena.

The problem solved in the case study is a one-dimensional nonlinear diffusion problem defined as

$$\dot{H} - \frac{1}{\sigma\mu_0} \nabla^2 H = -\dot{M}, \quad M = \mathcal{P}\{H\}, \quad (8)$$

where  $H$  is the magnetic field strength,  $M$  is the magnetization, and  $\mathcal{P}\{\cdot\}$  denotes the Preisach-operator. In the COMSOL environment, after defining the diffusion equation (8) as the governing physics, the hysteretic relation has to be defined. It can be managed by defining an auxiliary dependent variable for  $M$ , and providing the weak-form equation connecting the auxiliary variable  $M$  and the hysteresis operator, which is represented by a variable assigned to the predefined Matlab function. The Matlab function definitions can also be done from the COMSOL environment in the global definitions section.

Solving the problem defined by (8) on a one-dimensional domain results in the time evolution of the  $H$  and  $M$  fields. In Fig. 4 and Fig. 5 minor hysteresis curves can be seen corresponding to different locations in space, which were obtained by solving the nonlinear diffusion problem with the application of the Preisach-operator using the representation described above. (The value of magnetization is normalized to  $[0,1]$ .)

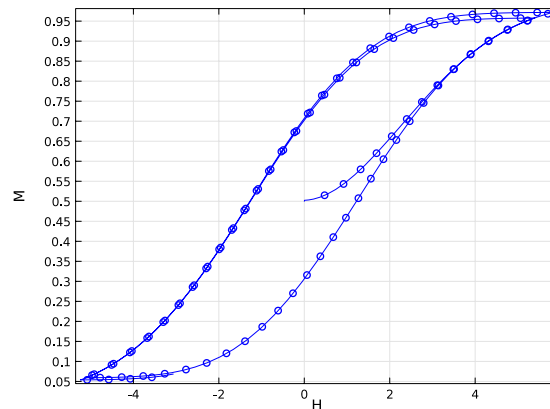


Figure 4. Minor hysteresis curves

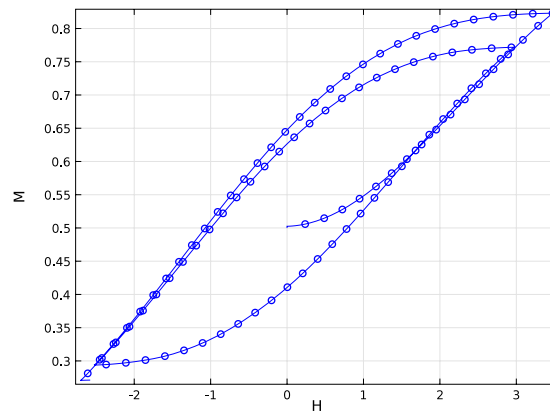


Figure 5. Minor hysteresis curves

It is important to emphasize, that after initializing the Preisach-model in the Matlab environment, it can be used similarly to a built-in function in COMSOL by the aid of an auxiliary dependent variable defined by a weak expression, and this way most of the programming difficulties of the Matlab implementation can be avoided, since the hysteresis operator can be used directly from the COMSOL user interface, and all of the modelling tasks (solution, post-processing) can also be accomplished without explicit usage of Matlab, which has the clear advantage of using a high level user-friendly interface instead of tweaking with the subtleties of programming.

## 7. Conclusion

As a concluding remark it can be stated, that the representation and the implementation outlined in the paper can be a productive way of application of the Preisach-model of hysteresis for handling nonlinear numerical field calculation problems involving hysteresis phenomena

## References

- [1] Iványi, A.: *Hysteresis Models in Electromagnetic Computation*, Budapest, Academic Press, (1997).
- [2] Brokate, M., Eleuteri, M., Krejci, P.: *On a model for electromagnetic processes in ferromagnetic materials with hysteresis and space dependent electric conductivity*, *Mathematical Methods in the Applied Sciences*, (2008), pp. 1545–1567.

# Analysis of Photovoltaic Modules Characteristics

F. Pranjić, P. Vrtič

University of Maribor, Faculty of Energy Technology  
Hočevarjev trg 1, 8270 Krško,  
e-mail: franjo.pranjic@uni-mb.si, peter.virtic@uni-mb.si.

**Abstract.** Nowadays, photovoltaics is one of the most popular and interesting areas, especially in the economy. This paper presents an analysis of characteristics of photovoltaic modules. The comparisons between the characteristics provided by the manufacturers and characteristics obtained by measurements, under the real time conditions are accomplished. The temperature dependence of power and the actual energy production are also presented. Measurements are obtained directly from the module without the inverter.

**Keywords:** *photovoltaics, energy production, specific energy yield.*

## 1. Introduction

European Union's directive, upon increasing the production of electricity from the renewable energy sources till 2020, has contributed to the growth of photovoltaic (PV) systems connected to the electric grid. The main elements of the PV systems are solar modules, which convert the solar radiation directly into the electricity. The efficiency of this conversion depends on the solar radiation that reaches the surface of the solar cells, the temperature of the solar cells, the impedance matching between the solar modules and DC/DC converters, and the quality of the inverters [1].

In this paper, the analysis of characteristics of four photovoltaic (PV) modules is presented. The comparisons under real conditions are accomplished between characteristics provided by the manufacturers and characteristics obtained by measurements. The temperature dependence of electric power and actual energy production is also presented. Measurements are accomplished on the PV module without the inverter. All sample PV modules are measured at the same time, therefore identical conditions are ensured.

## 2. Measuring system and method

Measurements are performed by using an automatic measuring system for characteristics monitoring of PV modules (MSPV01) as shown in Fig.1.

Measuring system is able to measure current-voltage characteristics, total solar radiation on horizontal basis and temperature. From these data the electric power is calculated. Measured results are stored into the personal computer database after each measurement. In order to process measured results the LabVIEW software produced by



National Instruments is used. LabVIEW receives data from multiple outputs of the instrument MSPV01 and stores them into the database to enable subsequent analyses and comparisons. MOSFET transistors that withstand intermittent electric load are also part of the measuring system. Current pulses represent the load of the PV modules and on their basis the maximum power point (MPP) of PV modules is achieved [2].



Figure 1. Measuring system for characteristics monitoring of PV modules (MSPV01)

PV modules are measured at three different slopes: 30°, 45° and 60°. The next measuring test is carried out with two partially shaded PV modules at the slope of 30°.

The efficiency given by the manufacturer is additionally verified by using (1).

$$\eta_{STC} = \frac{P_{STC}}{AG_{STC}} \cdot 100\% \quad (1)$$

where:  $\eta_{STC}$  – efficiency calculated at standard test conditions,  $P_{STC}$  – power calculated at standard test conditions,  $A$  – active surface of the module and  $G_{STC}$  – irradiance at standard test conditions.

Equation (2) presents the efficiency calculated on the basis of measured electric power and measured irradiance.

$$\eta_m = \frac{P_m}{AG_m} \cdot 100\% \quad (2)$$

where:  $\eta_m$  – efficiency calculated on the basis of measured power and measured irradiance,  $P_m$  – measured electric power,  $G_m$  – measured irradiance.

Figure 2 shows the solar irradiance for the first day. The same measurements have been accomplished for the other days as well. The thick line represents the horizontal solar irradiance and the dashed line represents the solar irradiance that falls onto the surface of the PV module.

Analytically calculated electric power is determined by using (3).

$$P_a = P_{STC} \frac{G_m}{G_{STC}} (1 - \gamma(T_m - T_{STC})) \quad (3)$$

where:  $P_a$  – analytically calculated power,  $P_{STC}$  – power calculated at standard test conditions,  $G_m$  – measured radiation,  $G_{STC}$  – irradiance at standard test conditions,  $\gamma$  – temperature coefficient of power,  $T_m$  – measured temperature of the module,  $T_{STC}$  – temperature of the module at standard test conditions.

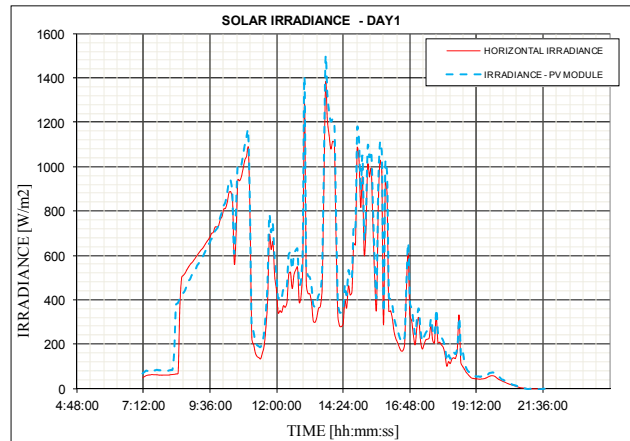


Figure 2. Solar irradiance for day 1

The comparison between calculated efficiency on the basis of measurements and the efficiency given by the manufacturer is accomplished. These results are also compared with those obtained by shaded PV modules. Two modules of the same manufacturer with the same nominal power are used as measuring objects. The back side the first PV module is thermally insulated with Styrofoam and the second PV module is without additional thermal insulation. Both electrical power and temperature of PV modules are compared as well.

### 3. Results

Table 1 shows calculated efficiencies by using (2) and efficiencies obtained by datasheets. The efficiency obtained by the manufacturer (datasheets) is in good agreement with a calculated efficiency by using (2).

Table 1. Comparison of efficiencies

Slope	Efficiency calculated by using (2)			Efficiency given by the manufacturer at STC
	30°	45°	60°	
Module 1	15%	15%	15%	14.3%
Module 2	15%	14%	15%	14.3%
Module 3	15%	15%	15%	14.1%

Figures 3, 4 and 5 show the difference between calculated electric power of PV module 2 by using (3) and the measured power of PV module 2.

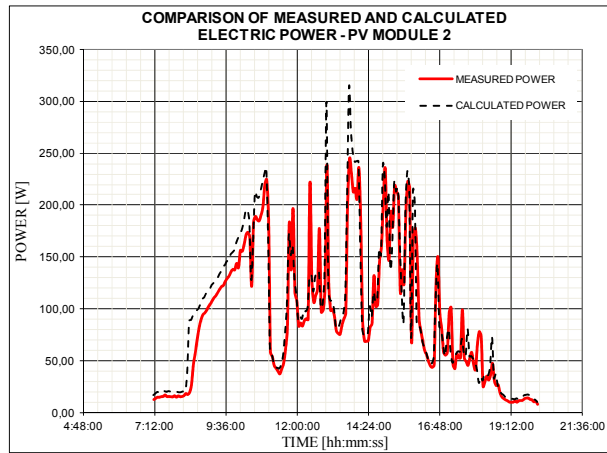


Figure 3. Comparison of calculated electric power of PV module 2 by using (3) and the measured power of PV module 2– day 1

The comparison has been conducted for three days. Figures 3, 4 and 5 are for day 1, 2 and 3. Thick lines in the figures represent the measured electrical power and dashed lines represent the calculated electrical power by using (3). Deviation between calculated electric power and measured power occurs due to the measuring instruments which causes the load in the form of pulses.

Deviation between calculated electric power and measured power occurs due to the measuring instruments which causes the load in the form of pulses. The electric power of a PV system depends on the solar radiation that reaches the surface of the PV modules, the active surface of the modules, their efficiency, and the applied maximum power point tracker (MPPT) [3].

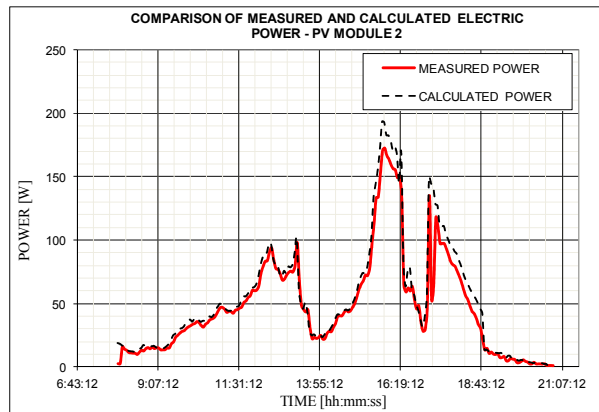


Figure 4. Comparison of calculated electric power of PV module 2 by using (3) and the measured power of PV module 2– day 2

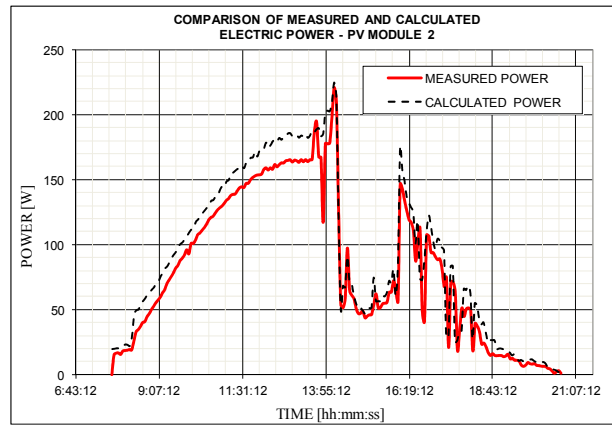


Figure 5. Comparison of calculated electric power of PV module 2 by using (3) and the measured power of PV module 2– day 3

Table 2. Comparison between insulated and non-insulated PV module

	$P1_{average}$ (W)	$P2_{average}$ (W)	Deviation (W)	Deviation (%)	$T1_{average}$ (°C)	$T2_{average}$ (°C)	Deviation (°C)	Deviation (%)
<b>Slope: 30</b>								
Day1	80	84	3.6	-4.3	43	34	9.7	23
Day2	85	92	6,5	-7.1	42	36	6.3	15
<b>Slope: 45°</b>								
Day1	46	46	0,3	-0.7	33	28	5.3	16
Day2	76	80	3,9	-4.9	42	33	8.5	21
<b>Slope: 60°</b>								
Day1	73	76	2,7	-3.6	45	37	8.7	19
Day2	54	54	0,9	-1.6	36	30	5.7	16
<b>Slope: 30° with shading</b>								
Day1	12	12	-0.1	0.9	40	31	9.1	23

Figure 6 shows the temperature of PV modules and ambient temperature for three days. Modules are of the same rated power and from the same manufacturer. Module 1 is isolated by Styrofoam. Average electrical power is calculated by summing the individual measured results divided by the number of measured results for different days. The lowest line in the figure represents the ambient temperature, and the highest line represents the temperature of Styrofoam insulated PV module. It is obvious that the temperature of this PV module is much higher than the temperature of other PV modules, hence smaller efficiency is expected.

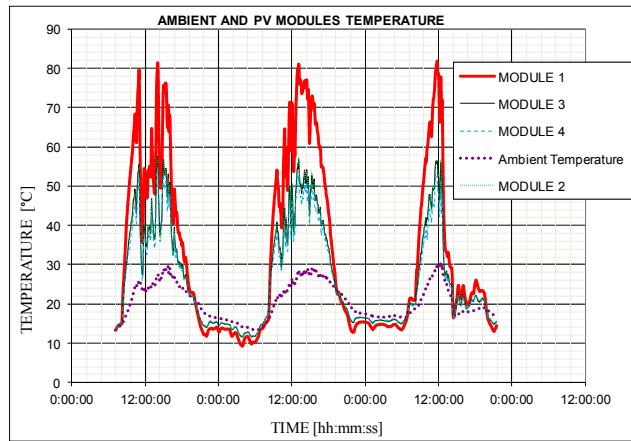


Figure 6. Ambient and PV modules temperature

Figures 7 and 8 show how shaded the PV modules are as well as the operating mode of PV modules. PV modules 1, 2 and 4 are standard ones with three operating sectors (3 bypass diodes), but PV module 3 is a special one, with 9 operating sectors (9 bypass diodes).



Figure 7. Shading of PV modules

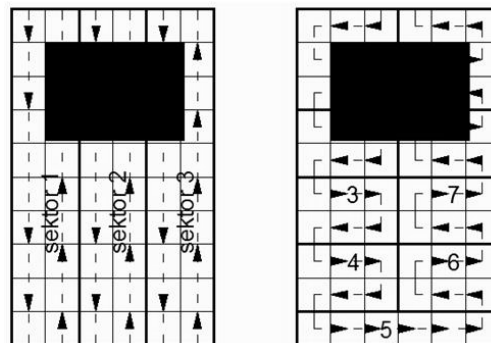


Figure 8. Operating mode of PV modules

Comparison is made between PV modules with 3 and 9 bypass diodes. In order to see the difference between them they have to be shaded. Posters of the same dimensions are used on all PV modules and placed on the same position as shown in Fig. 7. The advantage of

PV module with 9 bypass diodes is that it has 9 operating sectors, which are divided as it is shown in Fig. 8. Fig. 8 also shows how the operating sectors are divided in PV modules with 3 bypass diodes. The principle is that when some cells of one sector are covered, the whole sectors barely work. As can be seen from Fig. 7 and 8, poster covers all 3 sectors on PV modules with 3 bypass diodes and only 4 on PV module with PV module with 9 bypass diodes. That means that 5 out of 9 sectors operate normally.

Figure 9 shows the specific energy yield of PV modules. The upper line represents the energy yield of PV module 3 which is the one with 9 bypass diodes. When the PV modules are shaded it is obvious that PV module 3 has the biggest energy yield in comparison with the others. It is confirmed with Fig. 10, which shows the daily power diagram of PV modules. Thick line is much higher than other lines. Of course PV module 3 works with less efficiency due to the shading; max power is 150 Wp when it should be around 230 Wp. Other PV modules work with around 15% of their capability because of the shading.

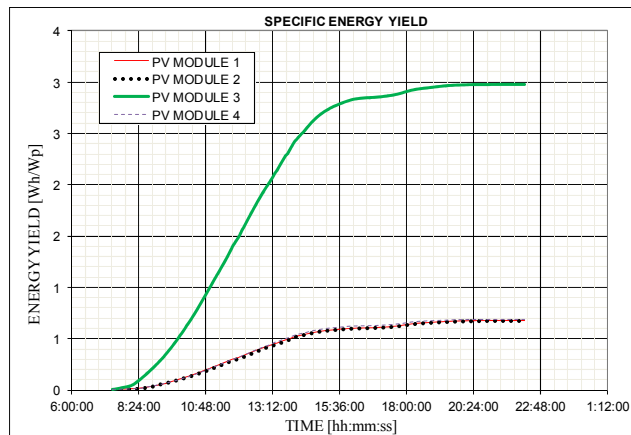


Figure 9. Specific energy yield of shaded PV modules

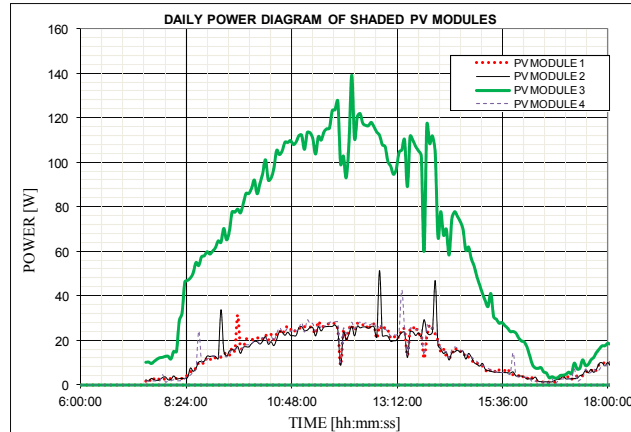


Figure 10. Daily power diagram of shaded PV modules

#### 4. Measured efficiencies of PV modules

Some of the reasons for the actual efficiency of cells being lower than the theoretical limitation are:

- Reflection of light from the surface of the cell.
- Shading of the cell due to current collecting electrical contacts.
- Internal electrical resistance of the cell.
- Recombination of electrons and holes before they can contribute to the current [2].

Figure 11 shows the efficiencies of PV modules at the slope of 30°, Fig. 12 at slope 45° and Fig. 13 at slope 60°. The peaks in the characteristics occur due to the measuring errors of the measuring equipment.

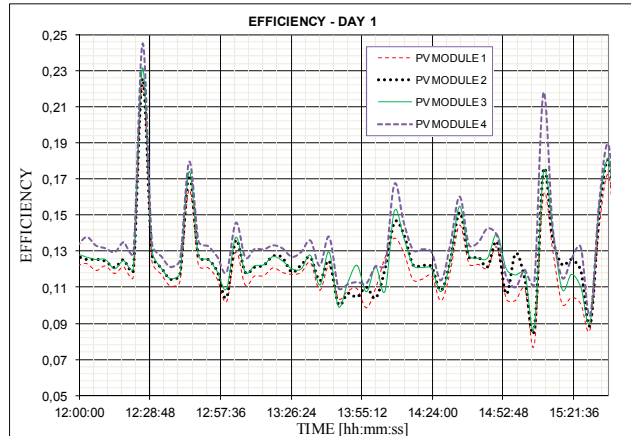


Figure 11. Efficiencies at slope 30°

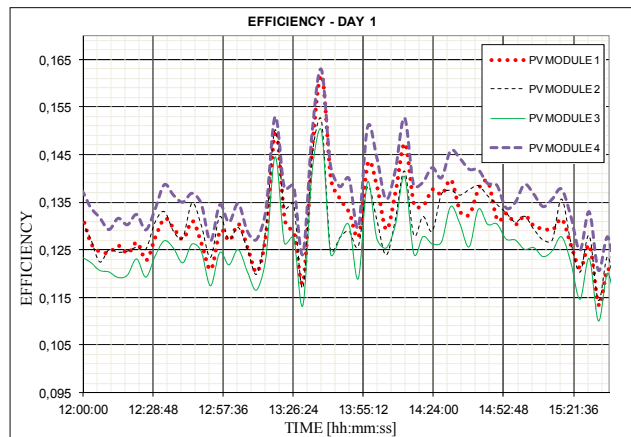


Figure 12. Efficiencies at slope 45°

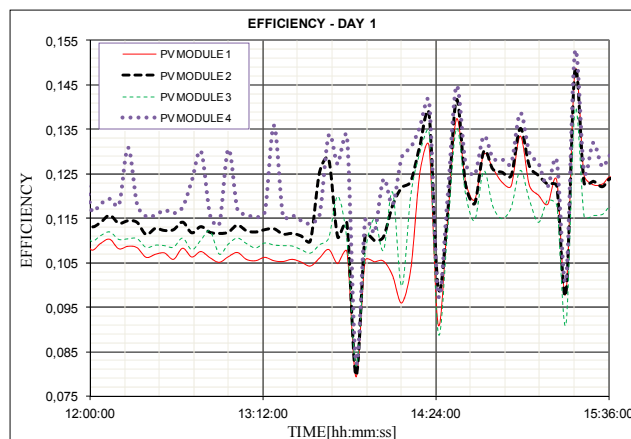


Figure 13. Efficiencies at slope  $60^\circ$

## 5. Conclusion

This paper presents the results of the analysis of characteristics of four photovoltaic modules. The energy yield is directly calculated from meteorological and geographical data with knowing PV module performance and losses in the system.

The exact value of the future annual energy yield cannot be determined because of two factors. Firstly, the equation that can predict weather in the future reliably doesn't exist. It can only be calculated on a base of long-term averages, minimums and maximums. Secondly, some losses also cannot be exactly calculated and have to be chosen on the basis of experience and recommendations. For a more accurate calculation of the energy yield, the PV module characteristics of particular module have to be known.

## References

- [1] Seme, S., Štumberger, G., Voršič, J.: *The optimal tracking strategies for two-axis PV system*, Prz. Elektrotech., (2011).
- [2] Goswami, D. Y., Kreith, F., Kreider, J. F.: *Principles of Solar Engineering*, Taylor & Francis, (2000).
- [3] Seme, S., Štumberger, G., Voršič, J.: *Maximum efficiency trajectories of a two-axis sun tracking system determined considering tracking system consumption*, IEEE Trans. Power Electron., (2011).
- [4] Dobovičnik, Z.: *Technical documentation of instrument MSPV01*, Velenje, (2011).



# Evaluation of Mechanical Properties of Soft Magnetic Materials for Axial Flux Permanent Magnet Synchronous Machines

Z. Praunseis, P. Vrtič

University of Maribor, Faculty of Energy Technology,  
Hočevarjev trg 1, 8270 Krško, Slovenia,  
e-mail: zdravko.praunseis@uni-mb.si, peter.vrtic@uni-mb.si

**Abstract.** Accurate determination of soft magnetic material mechanical properties is important for operation of axial flux permanent magnet synchronous machines (AFPMSM). The aim of the paper is systematic experimental approach for determination of mechanical properties of high strength low alloyed steels and mild carbon steel in the direction of steel rolling, steel plate thickness and width. These steels can be used as a rotor yoke in AFPMSM with coreless stator and double external rotor.

**Keywords:** *soft magnetic materials, mechanical properties, experimental testing.*

## 1. Introduction

The high strength low alloyed steels (HSLA) grade HT50 and HT80 is widely used for construction of different modern energy components [1]. The mild steel is typically carbon steel, with a comparatively mild amount of carbon (0.16% to 0.3%) and with ferromagnetic properties. Ferromagnetic properties make it ideal for electrical machines and other electrical devices [2, 3]. Due to the non-laminated rotor discs the mild steel is especially applicable to axial flux permanent magnet synchronous machines (AFPMSM) with coreless stator and double external rotor. Mild steel with high amount of carbon is vulnerable to rust. Where the rust free technology is required the stainless steel over mild steel is preferred. On the other hand, stainless steel does not have ferromagnetic properties although it is composed mainly of ferromagnetic metal. Mild steel is also used in construction as structural steel. It is also widely used in the car manufacturing and energy industry.

Three different types of steels were tested due to comparison of mutual mechanical properties. The mechanical properties of the HSLA steel grade HT50 and HT80 and mild steel were evaluated using standard tensile [4], Charpy [5] and Crack Tip Opening Displacement (CTOD) test [6, 7]. The samples were taken from the steel plates in rolling, thickness and width direction.

The differences in microstructures among material regions influence on the mechanical properties [8-13]. Thus, systematic experimental determination of material

mechanical properties including fractographical and metallographical investigation of fracture surfaces is necessary.

## 2. Experimental procedure

Chemical composition of the HSLA steel grade HT50 and HT80 and mild steel, plate thickness of 40 mm are given in Table 1. All testing samples were taken from the steel plates in rolling direction (A), thickness direction (B) and width direction (C).

The yield strength and tensile strength were obtained using round bar tensile samples, as shown in Fig. 1. Tensile testing was carried out at the room temperature (20 °C).

Charpy – V testing was used to determine the impact toughness of steel plates. Shape and dimensions of standard Charpy – V sample, mechanically notched, are shown in Fig. 2. Testing was performed at the temperature –10 °C. For every test temperature three samples were fractured.

Table 1. Chemical composition of the HSLA steel grade HT50 and HT80 and mild steel

Composition (%)	HT50	HT80	Mild steel
C	0.12	0.16	0.28
Si	0.55	0.68	0.52
Mn	0.67	0.75	0.71
P	0.015	0.020	0.011
S	0.002	0.003	0.007
Cr	0.70	0.79	0.05
Ni	0.07	0.09	0.01
Mo	0.042	0.032 <td>0.013</td>	0.013
Cu	0.19	0.24	0.62
Al	0.001	0.002	0.001

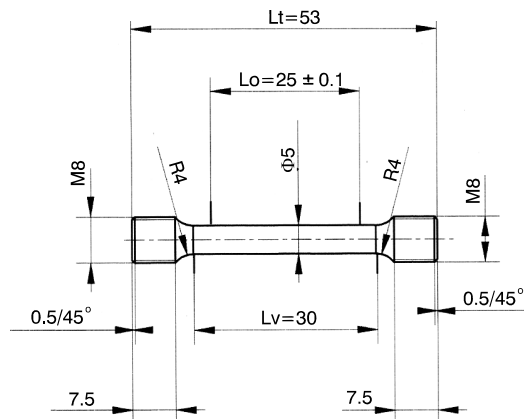


Figure 1. Round bar tensile sample B 5×25

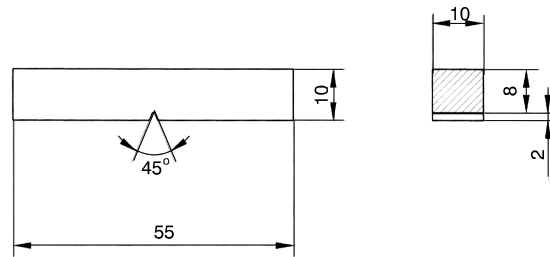


Figure 2. Shape and dimensions of V notched sample – Charpy

CTOD fracture toughness of the HSLA steel grade HT50 and HT80 and mild steel was evaluated using the standard static CTOD test [4-5]. Sample loading was carried out with constant crosshead speed  $v = 0.5$  mm/min. The test temperature was  $-10^{\circ}$  C according to the recommendation of the Offshore Mechanics and Arctic Engineering (OMAE) association. For CTOD testing the single sample method was used [1]. To evaluate fracture toughness of steels standard fracture mechanics tensile samples with shallow notches were used, as shown in Fig. 3.

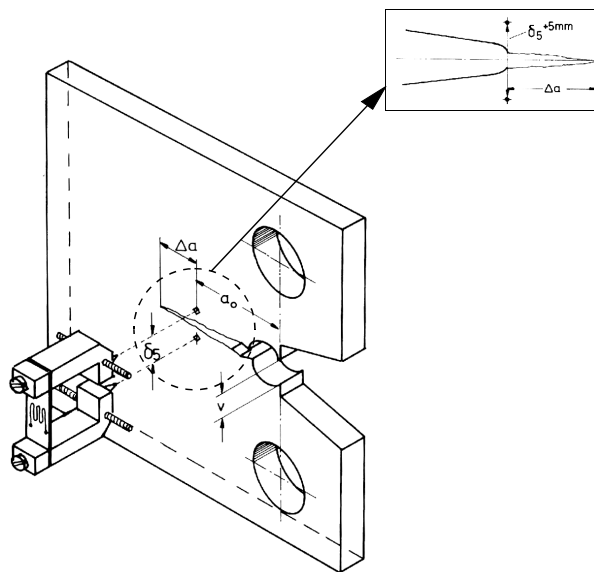


Figure 3. Direct measurement of CTOD values at crack tip of fracture mechanics sample

For all samples the fatigue precracking was carried out with the Step-Wise High R ratio (SHR) method procedure [6]. During the CTOD tests the potential drop technique was used for monitoring stable crack growth [7]. The CTOD test values were directly measured by special clip gauge [7] on the sample side surfaces at the fatigue crack tip over a gauge length of 5 mm (see Fig.3).

The basic aim of the fractographical investigation was to determine the location of brittle fracture initiation on the fracture surface of CTOD test samples and to identify

the brittle fracture initiation point by using Energy Disperse X-ray (EDX) analysis. Microstructure at the brittle fracture initiation point and around it, as well as crack path deviation nature, was evaluated using the fracture surface cross-section method [1] through the brittle fracture initiation point. A detailed analysis of material at the crack tip region and along deviated crack path was done by optical microscope and scanning electron microscope. This way the critical microstructure (local brittle zones) at fatigue crack tip surroundings, where the brittle fracture was initiated, and the microstructure, where it propagated later, were identified. For fractographical and metallographical analysis the most representative fractures of CTOD test samples were chosen, which also appeared in other samples in an appropriate shape.

### 3. Discussion of results

Mechanical properties of HSLA steel HT80 and HT50 and mild steel plate in the rolling direction (A), thickness direction (B) and width direction (C) are presented in Table 2. The basic values of yield strength and tensile strength of testing steels, given in Table 2, were obtained from engineering stress (R) – strain (e) diagrams. It is known that engineering material curves can not be used for the analysis of material deformation characteristics and finite element calculations in the range of high plastic deformations.

For this purpose the true stress – strain curve (Fig. 4) was used, which is described by the power law expression [4, 6]:

$$\sigma = \sigma_0 e^n \quad (1)$$

where:  $\sigma_0$  – fictitious yield strength,  $n$  – strain hardening exponent.

$$n = \frac{\log \frac{R_m (1 + A_{gt})}{R_{p0.2}}}{\log \frac{\ln(1 + A_{gt})}{e_{0.2}}} \quad (2)$$

where:  $R_m$  – ultimate tensile strength,  $A_{gt}$  – engineering extension at the maximum tensile load,  $R_{p0.2}$  – yield strength equivalent to 0.2 percent of proof stress,  $e_{0.2}$  – engineering extension.

$$e_{0.2} = \frac{R_{p0.2}}{E} + 0.002 \quad (3)$$

where:  $E$  – Young's modul.

Finally, the fictitious yield strength  $\sigma_0$  was calculated by:

$$\sigma_0 = R_{p0.2} 10^{\frac{n}{n-1} \log \frac{E e_{0.2}}{R_{p0.2}}} \quad (4)$$

Average Charpy-V testing results of three fractured samples are represented in Table 2, where abbreviation „av” means „average”.

Table 2. Mechanical properties of HSLA steel HT80 and HT50 and mild steel plate in the rolling direction (A), thickness direction (B) and width direction (C)

Steel grade	Measured direction	Yield strength (MPa)	Tensile strength (MPa)	CTOD (mm)	Charpy-V (J) at $-10^{\circ}\text{C}$
HT50	A	542	591	0.390	47, 68, 71 av = 62
HT80	A	693	830	0.401	69, 78, 64 av = 70
Mild steel	A	452	497	0.423	42, 55, 62 av = 53
HT50	B	501	562	0.240	39, 41, 55 av = 45
HT80	B	657	799	0.253	53, 68, 66 av = 62
Mild steel	B	439	471	0.231	39, 44, 61 av = 48
HT50	C	531	587	0.416	42, 76, 69 av = 62
HT80	C	665	811	0.478	67, 71, 63 av = 67
Mild steel	C	447	478	0.443	40, 51, 65 av = 52

The Charpy toughness of samples taken from the steel plates in rolling direction (A) is approximately equal to the Charpy toughness of samples taken from the steel plates in width direction (C).

The lowest Charpy toughness was measured in the samples taken from the steel plates in thickness direction (B). The cause for low toughness was appearance of inconvenient ferritic microstructure with distributed brittle martensite – avstenite (M-A) constituents (Fig. 5).

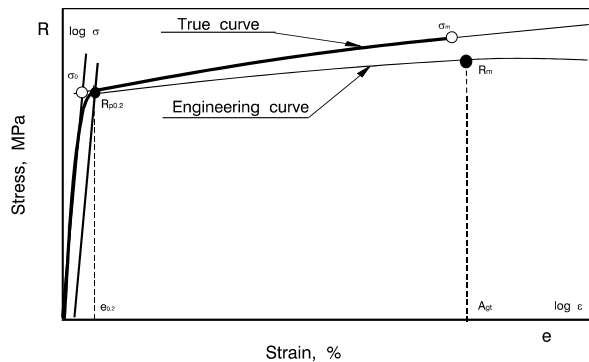


Figure 4. Engineering and true stress – strain curves for uniaxial tension

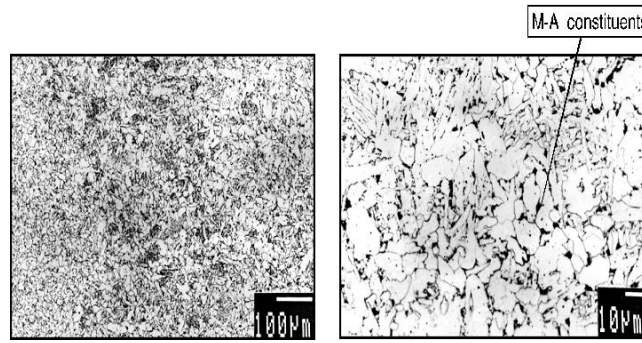


Figure 5. Ferritic microstructure with distributed brittle M-A constituents along ferrite grain boundaries

The Charpy toughness of samples taken from the steel plates in rolling direction (A) is approximately equal to the Charpy toughness of samples taken from the steel plates in width direction (C).

Directly measured CTOD test values of fracture toughness for each type of steels are summarized in Table 2. During CTOD testing of fracture mechanics samples the appearance of pop-ins at the propagating crack tip was expected. These moments are detected by force – displacement relationship (Fig. 6), which are evaluated according to the standard [6] depending on their size (decrease of force and sudden increase of displacement). The maximal CTOD toughness was measured in the samples with the crack tip located in the width direction (C).

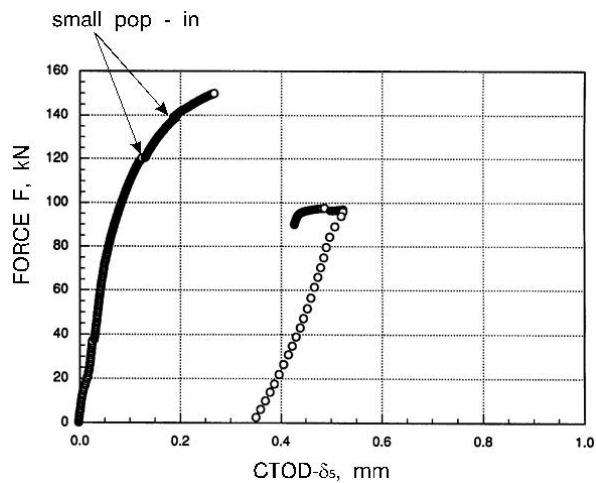


Figure 6. Appearance of local brittle zones during CTOD testing and final fracture of fracture mechanics specimen

In the case of CTOD testing of specimens with the crack tip located in the thickness direction (B) the lowest CTOD test value was measured due to the appearance of the first brittle fracture in the mainly ferritic microstructure with carbides ( $\text{Fe}_3\text{C}$ ),

precipitated at the grain boundary (Fig. 7 and Fig. 9) and appearance of brittle fracture initiation point, i.e. Al-Si-Mn inclusions (Fig. 8).

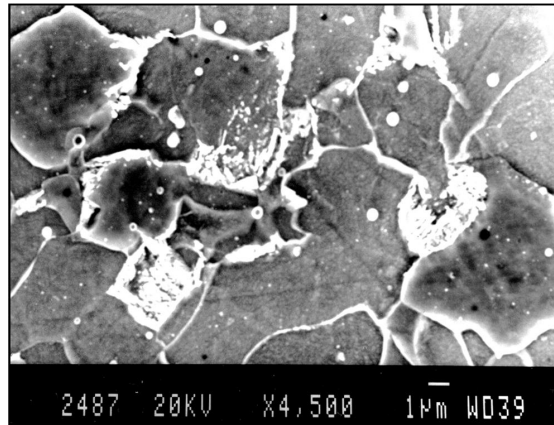


Figure 7. Mainly ferritic microstructure with carbides ( $Fe_3C$ ) precipitated at the grain boundary

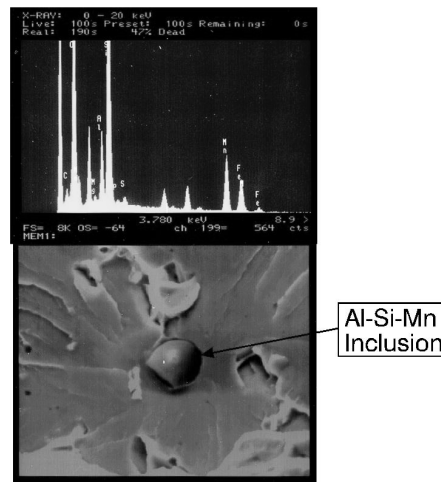


Figure 8. Appearance and EDX analysis of brittle fracture initiation point, i.e. Al-Si-Mn inclusion

It should be noticed that for correct identification of brittle fracture initiation point it is of utmost importance to apply EDX analysis to both fracture surfaces. In the opposite case it could happen that the EDX analysis detects fictitious brittle fracture initiation point.

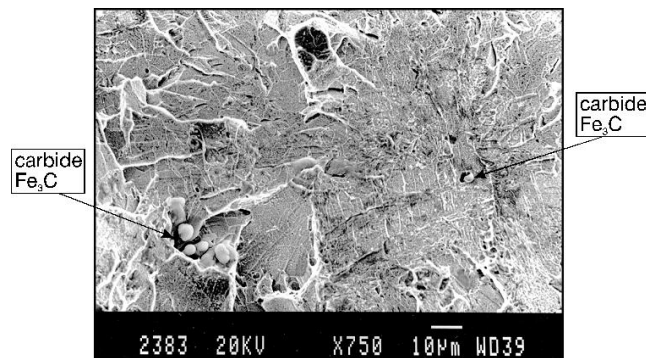


Figure 9. Identification of brittle fracture initiation point as  $Fe_3C$  on the fracture surface of CTOD test sample

#### 4. Conclusion

Due to the use of soft magnetic material for the rotor yoke in AFPMSM with coreless stator and double external rotor the exact evaluation of soft magnetic material mechanical properties is important for safe operation of AFPMSM.

The presence of different microstructures along pre-crack fatigue fronts has important effects on the critical CTOD. This value is relevant parameter not only for the rotor discs of AFPMSM but also for a variety of components in modern energy technology.

The mechanical properties of HSLA steels grade HT50 and HT80 and mild steel are the lowest in the thickness direction of the steel plate due to the appearance of carbides ( $Fe_3C$ ) and Al-Si-Mn inclusions in the ferritic microstructure. The mechanical properties of HSLA steels grade HT50 and HT80 and mild steel are approximately equal in rolling and in width direction of the steel plates.

#### Acknowledgments

The authors wish to acknowledge the financial support of the Slovenian Foundation of Science and Technology and the Japanese Promotion of Science

#### References

- [1] Praunseis, Z.: *The influence of Strength Under-matched Metals containing Heterogeneous Regions on Fracture Properties of HSLA Steel* (Dissertation in English), Faculty of Mechanical Engineering, University of Maribor, Slovenia, (1998).
- [2] Virtic, P.: *Variations of Permanent Magnets Dimensions in Axial Flux Permanent Magnet Synchronous Machine*, Prz. Elektrotech., 87, no. 12B, (2011), pp. 194–197.
- [3] Pisek, P., Virtic, P., Štumberger, B.: *Back EMF and torque characteristic of N-N and N-S type of multi-disc axial flux permanent magnet synchronous generator*, Prz. Elektrotech., 84, no. 12, (2008), pp. 221–223.



- [4] BS 4732, Methods for tensile testing, The British Standards Institution, London, (1979).
- [5] ASTM E 1152-87, Standard test method for Charpy testing, Annual Book of ASTM Standards, American Society for Testing and Materials, Philadelphia, (1990).
- [6] ASTM E 1290-91, Standard test method for crack-tip opening displacement (CTOD) fracture toughness measurement, American Society for Testing and Materials, Philadelphia, (1991).
- [7] GKSS Forschungszentrum Geesthacht GMBH, GKSS-Displacement Gauge Systems for Applications in Fracture Mechanic
- [8] Praunseis, Z., Toyoda, M., Sundararajan, T.: *Fracture behaviours of fracture toughness testing specimens with metallurgical heterogeneity along crack front*, 71, No. 9, (2000).
- [9] Praunseis, Z., Sundararajan, T., Toyoda, M., Ohata, M.: *The influence of soft root on fracture behaviors of high-strength, low-alloyed (HSLA) steel weldments*, Mater. manuf. process, 16, No. 2, (2001).
- [10] Sundararajan, T., Praunseis, Z.: *The effect of nitrogen-ion implantation on the corrosion resistance of titanium in comparison with oxygen- and argon-ion implantations*, Mater. Tehnol., 38, No. 1/2, (2004).
- [11] Praunseis, Z.: *Crack driving force of specimens with shallow crack in the undermatched welded joint*, Kovové mater., 38, No. 4, (2000), pp. 280–294.
- [12] Praunseis, Z., Toyoda, M.: *The transferability of fracture-mechanics parameters to fracture performance evaluation of welds with mismatching*, Mater. tehnol., 34, No. 6, (2000), pp. 343–352.
- [13] Praunseis, Z., Toyoda, M.: *Fracture toughness evaluation of mis-matched weld joints*, Weld. world, 45, special issue, (2001), pp. 195–199.

# Diagnostic of Broken Rotor Bars in Induction Motor on the Basis of its Magnetic Field Analysis

M. Zagirnyak, Z. Romashihina, A. Kalinov

Kremenchuk Mykhailo Ostrohradskyi National University  
Institute Of Electromechanics, Energysaving And Control Systems,  
Pershotravneva, 20, 39600, Kremenchuk, Ukraine,  
e-mail: mzagirn@kdu.edu.ua, romashihina\_zhanna@mail.ru,  
scenter@kdu.edu.ua.

**Abstract.** The analysis of magnetic field in an induction motor operating gap in the presence of rotor bar damages after disconnecting the motor from the supply mains is carried out using the finite elements method. The performed wavelet analysis of the stator winding electromotive force signal, calculated due to modeling, makes it possible to determine the location of the rotor broken bars. The experimental research confirming the efficiency of the offered method of rotor broken bar diagnostics based on magnetic field analysis is performed.

**Keywords:** *motor, rotor broken bars, disconnecting the motor, electromotive force.*

## 1. Introduction

Squirrel-cage rotor induction motors (IM) are the most common type of electric machines (EM). Annually about 20-25% of the total amount of IM break down. Statistics show that about 5% of IM failures are due to rotor broken bar.

There exist various methods for IM rotor damages diagnostics [1]. Most of them require elimination of the workflow and disassembling the motor. Conventional methods of IM damages diagnostics in operation, e.g. Motor Current Signature Analysis (MCSA), do not take into account the influence of the mains supply on the diagnostics results. In this case MCSA method does not provide satisfactory results when diagnostics is made under no-load conditions. Besides, use of the results of fast Fourier transformation of current signals does not enable unambiguous determination of breakage level and rotor broken bars relative position. So, it is topical to develop methods due to which it would be possible to determine the degree of damage and location of broken bars without elimination of the technological process.

During the recent decade numerical methods of research have been actively used in the sphere of IM diagnostics [2-3].

As it is known, the EM mathematical modeling with application of the classical field theory makes it possible to analyze their characteristics, using the simplified circuit model analysis.

Numerical methods of the electromagnetic field analysis enable research of both steady and dynamic conditions of EM operation. Finite element method (FEM) is one of the most widely-used numerical methods of IM field analysis.

In this case the analysis of steady conditions of EM operation is to be made according to the results of calculation of their electromagnetic field. The analysis of transient and dynamic conditions is carried out with the use of circuit-field mathematical models (CFMM). They are based on the joint solution of winding electric circuit differential equations and equations of nonstational electromagnetic field in EM active zone [4].

Rotor broken bar are known to result in distortion of magnetic field in the IM air-gap. Presence of IM stator and rotor slots causes occurrence of tooth space harmonics of this field. Tooth kink makes it possible to correlate flux lines with teeth geometrical layout.

Paper [5] deals with the diagnostics of rotor broken bars by the analysis of the processes in an induction motor after its switching-off. The use of IM switching-off provides the possibility to avoid the influence of low-quality mains supply on the diagnostics results. When the motor is disconnected from the mains, electromotive force (EMF) is induced in stator windings, which is conditioned by currents attenuation in the rotating rotor windings. Magnetic field distortions caused by rotor broken bars are fixed according to the analysis of EMF instantaneous values in stator windings.

When an experimental investigation is made, magnetic field distortions can be caused not only by rotor broken bars but also by a number of other factors: rotor static and dynamic imbalance, magnetic system unsymmetry, etc. That is why a mathematical model based on FEM was proposed for estimation of the rotor broken bars influence on IM magnetic field [2-3].

## 2. The purpose of the paper

The calculation of induction motor magnetic field, using the finite elements method, and its results analysis for the diagnostics of rotor broken bars according to the signal of stator winding electromotive force after disconnecting the motor from the supply mains.

### 2.1. Basic theory

To calculate EMF in IM stator windings [4] the flux linkage of these windings is used.

Relation between magnetic induction  $\vec{B}$  and vector magnetic potential (VMP)  $\vec{A}$  according to Maxwell equation:

$$\vec{B} = \text{rot } \vec{A} \quad (1)$$

To calculate stator windings EMF the total flux linkage of a winding phase is used:

$$\Psi_{ph} = \frac{2I_s \omega_s}{S_{sl}} \int_{S_{ph}} A_z dS \quad (2)$$

where  $l_s$  – stator active length;  $\omega_s$  – the number of turns connected in series in the slot;  $S_{sl}$  – stator slot section area;  $A_{z\Sigma}$  – total accumulative value of VMP in all the phase slots;  $S_{ph}$  – total cross-sectional area of all the phase coils connected in series.

Flux linkage values are used for determination of the stator winding phase EMF according to Faraday's law of electromagnetic induction:

$$e_s(t) = -\frac{d\Psi_s}{dt} \quad (3)$$

When stator winding EMF is calculated in an IM after its switching-off, the character of currents attenuation in rotor bars is taken into account. At the moment of switching the motor off the mains supply ( $t = 0$ ) the currents in stator phases are equal to zero. In this case the principle of flux linkage constancy is observed. The rotor current at the moment of switching the IM off the mains supply is determined by expression [6]:

$$I_{2beg} = I_{2(t=0)} + k_2 I_{1(t=0)} \quad (4)$$

where  $I_{2(t=0)}$  – rotor current in the previous steady condition at the moment of switching the IM off the mains supply;  $k_2$  – rotor coupling coefficient [6];  $I_{1(t=0)}$  – stator current in the previous steady condition at the moment of switching the IM off the mains supply.

At the following time moments the rotor bars currents attenuate exponentially with the time constant:

$$\tau = L_2 / R_2 \quad (5)$$

where  $L_2$  – rotor induction,  $R_2$  – rotor active resistance.

## 2.2. Numerical modeling

IM of AHP80B4Y2 type is selected for the research ( $P=1.5$  kW,  $n=1395$  rpm,  $\eta=0.77$ ,  $\cos\varphi=0.81$ ). Magnetic field numerical computation is based on developed IM model taking into consideration the machine geometry, magnetic and electrical properties of its active materials.

The design of IM manufactured from real materials has some peculiarities: geometry nonsymmetry, irregularity of properties (deviation of their magnetic and electrical characteristics from steady values), etc. That is why during the modeling the main assumptions determining the level of idealization of physical and geometric features of the construction are taken into account.

Surface effect in two-dimensional formulation of solution of the problem of magnetic field in cross-section is considered by introducing boundary conditions. The slant of rotor slots is not taken into account. Bar break is considered to be the total loss of the contact with rotor cage ring.

The computation of magnetic field in the IM cross-section is made by software [7], which makes it possible to solve both linear and nonlinear problems.

The computation by FEM consists of the following stages:

1. Development of the model geometry.
2. Selection of elements types, introduction of material features, assignment of material and element features to geometric areas.
3. Assumption of current initial values in rotor bars.
4. Assumption of boundary conditions. Dirichlet condition is used for the external boundary of the model. In this case VMP is assumed to be equal to zero ( $A = 0$ ). Zero Dirichlet condition determines the behaviour of induction normal component on the boundary of model.
5. Discretization of the model areas into the finite-element mesh.
6. Numerical solution of the equations system.

To build EMF curve the computation of IM magnetic field for two complete revolutions of rotor with the turn step of 1 degree was made. In this case the decrease of rotor speed after disconnecting the motor from the supply mains is taken into consideration.

Computation of IM magnetic field is made in batch with the use of LUA-script. Command set for LUA-script can be changed in accordance with the problems posed by the computation. The obtained model can be used for research of IM of any required H.P. and different dynamic operation conditions determined only by initial values of currents in the stator and rotor slots.

To determine the currents in rotor bar at the moment of motor disconnection from the supply mains the IM circuit model in a three-phase coordinate system is developed. The created model is based on the use of balance equations of IM stator and rotor circuit voltage [8]. In this model the number of rotor electric circuits corresponds to the number of bars.

The developed mathematic circuit model makes it possible to research operation conditions of IM with different number of broken bars taking the damage geometrical layout into account.

The results of modeling enabled getting the values of currents in rotor bars at the initial moment of IM disconnection from the supply mains. These values were used in FEM calculation of IM magnetic field in the switching-off conditions.

Calculation of magnetic field after IM disconnection from the supply mains resulted in obtaining the flux lines distribution in a healthy motor (Fig. 1, a) and in the one with rotor bar damages (Fig. 1, b).

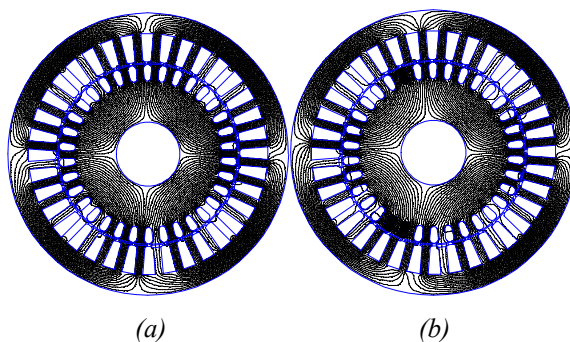


Figure 1. Flux lines at a healthy IM (a) and IM with three broken rotor bars (b)

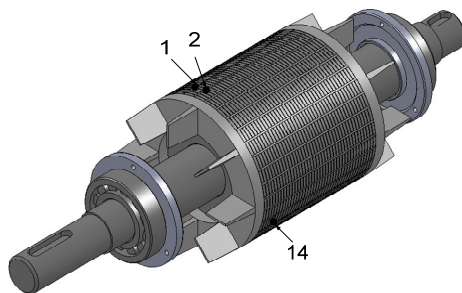


Figure 2. Location of broken IM rotor bars

In Fig. 1, b the broken bars are marked with black color. The numbers and location of broken bars are selected in accordance with the physically investigated IM with artificially made rotor damages. Breaking-down of bars electrical coupling is made by drilling holes in the rotor (they are designated as 1, 2 and 14 in Fig. 2).

As modeling results show, in a healthy motor the symmetric distribution of magnetic field lines is observed. In the presence of broken rotor bars the IM magnetic field becomes asymmetric.

To determine the diagnostic criteria the analysis of IM magnetic field distribution in dynamic mode is made. To assess the distortion of the magnetic field the stator winding electromotive force (EMF) signal calculated according to expression (3) for two complete rotor revolutions after IM disconnection from the supply mains is used.

In Fig. 3 the calculation values of EMF signals in healthy IM stator windings, and also in the motor with one and three broken bars respectively, are depicted.

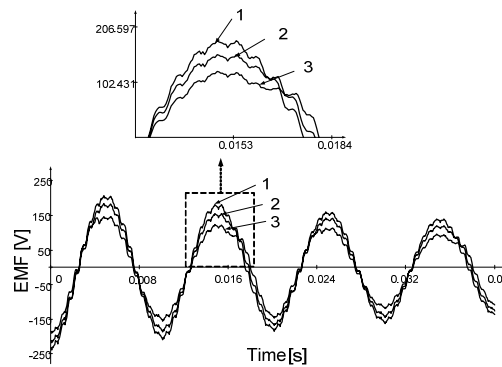


Figure 3. EMF signals in the stator windings: 1 – healthy IM, 2 – IM with of one broken rotor bar, 3 – IM with of three broken rotor bars

As the results of calculation of stator windings EMF show, EMF amplitude decreases because of the increase of the rotor cage equivalent resistance. With the increase of broken bars number some distortions can be seen in the EMF signal. It is proposed to use the wavelet analysis to assess these distortions [9].

Wavelet transform is the generalization of spectral analysis, but due to the possibility of making the analysis both in the frequency and time domain, it allows analyzing and processing the signals and functions, that are non-stationary in time and inhomogeneous in space.

Research as to the choice of wavelet-functions for wavelet transform of the calculated EMF signal in the stator windings was made. During the research it was determined that orthogonal wavelets with compact support can be used for analysis of sinusoid-like waveforms. Such wavelets include the wavelets of Daubechies, Symlet and Coiflets [9].

As the research results show, only the decaying character of signal is reflected on low frequencies in spectrum. To determine the local peculiarities of the stator winding EMF signal the wavelet-analysis by the tertiary wavelet of Symlet is made. In Fig. 4 the results of wavelet transform of EMF in stator windings of the healthy IM and IM with of one and three broken rotor bars, respectively, are depicted.

In the wavelet spectrum of EMF signal (Fig. 4, a) in the high-frequency range the tooth kinks, number of which correlates to real number of rotor bars, are shown. Wavelet spectrum analysis in Fig. 4, b and 4, c shows that explicit coefficients of wavelet decomposition, marked with dotted line, correspond to broken bars.

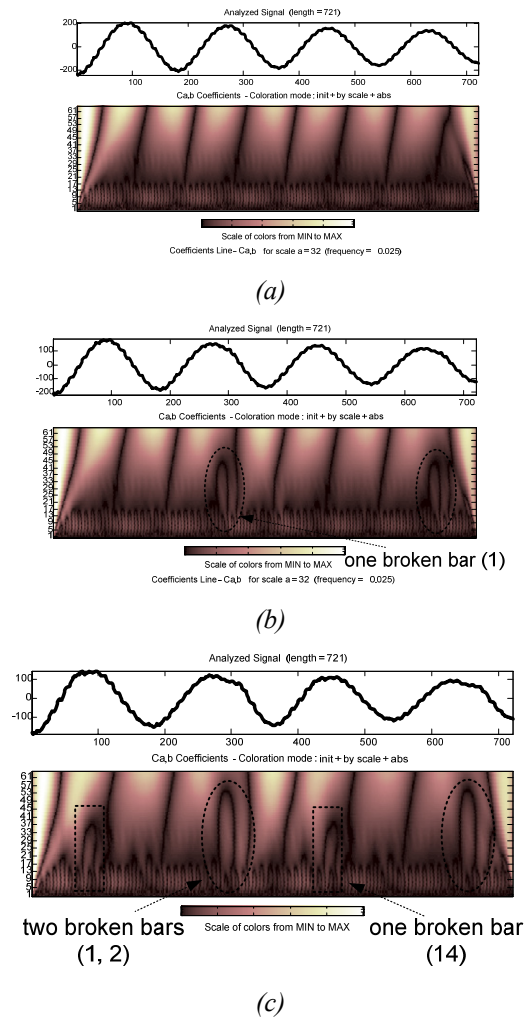
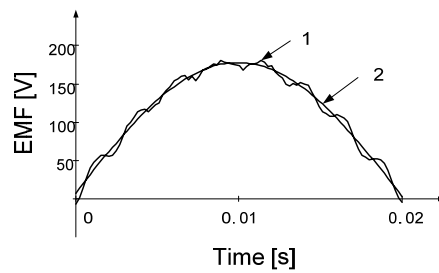


Figure 4. EMF signals in the stator windings and their wavelet spectrums for healthy IM (a) and IM with one (b) or three (c) broken rotor bars

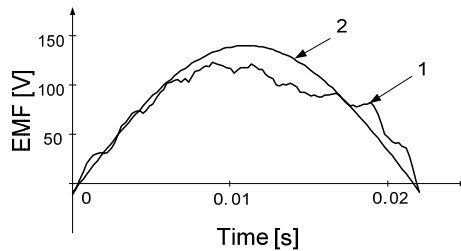
To assess the influence of broken rotor bars the comparison of calculated and approximated EMF signals half-periods in the stator windings of healthy IM and in the IM with damages is made (Fig. 5).

The comparison results show that in healthy IM the EMF in the stator windings has the form of a regular sinusoid modulated by high-frequency oscillations caused by IM toothed form. In case of damages there is evident deviation of the EMF signal form from the sinusoidal one (Fig. 6).





(a)



(b)

Figure 5. Patterns of calculated (1) and approximated (2) EMF signals in the stator windings of healthy IM (a) and IM with three broken rotor bars (b)

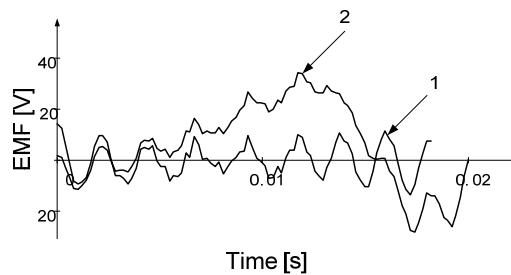


Figure 6. Difference between approximated and calculated EMF signals in the stator windings: 1 – for healthy IM, 2 – for IM with three broken rotor bars

Thus, IM rotor bar breaks diagnostics using EMF signal wavelet transform in stator windings after switching IM off the mains makes it possible to determine the relative position of broken bars.

Besides, rotor bar breaks diagnostics can also be made according to the results of the analysis of difference between approximated and calculated EMF signals.

**2.3. Experimental research**

To confirm the results of modeling of IM magnetic field, considering the broken rotor bars, the experimental research with the use of the developed computerized measuring complex was made (Fig. 7).

It consists of voltage and current sensors set, an analog-digital converter and a personal computer for the results analysis.

Experimental research was made for healthy IM and IM with one, two or three broken rotor bars. Layout chart of broken bars is shown in Fig. 2. During the experiment IM was switched off the mains; stator phase voltages were measured by sensor set. The analysis of the obtained results is demonstrated in Fig. 9.

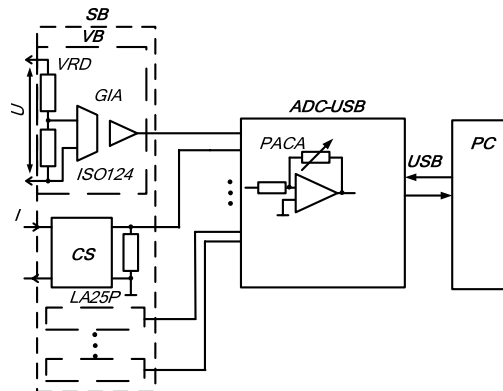


Figure 7. Measuring module functional circuit (SB – sensor block; VB – voltage block; VRD – voltage resistance divider; GIA – galvanic isolation amplifier; CS – current sensor; PC – personal computer; PACA – programmed amplification coefficient amplifier; USB – PC bus

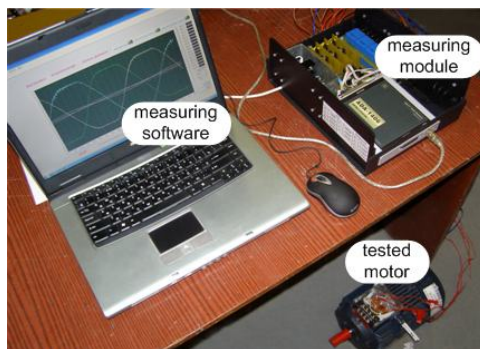


Figure 8. Photo of the measuring complex

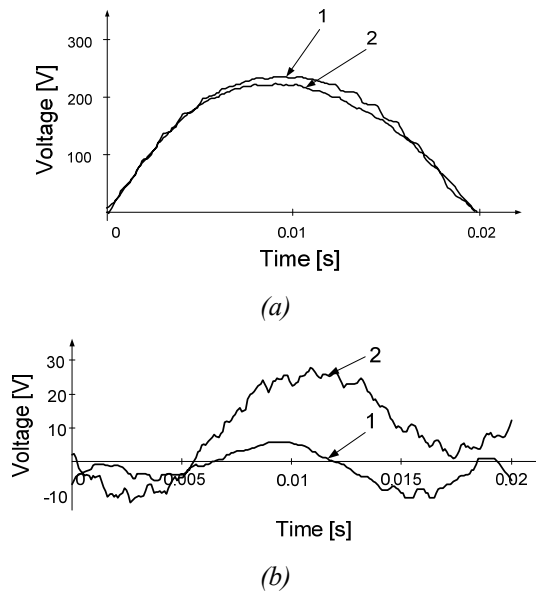


Figure 9. Voltage (a) and difference between approximated and experimental signals of voltage (b) in the stator phase: 1 – for healthy IM, 2 – for IM with three broken rotor bars

Results of comparison of EMF in the stator phase for healthy IM and with broken bars (Fig. 9, a, b) are confirmed by the distortion of EMF signal form in the presence of rotor damages. The values of the difference between the approximated and experimental voltage signals in stator phase can be used to determine the degree and location of rotor bar damages.

### 3. Conclusions

The offered methods of electromagnetic processes calculation with the use of IM circuit model and a mathematical model based on FEM makes it possible to assess rotor bar damages influence on the EMF signal of stator phase winding after switching IM off the mains. The use of wavelet transformation of stator winding EMF signal obtained on the basis of magnetic field calculation after switching IM off the mains allows determination of the rotor bar damages location. Experimental research, carried out on the developed computerized measuring complex, confirmed the efficiency of the proposed method for IM rotor bar damages diagnostics.

### References

- [1] Casimir, R., Boutleux, E., Clerc, G., Chappuis, F.: *Comparative Study of Diagnosis Methods for Induction Motor*, Proc. Int. Conf. Electr. Mach. Brugge, Belgium, (2002), pp. 465–470.

- [2] Yeh, C.C., Mirafzal, B., Povinelli, R. J., Demerdash, N. A. O.: *A Condition Monitoring Vector Database Approach for Broken Bar Fault Diagnostics of Induction Machines*, IEEE, 2005, pp. 29–34
- [3] Nemeč, M., Ambrožič, V., Fišer, R., Makuc, D.: *Parameters estimation using single phase measurement of three phase induction machine*, Przegląd Elektrotechniczny (Electrical Review), No. 3, (2011), pp. 129–132.
- [4] Vaskovskij, Y.: *Field Analysis of the Electrical Machines*, Tutorial, Kiev, (2007), [in Ukrainian].
- [5] Kalinov, A., Uchan, Zh., Urdin, I.: *Method of Diagnostics of Rotor Bars Damages*, Visnyk KDU, 57, No. 4, (2009), pp. 98–101, [in Ukrainian].
- [6] Ivanov-Smolensky, A.: *Electrical Machines*: – Moscow: MIR Publishers, (1983).
- [7] <http://www.femm.info/wiki/HomePage>.
- [8] Chornij, O., Lugovoj, A., Rodkin, D., Sisjuk, G., Sadovoj, O.: *Modeling of Electromechanical Systems*, Kremenčuk, (2001), [in Ukrainian].
- [9] Debnath, L.: *Wavelet Transforms and Time-Frequency Signal Analysis*, Birkhäuser Boston, (2001).

# Microwave-Induced Hearing – its Mechanism and Consequences

W. Stankiewicz, A. Krawczyk, J. Kieliszek

Department of Microwave Safety, Military Institute of Hygiene and Epidemiology, Kozielska 4, 01-163, Warsaw, Poland  
e-mail: wanda.stankiewicz@gmail.com, ankra.new@gmail.com, jarekkiel@wp.pl,

**Abstract.** This paper describes well-documented effect of electromagnetic field at high frequency, i.e. the auditory effect. The history of research in his area is described and some evidences are quoted. The contemporary interpretation of the microwave-induced hearing is discussed as well as new directions of research are drafted.

*Keywords:* electromagnetic field, auditory effect, thermoelastic expansion

## 1. History of research

The microwave auditory is one of two well-documented behavioural thermal effects connected with the electromagnetic field of high frequency – the other one is the effect of heating of tissue. The history of investigations of microwave-induced (MW-induced) auditory effect started in 1947 – at that time the first finding on hearing of repetitive sounds from radars occurred, but was treated as the mental problems rather [1]. There was a common opinion that “hearing” of electromagnetic field is not possible – the paradigm existing in hearing was the pressure of acoustic waves. It caused that the real investigation in this area started later as the next publication came in 1961 and was prepared by Frey - that is why sometimes the electromagnetic hearing is called Frey’s phenomena [8]. He also observed the people exposed in radar beam and he found that the voices they heard were of buzz, hiss and clicking. The voices occurred not regarding what was the position of a man in referring to the radar antenna. Electromagnetic nature of the voices was confirmed by the fact that all these effects have been stopped when aluminium screen was installed. In this investigation the crucial part of brain responsible on the “electromagnetic sounds” the frontal lobe is supposed – when it was screened by metal plate of 5 cm×5 cm the voices disappeared. The side finding of the investigation was that the intensity of voices increased when the people were provided with “anti-noise” apparatus what limited the level of environmental noise.

## 2. Mechanism of MW-induced auditory effect and consequences

The investigations carried out within last, say 10-15 years, indicated that threshold values depend on numerous parameters, like frequency, pulsation rhythm, pulse time, density of energy emitted within the pulse and averaged energy. The various combinations of the parameters decided on the results. The so called heariness exists in

the frequency spectrum, from 2.4 till 10000 MHz. But the level of heariness depends also on the special arrangement of parameters, for example there was the lack of heariness for the WMF frequency 8900 MHz and the density of power  $0.0025 \text{ W/m}^2$ , and for frequency 216 MHz the threshold of "hearness" was  $40 \text{ W/m}^2$  [7]. Guy and co-workers [13] showed that the threshold at 2450 MHz was reached for density of energy  $0.40 \text{ J/m}^2$  in one pulse, independently of the fact what was the maximum energy or length of pulse (less than  $32 \mu\text{s}$ ). It resulted from the simulation that each pulse of these energy parameters could cause the temperature increase of ca.  $5 \times 10^{-6} \text{ }^\circ\text{C}$ .

The investigations indicated that MW hearing can be experienced by the people whose auditory diagram is between 5 and 10 kHz. It should be noticed that in this case the bone conduction played the important role ([5], [22]).

The acoustic waves are absorbed by an ear and interpreted as the sound by the brain centres. At the first stage a mechanical distortion is sent further as the electric potential which represents the acoustic wave. These potentials can be measured by the use of electrodes places in the vicinity of neuronal acoustic paths.

It is known that acoustic stimuli generate, the so called evoked potentials in CNS (central nervous system) beyond the acoustic paths. Examinations of MW EMF perception ([4], [16], [17]) on the basis of electrophysiological phenomena in auditory paths and measuring evoked potential show the similarity between auditory path and trace of EMF stimuli which are transvered on the cochlear level to electrophysiological auditory path. One has to regard that to hear MW-induced sounds one has to be exposed to EMF in the frequency range of megahertz while the range of frequency of acoustic wave should exceed 5 kHz.

It is well-known (e.g.: [7]) that the MW-induced hearing does not come from the direct interaction between electromagnetic field and the auditory nerves or the part of CNS. The microwave pulse which is absorbed by soft tissues in the head, causes a thermoelastic wave of acoustic pressure that is transmitted by bone conduction to the inner ear where the cochlear receptors are activated. The mechanisms of microwave hearing is finally the same as for normal hearing.

This phenomenon is known as the theory of thermoelastic expansion.

To recognize the consequences of the MW-induced hearing one should put two questions:

- What the physiological consequences are?
- What are the psychological consequences (if any) of MW-induced auditory effect?

There is a common opinion that microwave hearing has no consequences on the human health, both from physiological and psychological aspects. It is supported by the following findings:

- the sounds generated indirectly by EMF do not differ from those existing in nature and the latter are much more intensive,

- although the additional hearing may be generate the stress, the small intensity of the MW-induced sounds can be easily eliminated by simple physical interventions, like being at distance with the EMF source or shielding.

But there are still some doubts and concerns connected with the health consequences of MW-induced hearing, so the problem is open for further interdisciplinary investigations.

The last decade brought also the research connected with the mobile phone influence on hearing [19]. The widespread use of mobile phones has caused rise of concern whether the electromagnetic field generated by mobile phones changes anything in the process of hearing. The examination was made with the cohort of 30 people (17 males and 13 females) of the age between 19 and 36 years. The monitoring of possible negative effect of mobile phones was realized by means of otoacoustic emission (OAE), utilizing the special cochlear emission analyser. After vast examination the final result can be formulated as follows:

Statistical analyses of the evoked OAE levels corroborate that mobile phones use does not cause any alter-effect on hearing in neither a positive nor a negative manner.

Dealing with the electromagnetic interferences with human organisms one tends to the positive aspects of the interferences as this is more promising for future. The same situation one meets with the problem of MW-induced hearing. There are also possibilities to use the auditory effect in the examinations of physiology and physiopathology of hearing organ, among others in the examination of otoacoustic emission and the harm of it by electromagnetic radiation. It was found that the hearing organ can either percept the sounds or generate them. The possibility of this phenomenon was signalized in 1946 by Thomas Gold (1920-2004) in the paper describing physical foundations of cochlear activation. Some 30 years later the Gold hypothesis has been confirmed by David Kemp. Sounds which are emitted by cochlear and registered in the outer ear by means of special apparatus are defined as acoustic ear emission. The factors influencing the middle ear, may be that EMF too, would decrease the energy of received signal, thus they would harm the otoacoustic emission. Therefore, the examination of otoacoustic emission can show the pathological processes in ear. The majority of researchers (see Arai and others, 2003) who attempt at determination of the EMF influence on hearing examine otoacoustic emission and evoked potentials in brain stem as well as their changes due to EMF emitted by mobile phones. The majority of researchers find these changes are of inhomogeneous character and do not link them with the possible EMF hazard. They are however of the same opinion as to the continuation of research and enlarging the number of patients and volunteers as well as differentiating possible exposures (character of exposure and intensity).

## References

- [1] Airborne Instruments Laboratory, *An observation on the detection by the ear microwave signals*, Proc IRE 44:2A, (1956).

- [2] Arai, N., Enomoto, H., Okabe, S.: *Thirty minutes mobile phone use has no short-term adverse effects on central auditory pathways*, Clin Neurophysiol 114., (2003), pp. 1390–1394.
- [3] Cain, C. A., Rissmann, W. J.: *Mammalian auditory response to 3.0 GHz microwave pulses*, IEEE Trans Biomed Eng BME 25, (1978), pp. 288–293.
- [4] Chou, C. K., Guy, A. W., Galambos, R.: *Microwave-induced auditory response: Cochlear microphonics*, In: Johnson C. C., Shore M. L., ed. Biological effects of electromagnetic waves. Vol. 1. Rockville, MD: HEV Publication (FDA) 77-8010., (1976), pp. 89–103.
- [5] Chou, C. K., Guy, A. W., Galambos, R.: *Characteristics of microwave-induced cochlear microphonics*, Radio Sci 12(6S): (1977), pp. 221–227.
- [6] Constant, P. C. Jr.: *Hearing EM waves*, In: Jacobson B. Ed. Digest of the Seventh International Conference on Medical and Biological Engineering. Stockholm, Sweden: Department Biological Engineering, Karolinska Institute. (1967).
- [7] Foster, K. R., Finch, E. D.: *Microwave hearing: Evidence for thermoacoustic auditory stimulation by pulsed microwaves*, Science 185, (1974), pp. 256–258.
- [8] Frey, A. H.: *Auditory system response to radio frequency energy*, Aerospace Med. 32: (1961), pp. 1140–1142.
- [9] Frey, A. H.: *Human auditory system response to modulated electromagnetic energy*, J Appl. Physiol. 17: (1962), pp. 689–692.
- [10] Frey, A. H.: *Some effects on human subjects of ultra-high-frequency radiation*, Am. J. Med. Electron 2, (1963), pp. 28–31.
- [11] Frey, A. H., Messenger, R.: *Human perception of illumination with pulsed ultrahigh-frequency electromagnetic energy*, Science 181, (1973), pp. 356–358.
- [12] Gournay, L. S.: *Conversion of electromagnetic to acoustic energy by surface heating*, J. Acous. Soc. Am. 40, (1966), pp. 1322–1330.
- [13] Guy, A. W., Chou, C. K., Lin, J. C., Christensen D.: *Microwave-induced acoustic effects in mammalian auditory systems and physical materials*, Ann. NY Acad. Sci. 247, (1975), pp. 194–215.
- [14] Ingalls, C. E.: *Sensation of hearing in electromagnetic fields*, NY State J. Med. 67, (1967), pp. 2992–2997.
- [15] Khizhnyak, E. P., Shorokkhov, V. V., Tyazhelov, V. V.: *Two types of microwave auditory sensation and their possible mechanism*, In: Berteaud A., Servantie B. Ed. Proceedings of the URSI Symposium, Ondes Electromagnetiques et Biologie (Electromagnetics Waves and Biology), Jouy en Josas, (1980), pp. 101–103.
- [16] Lin, J. C.: *Microwave-induced hearing: Some preliminary theoretical observations*, J Microwave Power 11, (1976), pp. 295–298.
- [17] Lin, J. C.: *On microwave-induced hearing sensation*, IEEE Trans Microwave Theory Tech. 25, (1977), pp. 605–613.
- [18] Lin, J. C.: *Hearing microwaves: the microwave auditory phenomenon*, IEEE Microwave Magazine 3, (2002), pp. 30–34.
- [19] Ozturan, O., et al.: *Effects of mobile telephone's electromagnetic field on hearing*, [www.otoemissions.org/whitepapers/clinical/mobile.html](http://www.otoemissions.org/whitepapers/clinical/mobile.html).
- [20] Rochmann, P.: *Human auditory system response to pulsed radiofrequency energy in RF coils for magnetic resonance at 2.4 to 179 MHz*, Magn. Reson. Med. 21, (1991), pp. 151–157.



- [21] Sommer, H. C., von Gierke, H. E.: *Hearing sensation in electric fields*, *Aerospace Med.* 35, (1964), pp. 834–839.
- [22] Watanabe, Y., Tanaka, T., Taki, M., Watanabe, S.: *FDTD analysis of microwave*, *Theory Tech*, 49, (2000), pp. 2126–2132.

# Eddy Currents in Permanent Magnets of a Multi-pole Direct Drive Motor

G. Gotovac<sup>1</sup>, G. Lampic<sup>1</sup>, D. Miljavec<sup>2</sup>

Elaphe Ltd.<sup>1</sup>, University of Ljubljana, Faculty of Electrical Engineering<sup>2</sup>

**Abstract.** Eddy currents in permanent magnets of direct drive synchronous motors cause permanent magnet heating which can cause a drop in performance, reduce durability or even cause machine failure. In this article eddy currents in permanent magnets of multi-pole direct drive motors with sinusoidal current are investigated with finite-element analysis with an emphasis on the dependency of losses on different design parameters. Analytical equations are used for comparison and evaluation of the possible replacement of the more time consuming numerical calculations.

**Keywords:** *eddy-current losses, permanent magnets, finite element method, direct drive motor*

## 1. Introduction

Direct drive motors are used in applications where high efficiency and reliability is needed. Their use has increased in recent years in propulsion systems for electric vehicles with an aim of mitigating the energy source problem and enabling new concepts like in-wheel drive. Since there is no mechanical gear between the motor and the wheel of the car, direct drive motors require a high rated torque. Permanent magnet synchronous motors with high pole numbers have a very favourable torque to weight ratio and good efficiency, which makes them a suitable candidate for a direct drive motor. However, these motors usually have slotted stators, which can, in connection with a high pole number, introduce high frequency components into both the air-gap permanent-magnet flux density as well as the air-gap stator-current magnetic flux. Furthermore, the windings of these motors have very low inductances which enable an increase of the current ripple and with this some additional high frequency harmonics in the air-gap magnetic flux. The high frequency magnetic field oscillation superimposed on the main rotational magnetic flux density causes eddy-current induction in permanent magnets, which can lead to performance decrease, additional losses and even to overheating and demagnetization of the magnets.

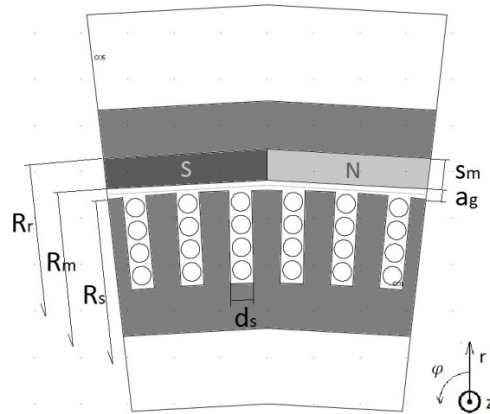


Figure 1. The geometry of one pole pair with two radially magnetised magnets

The effect of the stator geometry on the magnetic flux density harmonic content has been studied in [1, 2], where analytical models have been introduced to enable fast calculation of the induced eddy current density and the losses in the permanent magnets. In this article eddy currents in permanent magnets of multi-pole direct drive motors with sinusoidal current are investigated with finite-element analysis with an emphasis on the dependency of losses on different design parameters. As a support, analytical solution from literature [3, 4] will be calculated to evaluate whether it can be used instead of FEM analysis when fast results are needed.

## 2. Geometry and variables

The geometry of one pole pair and the motor parameters are presented in Fig. 1 and Table 1.

Table 1. Parameter description and values for original design

Label	Description	
$P_{rat}$	Rated power	28 kW
$P_r$	Rotor pole pairs	28
$P_s$	Stator pole pairs	28
$N_s$	Number of stator slots	168
$R_s$	Stator outer radius	162.0 mm
$R_m$	Magnet inner radius	163.0 mm
$R_r$	Magnet outer radius	166.45 mm
$a_g$	Air-gap length	1.0 mm
$s_m$	Magnet thickness	3.45 mm
$d_s$	Slot opening length	2.75 mm

Label	Description	
g	Slot depth	11.5 mm
l	Stator axial length	60 mm
$\omega$	Rotational angular frequency	100 s <sup>-1</sup>
$\nu_{\text{FWM}}$	PWM frequency	10 kHz
$\gamma$	Magnet electrical conductivity	6.7 10 <sup>5</sup> S m <sup>-1</sup>
$I_0$	Max. current amplitude	565 A
$I_{\text{FWM}}$	Max. current ripple amplitude	56.5 A

## Theory

The eddy-current losses are calculated by a time and space average of instantaneous losses via equation

$$\langle P_I \rangle = \frac{N_s \omega}{2\pi\gamma} \int_V \int_0^{2\pi} N_s \omega J_e(r, \varphi, t)^2 r dr d\varphi dt \quad (1)$$

In order to obtain a useful result, eddy-current distributions are needed for each underlying cause. The following assumptions have also been made:

- i) The rotor and the stator core have an infinite permeability.
- ii) The eddy currents flow only in the direction of the z-axis of the cylindrical coordinate system.
- iii) The compensation field generated by eddy current is neglected.

A consequence of a slotted stator and the fact that the windings are discretely distributed around the circumference of the stator is the introduction of higher harmonic components into the armature air-gap magnetic flux density [2]. To calculate the eddy-current contribution first the discrete motor winding is replaced by a current sheet on the very top of lamination teeth (at  $r = R_s$ ) as in [3]. The current sheet equation is also transformed into the rotor coordinate system, which is relevant for eddy current loss calculation in permanent magnets.

$$\begin{aligned} J_s(\varphi, t) &= \\ &= \sum_{k=1,2,\dots} J_{3k-1} \cos((3k-1)p_s \varphi - ((3k-1)p_s + p_r)\omega t) - \\ &- \sum_{k=1,2,\dots} J_{3k+1} \cos((3k+1)p_s \varphi + ((3k+1)p_s - p_r)\omega t) \end{aligned} \quad (2)$$

In (2)  $J_n$  ( $n = 3k-1$  or  $3k+1$ ) are the current distribution coefficients which can be calculated via (3) from the geometric parameters [4].

$$J_n = \frac{2N_s I_0}{\pi R_s} K_{wn} \quad (3)$$

where  $I_0$  is the main current harmonic component,  $K_{wn}$  is the winding factor which reflects the shape of the current sheet [4] and depends on the specific winding and slot distribution; in our case:

$$K_{wn} = \frac{2R_s}{npb_0} \sin\left(\frac{npd_s}{2R_s}\right) \sin\left(\frac{n\pi}{2}\right) \quad (4)$$

If the magnetic flux density produced by induced eddy-current is neglected, the magnetic vector potential can then be calculated with the use of Laplace equation and boundary conditions, following from the current sheet definition on the edge of the stator and the infinite permeability of the rotor core.

$$H_\Theta(r=R_s) = J_s(\varphi, t), \dots B_\Theta(r=R_r) = 0 \quad (5)$$

where  $R_s$  and  $R_r$  are the outer stator core and inner rotor core radius respectively,  $H_\Theta$  is the tangential component of the magnetic field strength and  $B_\Theta$  is the tangential component of the magnetic flux density. We can directly calculate the eddy-current distribution from the magnetic vector potential  $A_z(r, \varphi, t)$ :

$$J_e(r, \varphi, t) = -\gamma \frac{\partial A_z(r, \varphi, t)}{\partial t} + C(t) \quad (6)$$

where  $J_e$  is the eddy current density and  $\gamma$  is the conductivity of the permanent magnet material. The term  $C(t)$  in the expression (6) is the integration constant which is used to ensure the magnets are insulated from each other. The eddy current density in equation (6) thus satisfies the following equation for the area of the magnet  $S$ :

$$\int_S J_e(r, \varphi, t) r \, dr \, d\varphi = 0 \quad (7)$$

that is equivalent to the statement, that no current flows between the magnets.

### 3. Finite element analysis

The two dimensional FEM analysis [5] was used to obtain accurate results for eddy-current density distribution and the losses in permanent magnets. Finite element calculations offer an satisfactory alternative for estimation of the effect of design parameters on the losses in permanent magnets. On the other hand, setting up a measurement of eddy currents and eddy-current losses is very difficult, and calculating results indirectly from heat generation is only as accurate as the assumptions of the stator and winding losses and the conductivity of the heat paths.

The mesh lines of the lengths ranging from 0.3 mm up to 2 mm were defined for different regions and a mesh with 14300 nodes and 7000 surface elements was created. The quality of the mesh elements was verified by the program's internal mesh-quality test. Only one magnetic pole pair was modelled using symmetrical periodical conditions (Fig. 2).

A non-linear  $B(H)$  characteristic of M270-35A electrical steel was implemented to model the rotor and stator core and each of the magnet volumes was defined as a solid conductor.

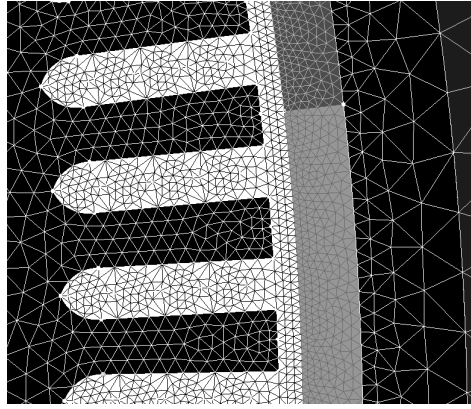


Figure 2. Example of the finite element mesh

The remanent flux density of the magnets was set to zero in order to calculate just the contribution of the stator current to the losses. The magnetic-flux density in the stator teeth was below saturation level, i.e. below 1.6 Tesla. If the stator teeth were saturated, we would expect a large deviation from the analytical results, which assume infinite permeability of the stator core.

#### 4. Results

The results of the finite element analysis were compared to the analytical equations describing eddy-current losses from the literature [3] in order to check the area of validity of analytical formulation and to draw conclusions about design guidelines for reduction of permanent magnet heating. The focus was on variation of four important design parameters:

- Air-gap length ( $a_g$ )
- Number of magnetic pole-pairs ( $p_r$ )
- Stator slot width ( $d_s$ )
- Magnet thickness ( $s_m$ )

These parameters are the most influential on the harmonic content of the air-gap magnetic field. The air-gap length and the pole number, have a similar effect, because the harmonic content of the air-gap magnetic field depends heavily on the ratio between the air-gap length and the geometrical modulation wavelength, which is tightly connected to the pole pair number. The slot width was chosen because it is responsible for modulation of both the stator magnetic field density and the permanent magnetic field density. The last parameter that was varied is the permanent magnet thickness, which modifies the MMF of the magnet as well as the effective air gap between rotor and stator (if the air gap is kept constant).

The original motor model (Table 1) was set up in such a way that the geometry was parameterized so the parameters could easily be investigated. They were then varied between the boundaries found in Table 2.

Table 2. Boundary conditions for parameter variation

Parameter	>	<
$p_r = p_s$	10	30
$a_g$	0.3 mm	1.9 mm
$d_s$	1.40 mm	3.95 mm
$d_m$	1.5 mm	4.5 mm

The operating point of the machine was taken to be at the maximum capability. The coils then carry a total current with an amplitude of 565A (each turn carries 100 ARMS). Even in these extreme conditions the eddy-current losses in the original machine are negligible in comparison to losses from other sources.

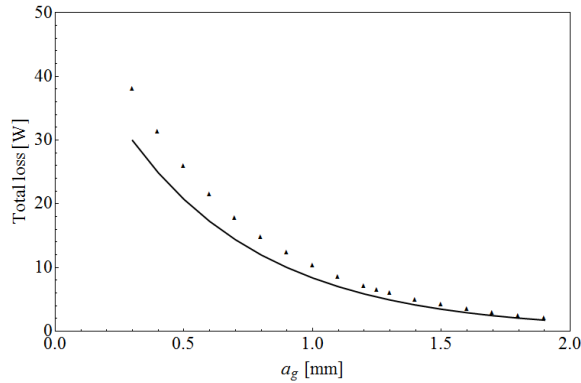


Figure 2: Dependence of total eddy current losses in all permanent magnets of the machine on the air-gap length for a sinusoidal distribution of current in the stator winding

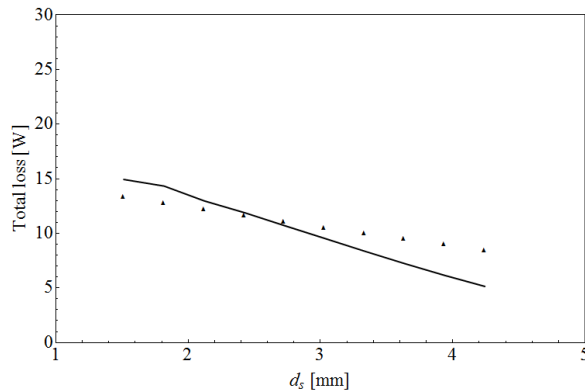


Figure 3: Dependence of total eddy current losses in all permanent magnets of the machine on the slot width for a sinusoidal distribution of current in the stator winding

The total loss exhibited by all magnets is 10 W, which is 0.2 W per magnet. The losses are also quite insensitive to parameter variation including the pole-pair number

variation. When reducing the pole pair number and the air-gap length the total losses in all magnets approach 40 W, and are relatively small compared to other sources of losses.

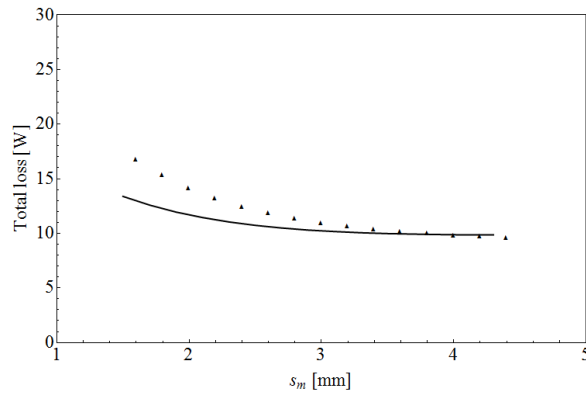


Figure 4: Dependence of total eddy current losses in all permanent magnets of the machine on the magnet thickness for a sinusoidal distribution of current in the stator winding

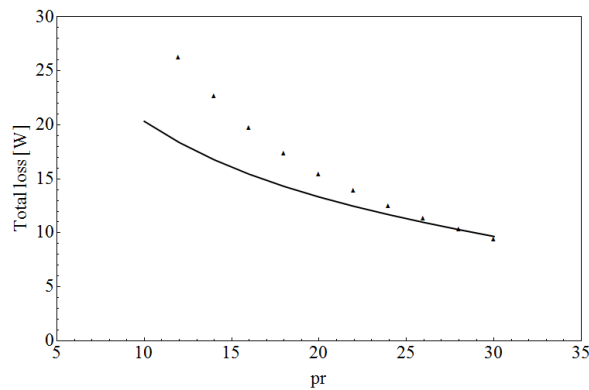


Figure 5: Dependence of total eddy current losses in all permanent magnets of the machine on the pole pair number for a sinusoidal distribution of current in the stator winding

The analytical method of calculation has showed its usefulness in the investigated parameter range, especially for the cases where the effective air gap is large (large  $a_g$  or  $s_m$ ) or there are less higher harmonics in the air-gap magnetic flux (small  $d_s$ ). Since any two-dimensional calculation of eddy currents is an approximation in itself, the analytical calculations can be taken as a fast way to obtain an estimate of losses caused by the stator current. If the losses exceed a certain level, a more accurate 3D model should be used in order to have accurate input for cooling ribs dimensioning.



## 5. Conclusion

FEM analysis of losses in permanent magnets of a direct drive multi-pole machine loaded with sinusoidal current showed that care should be taken when designing such a machine to keep the losses in permanent magnets as low as possible. Besides the losses caused by the sinusoidal current, also the losses caused by the current ripple and the permeance variation of the air gap contribute to total losses in the permanent magnets of a permanent magnet synchronous motor and add up so they can cause problems with overheating and demagnetization. The dependence of losses on design parameters can therefore crucially influence the choice of motor parameters in the design stage. Figures 2-5 reveal that the analytical method used in this paper can be used to predict eddy-current losses to a low level of accuracy, but in many cases it is a quick test of the parameter combination.

From the design parameter point of view increasing the pole number is very effective, whereas increasing both the magnet thickness as well as the air-gap length will reduce the eddy-current losses, but not as effectively. An alternative option is segmenting of magnets, or using buried magnet design.

The final action that can be taken is increasing the cooling capability of the rotor, which can be done using ribs, air-gap liquid cooling or simply air direction, depending on the volume of losses.

## Acknowledgements

Operation partially financed by the European Union, European Social Fund.

## References

- [1] Gotovac G., Lampic G. and Miljavec D.: *Analytical model of permeance variation losses in permanent magnets of the multi-pole synchronous machine*, Submitted to IEEE Trans. Magn., (2012).
- [2] Wang, J., Atallah, K., Chin, R., Arshad, W. M., Lendenmann, H.: *Rotor eddy-current loss in permanent-magnet brushless AC machines*, IEEE Trans. Magn., Vol. 46., No.7., (2010), pp. 2701–2707.
- [3] Huang Y. et al: *Eddy-current loss prediction in the rotor magnets of a permanent magnet synchronous generator with modular winding feeding a rectifier load*, IEEE Trans. Magn., Vol. 47., No. 10., (2011), pp. 4203-4206.
- [4] Zhu, Z. Q., Howe, D.: *Instantaneous magnetic field distribution in brushless permanent magnet dc motors. ii. Armature-reaction field*, IEEE Trans. Magn., Vol. 29., No. 1, (1993), pp. 136–136.
- [5] Cedrat Flux 2D 10.4, Software for electromagnetic design, (2011).